COLLECTIVITY IN LIGHT NEUTRON-RICH NUCLEI NEAR N=20: INTERMEDIATE-ENERGY COULOMB EXCITATION OF ^{32,34}Mg, ^{35,36}Al AND ^{37}Si

By

Jennifer Anne Church

A DISSERTATION

Submitted to
Michigan State University
in partial fulfillment of the requirements
for the degree of

DOCTOR OF PHILOSOPHY

Department of Physics and Astronomy

2003

ABSTRACT

COLLECTIVITY IN LIGHT NEUTRON-RICH NUCLEI NEAR N=20:
INTERMEDIATE-ENERGY COULOMB EXCITATION
OF ^{32,34}Mg, ^{35,36}Al AND ^{37}Si
By

Jennifer Anne Church

Collectivity in the neutron-rich nuclei ^{32,34}Mg, ^{35,36}Al and ^{37}Si has been studied via intermediate-energy Coulomb excitation in an early experiment at the National Superconducting Cyclotron Laboratory's Coupled Cyclotron Facility. Reduced transition probabilities and quadrupole deformation parameters were extracted from the measurements.

^{32,34}Mg are members of a group of nuclei near $N = 20$ which exhibit collective characteristics unexpected for nuclei at or near a shell closure. The observations are successfully reproduced by shell model calculations that allow a $2\hbar\omega$ intruder configuration as the ground state, in which 2 neutrons are promoted from the $\nu 1d_{3/2}$ level to the $\nu 1f_{7/2}$ level. Models based on valence spaces limited to the $0\hbar\omega$ configuration which describe the stable nuclei well are unsuccessful in calculating observables for these nuclei. Because of this inversion of the $0\hbar\omega$ and $2\hbar\omega$ configurations in energy, the group has been named the "Island of Inversion," and is predicted by the $2\hbar\omega$ shell model to extend to $10 \leq Z \leq 12$ and $20 \leq N \leq 22$. The possibility for static shape deformation has also been considered, and models utilizing a deformed potential are successful in calculating excited state energies and reduced quadrupole transition probabilities for this group. Recently, the neutron boundary has been predicted to extend to $N = 24$ by the $sd - pf$ Monte Carlo Shell Model, and several mean-field calculations predict shape coexistence for ^{32}Mg.

The energy of the first 2^+ state in ^{32}Mg was measured to be 885(18) keV, and

found to be in agreement with the adopted value of 885.5(7) keV. A second gamma-ray at 1436 keV was also observed with low statistics. The reduced electric quadrupole transition probability, $B(E2; 0^+_{g.s.} \rightarrow 2^+_1)$, of 447(57) e^2fm^4 and a $|\beta_2|$ value of 0.51(3) were extracted from the measurements without consideration of feeding from the 2321 keV state. A $B(E2; 0^+_{g.s.} \rightarrow 2^+_1)$ value of 328(48) e^2fm^4 and a resulting quadrupole deformation parameter $|\beta_2| = 0.42(3)$ were obtained after consideration of a minimum correction for feeding of the 885 keV state by the 2321 keV state via the 1436 keV gamma-ray. Both values are in agreement with the adopted value, and in contrast with the measurement by Chisté *et al.* which yielded 622(90) e^2fm^4 for the excitation strength. Our measurement agrees with the calculations of the $2\hbar\omega$ shell model.

A first excited-state energy of 659(14) keV for ^{34}Mg was also measured via Coulomb excitation. The value extracted for the reduced quadrupole transition probability of 541(102) e^2fm^4 with a corresponding $|\beta_2|$ value of 0.54(5) indicates that ^{34}Mg is more collective than ^{32}Mg as expected for a nucleus away from the closed shell. However, the value is also considerably higher than that calculated by the $0\hbar\omega$ shell model. One other observed value for the $B(E2; 0^+_{g.s.} \rightarrow 2^+_1)$ has been reported by Iwasaki *et al.* of 631(126) e^2fm^4. Our measurement is slightly lower than this. Both are in agreement with the $2\hbar\omega$ shell model calculations.

The remainder of the constituents of the ^{34}Mg cocktail beam were also observed. Gamma-rays were observed at 985(21) keV for ^{35}Al, 1437(30) keV for ^{37}Si, and 647(14) keV and 967(20) keV for ^{36}Al. Because there are no adopted values for the spin and parity of the odd-nucleon nuclei ^{35,36}Al and ^{37}Si, J^π values were calculated by the OXBASH shell model. Maximum values were then obtained for E1, M1, and E2 reduced transition probabilities and compared to listed recommended upper limits. The $B(\pi\lambda)$ values for ^{36}Al were previously unmeasured. E1, M1 and E2 cannot be excluded as possibilities for the transitions in all three nuclei from our analysis.

for my mom and dad, and my brother dan

ACKNOWLEDGMENTS

I acknowledge the work of the Gamma group. It was the idea of Thomas Glasmacher and Boris Pritychenko to investigate the Island of Inversion in depth. The graduate students in no particular order helped perform and set up the experiment: Ben Perry, Chris Campbell, Dan-Cristian Dinca, Katie Yurkewicz (Miller), Heather Olliver, and Alexandre Obertelli. Katie Miller wrote the Physica portion of the calibration routines, and Heather Olliver and I compared adaptations of Boris Prytychenko and Heiko Scheit's angular distribution codes as a double check. Heather also gave me the m-state plots shown in the figure. Ben Perry dis- and reassembled the APEX NaI(Tl) array and took the great majority of the calibration data during the final pre-experiment calibration (there were 4 months or so of pre-experiment calibrations). (I wish the graduate students the best of luck. You will need it). The post doctoral researchers Zhiqiang Hu, Wilhelm Mueller and Joachim Enders worked on the electronics. Zhiqiang Hu wrote the SpecTcl code which was later adjusted. Alexandra Gade made comments pertaining to the thesis itself.

Robert Janssens (Argonne Nat. Lab) had the idea for the bismuth target. Dave Sanderson and Andy Thulin worked with me setting up the vacuum system.

This was one of the first experiments to utilize the Coupled Cyclotron Facility and would not have been possible without it. It took a lot of hard work by too many people to list to complete the upgrade. Their work is duly acknowledged.

Alex Brown, Gregers Hansen, Bernard Pope, Wayne Repko, and Horace Smith participated as members of my thesis committee.

Now I move on to people I would like to personally thank.

Thanks to four all around nice guys: Len Morris for working with me on the detector support design, Dale Smith for all the help with the phone dialer, Jim Wagner for fixing the hydraulics and investigating the ticking in the ceiling, and Jon Bonofiglio for the Malt-O-Meal and the carbon stripper mechanism. A special thank you to the

computer group at the NSCL: Ron, Jay, Barb, Milt and the helproom staff. Thanks Milt for being strangely normal. Thanks Katie Miller for organizing a great get-together and the help with the thesis template, and Pat Lofy and Michelle Ouellette for all the rides to the airport.

Thank you Professor Pollack, Professor Kovacs and Debbie Simmons for all of your understanding and support starting with the divorce, and continuing until even now.

Thank you to my friends. Thanks Waz, Karen, Jen, and Cherami for calming me down and helping me through the hard parts, and Chris, AJ, and Jon for being there after my divorce. To Chung's Taekwondo, thanks for letting me take my frustrations out on you all. (I hope you find out someday exactly how Grandmother Chung got to be so fast.)

When a person grows up in Westwood, California, (population 2000, elevation 5000 ft.), the entire faculty and staff of the schools she attends become her extended family (some of whom actually are her parents). So I thank my old teachers for their enduring support, Mr. Church, Señora Iglesia, Mr. Kindig, Mrs. Brydon, Mr. Bryant, Mr. Hasselwander, Mr. Clark and Mr. Growden. Thank you to some family friends, Arvid and Lynne. Thanks Frank and Bill (I think).

Most of all I thank my family. My Mom and Dad, Patricia and Randall Church, my brother Daniel Church, my nephews Tyler and Nicolas, and my niece Alissa are irreplaceable. In this world of broken homes, and unsolid ground, my family has been my foundation, the solid ground under all of the mountains I climb. They remind me that sometimes my mountain is really just a rocky knoll somewhere out in the middle of Nevada, complete with dragonflies and aliens and stuff. Thanks Mom for always encouraging me to keep on, for being positive at all the right moments, you are the one who keeps me on track. Thanks Dad, for all the late night talks, for the philosophy and the perspective, you are the one who opens my eyes. Thanks Dan for being my biggest fan, you are the one who reminds me it is worth it. Thanks Tanya

for trying to get me to be peppy (haha). Thanks Tara for always being supportive, no matter what. Thanks Ty and Nic and Ali for all the singing and laughing and goofing around (with Aunt Lucky). Thanks also to all the Uncles and Aunts and cousins (there are many) for just being there.

Lastly, I give thanks to God (!) for getting me through this, and of course for all the nuclei–exotic, stable, and the rest.

Contents

List of Figures

IMAGES IN THIS DISSERTATION ARE PRESENTED IN COLOR.

List of Tables

Chapter 1

Motivation

1.1 The Atomic Nucleus

The field of nuclear physics has grown rapidly since the discovery of the atomic nucleus in the early 1900s [1–5]. As shown in Figure 1.1, a simplified chart of the nuclides, we now know of thousands of nuclei, only 270 of which are stable to decay [6]. Each nucleus is comprised of a number of protons (Z) and neutrons (N). These nucleons are quantum-mechanical particles and thus the nucleus itself is a quantum-mechanical many-body system.

A current goal of nuclear physics is the unified microscopic description of all nuclei, stable and unstable [8]. This is approached by comparing experimental observations to predictions made by theoretical models of the nucleus. Because the nuclear Hamiltonian is not known exactly, there are many nuclear models with many forms for the nuclear Hamiltonian. The comparison of the nuclear models to experimental observables is key to obtaining a realistic description of the nucleus.

Most nuclear models accurately predict the quantum-mechanical observables for stable nuclei. However, with the production of rare-isotope beams, discrepancies between what is expected from observed trends in the stable nuclei and the measured properties of neutron-rich nuclei have become obvious. For example, mass measure-

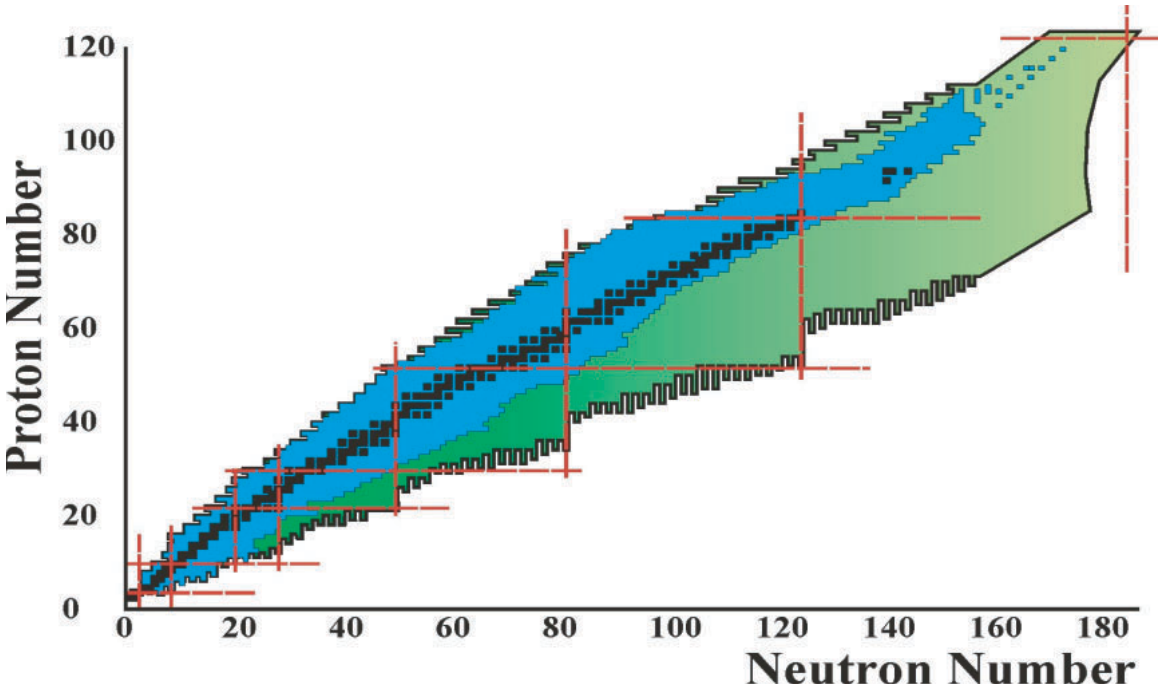

Figure 1.1: A simplified chart of the nuclides. Proton number vs. neutron number are plotted. Nuclei in black are stable. The dashed lines indicate the magic numbers as predicted by the standard shell model of Mayer and Jensen [7]. Although they extend beyond stability in the figure, recent experimental and theoretical developments indicate that these numbers of neutrons and protons may not indicate a closed shell for nuclei away from stability.

ments of ^{31,32}Na in 1975 by Thibault *et al.* revealed larger two-neutron binding energies than seen in trends for all of the other nuclei at the time [9]. The strong E1 transition in ^{11}Be measured by Millener *et al.* in 1983 is only reproduced by integrating out to an unprecedented nuclear radius of 35 fm [10]. Measurements by Tanihata *et al.* in 1985 showed ^{11}Li to have a much larger interaction radius than expected from the comparison to other light nuclei [11]. In the context of the present work, the collectivity in ^{32}Mg, as evident in the large $B(E2)$ value measured by Motobayashi *et al.* in 1995, was not expected for a nucleus with a magic number of neutrons neither from the shell model nor the trends in the stable nuclei [12].

Although much work has already been done, data are still needed for nuclei that are closer to the proton- and neutron-drip lines in order to fully develop the framework for these rare isotopes. The problem is being attacked by making nuclei far from

stability accessible through upgrades to existing accelerators such as the Coupled Cyclotron Facility (CCF) at the National Superconducting Cyclotron Laboratory (NSCL) [13], and by the proposed construction of new facilities such as the Rare Isotope Accelerator (RIA).

1.2 Electromagnetic Transitions and Collectivity

In order to reconcile theory and experiment for a complete description of the atomic nucleus, it is ideal to compare nuclear structure properties that can be measured in an essentially model-independent way, and at the same time, be robustly predicted by theory. Electromagnetic transitions between nuclear states are particularly well-suited for this. Reduced electromagnetic transition probabilities are readily calculated by most models and can be measured via intermediate-energy Coulomb excitation [14].

1.2.1 Transition Strengths

For an electromagnetic transition, the multipolarity λ of the operator O_λ connecting the nuclear state $|i\rangle$ to the state $|f\rangle$ depends on the angular momentum J and parity π selection rules, where the subscript i indicates the initial state, and the subscript f indicates the final state, E indicates an electric transition and M indicates a magnetic transition [15]:

$$|J_i - J_f| \leq \lambda \leq J_i + J_f \tag{1.1}$$

and

$$\pi_f \pi_i = \begin{cases} (-1)^\lambda, & \mathrm{E}\lambda \\ (-1)^{\lambda+1}, & \mathrm{M}\lambda. \end{cases} \tag{1.2}$$

The transition rate $\mathcal{W}$ for the selected multipole is approximated as

$$\mathcal{W}(\pi\lambda; J_i \rightarrow J_f) = \frac{8\pi\,(\lambda+1)}{\hbar\lambda\left[(2\lambda+1)!!\right]^2}\left(\frac{E_\gamma}{\hbar c}\right)^{(2\lambda+1)} B(\pi\lambda; J_i \rightarrow J_f) \tag{1.3}$$

where E_γ is the energy of the gamma ray emitted in the decay, and $\hbar c$ is 197.329 MeV/fm, with the reduced transition probability

$$B(\pi\lambda; J_i \to J_f) = \frac{1}{2J_i + 1} \left|\langle J_f \| O_\lambda \| J_i \rangle\right|^2 . \tag{1.4}$$

For the transition $|f\rangle \to |i\rangle$ the reduced transition probability is denoted $B(\pi\lambda \downarrow)$ and for the transition $|i\rangle \to |f\rangle$ the reduced transition probability is denoted $B(\pi\lambda \uparrow)$, and

$$B(\pi\lambda \uparrow) = \frac{2J_f + 1}{2J_i + 1} B(\pi\lambda \downarrow). \tag{1.5}$$

For a nucleus with even numbers of protons and neutrons, the ground state generally has spin and parity 0^+ because all of the nucleons are paired. The spin and parity of the first excited state are usually 2^+ for these even-even nuclei, although there are some exceptions. From the selection rules, the transition between these states is an electric quadrupole ($E2$) transition.

1.2.2 Collectivity

A nuclear transition from an initial state to a final state may involve one nucleon, or it may involve the coherent motion of many of the nucleons in the nucleus. When the transition includes motion of many of the nucleons, the states are called collective states, and the transition is called a collective transition. The transition probability for a collective electromagnetic transition is generally larger than that for an electromagnetic transition in which only one particle changes its state. [16]. Thus the comparison of the measured reduced transition probability to an estimate for the single-particle reduced transition probability gives an indication of the "collectivity" of the nucleus. The estimates for single-particle transition rates are outlined in Appendix A. Generally, at shell closures, nuclei are less collective than at mid-shell because the nucleons have to overcome a large energy gap to form an excited state. Even-even closed-shell nuclei tend to exhibit high 2_1^+ excitation energies and low reduced electric quadrupole

transition probabilities to their first 2^+ state as compared to those at mid-shell [17].

1.3 Nuclear Models

Nuclear structure properties such as the reduced transition probability $B(\pi\lambda)$ can be calculated by two general types of models. In collective models such as the rotational model, the Hamiltonian describing the nucleus is written in terms of the coordinates of the nucleus as a whole. In single-particle models such as the nuclear shell model, the nuclear Hamiltonian is written in terms of the coordinates of the individual nucleons.

1.3.1 Collective Models and Quadrupole Deformation

The collective models describe collective excitations as the deformation or a vibration of the nucleus as a whole. Models that describe the statically deformed nuclei are called rotational models while vibrations are described by vibrational models.

Within the framework of the rotational model for a ground state band and an axially symmetric deformation, the reduced electric quadrupole transition probability is related to the intrinsic quadrupole moment Q_0 of the nucleus through [18]

$$B(E2; 0^+_{g.s.} \rightarrow 2^+_1) = \frac{5}{16\pi} e^2 Q_0^2. \tag{1.6}$$

The quadrupole deformation parameter β_2 is defined to be related directly to the intrinsic quadrupole moment Q_0 of the nucleus. The relationship is written to first order in β_2 [18]:

$$Q_0 = \frac{3}{\sqrt{5\pi}} Z R_0^2 \beta_2. \tag{1.7}$$

Combining 1.6 and 1.7, the quadrupole deformation parameter is related to the $B(E2)$ value by

$$|\beta_2| = \frac{4\pi}{3} \sqrt{B(E2)} \frac{1}{ZeR_0^2}, \tag{1.8}$$

where $R_0 = 1.2A^{1/3}$ fm and $e^2 = 1.44$ MeV/fm [18]. The distortion parameter δ is also used to describe deformation and is related to β_2 through

$$\delta = 0.945\beta_2. \tag{1.9}$$

It can also be shown that the same relationship between the quadrupole deformation parameter and the $B(E2)$ value is obtained through the vibrational model of the nucleus [18]. Therefore, the reduced transition probability alone does not indicate whether or not the nucleus is deformed, but rather gives the strength of the collective excitation.

A distinction can be made between rotational and vibrational collectivity by measuring the intrinsic quadrupole moment of the ground state of the nucleus directly. The ratio of the energy of the first 4^+ state to the energy of the first 2^+ state in the nucleus, $E(4_1^+)/E(2_1^+)$ also gives an indication of the source of the collectivity [19]. From a model assumption of a rigid rotor, the $E(4_1^+)/E(2_1^+)$ ratio is 3.3, while from the assumption of a harmonic vibration the ratio is 2. By convention negative β_2 values indicate nuclei that are flattened oblately, and positive values of β_2 are nuclei that are elongated in a prolate shape. The shapes are depicted in Figure 1.4, where the energy levels are plotted as a function of the distortion parameter δ in the Nilsson model which will be discussed in Section 1.3.2.

The second type of nuclear model is the single-particle model. This type of nuclear model includes the degrees of freedom of the nucleons individually. Since the $B(\pi\lambda)$ value can be calculated from these models, the calculated degree of collectivity can be compared to experimental values. Subsequent conclusions drawn from the comparison oftentimes elucidate the single-particle structure of the nucleus.

1.3.2 Single-Particle Models

Single-particle models attempt to describe the nucleus in terms of the individual nucleons. The Hamiltonian arises from the interaction of one nucleon with an average field generated by the remainder of the nucleons in the nucleus. The nuclear wavefunctions Φ_k are expressed in terms of the individual nucleons, and combinations of these functions form the antisymmetrized many-body basis states which are written as a Slater determinant [15],

$$\Phi_k(\mathbf{r}_1, \mathbf{r}_2, \mathbf{r}_3, \cdots, \mathbf{r}_A) = \frac{1}{\sqrt{A!}} \begin{vmatrix} \phi_1(\mathbf{r}_1) & \phi_1(\mathbf{r}_2) & \cdots & \phi_1(\mathbf{r}_3) \\ \phi_2(\mathbf{r}_1) & \phi_2(\mathbf{r}_2) & \cdots & \phi_2(\mathbf{r}_3) \\ \vdots & \vdots & \ddots & \vdots \\ \phi_A(\mathbf{r}_1) & \phi_A(\mathbf{r}_2) & \cdots & \phi_A(\mathbf{r}_A) \end{vmatrix} \tag{1.10}$$

where the $\phi_i(\mathbf{r}_j)$ are the single-particle wave functions for A nucleons and $\mathbf{r}_j$ are the positions of the individual nucleons. The single-particle Schrödinger equation is

$$h(\mathbf{r}_i)\phi_k(\mathbf{r}_i) = \epsilon_k \phi_k(\mathbf{r}_i), \tag{1.11}$$

where $h(\mathbf{r}_i)$ is the single-particle Hamiltonian and ϵ_k are the single-particle energy eigenvalues. The many-body Hamiltonian can then be written

$$H = \sum_{i=1}^{A} h(\mathbf{r}_i) + \sum_{i \neq j=1}^{A} \widetilde{V}(\mathbf{r}_i, \mathbf{r}_j) \tag{1.12}$$

where $\widetilde{V}(\mathbf{r}_i, \mathbf{r}_j)$ is the residual 2-body interaction.

The variety of single-particle models in existence today are based on the early Shell Model of Mayer and Jensen [20, 21]. This model is often referred to as the Standard Shell Model [6]. In 1948, Mayer noticed from the experimental evidence of the time that nuclei with proton or neutron numbers 20, 50, 82 and 126 are particularly stable [7]. The following year, Mayer [20] and Jensen [21] added the spin-orbit term

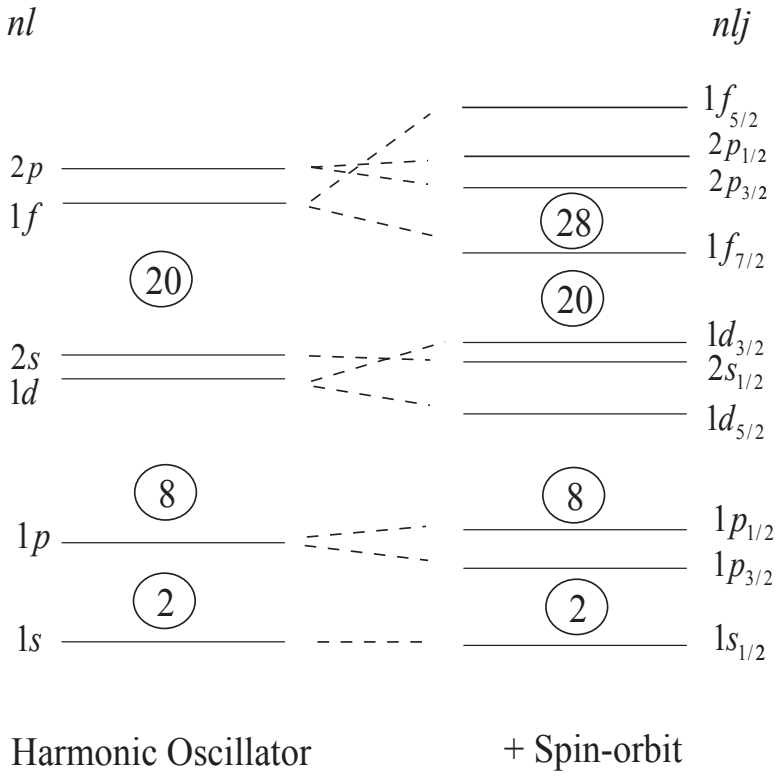

Figure 1.2: Energy level schemes for the harmonic oscillator including an l^2 term (left) and including the spin-orbit splitting (right). Major shell gaps up to $N = 28$ are displayed.

to the harmonic oscillator Hamiltonian. The addition of the spin-orbit term to the harmonic oscillator results in the splitting of the harmonic oscillator levels as is depicted in Figure 1.2. Adding the spin-orbit term results in major gaps in energy for the proton and neutron numbers 2, 8, 20, 28, 50, 82, and 126. These numbers of nucleons are called the "magic" numbers. Although the simple shell model fits the overall observed trends in stable nuclei for measurements such as the first excited-state energy accurately, it has been found to diverge from the results of measurements on neutron-rich and neutron-deficient nuclei, see for example, Reference [9].

The single-particle energy levels are filled according to the Pauli exclusion principle, and the neutrons (ν) and protons (π) fill separate sets of levels. Here the levels are labelled by n, l and j, where n is the major harmonic oscillator quantum number, l is the angular momentum quantum number and $j = l + s$ is the total angular mo-

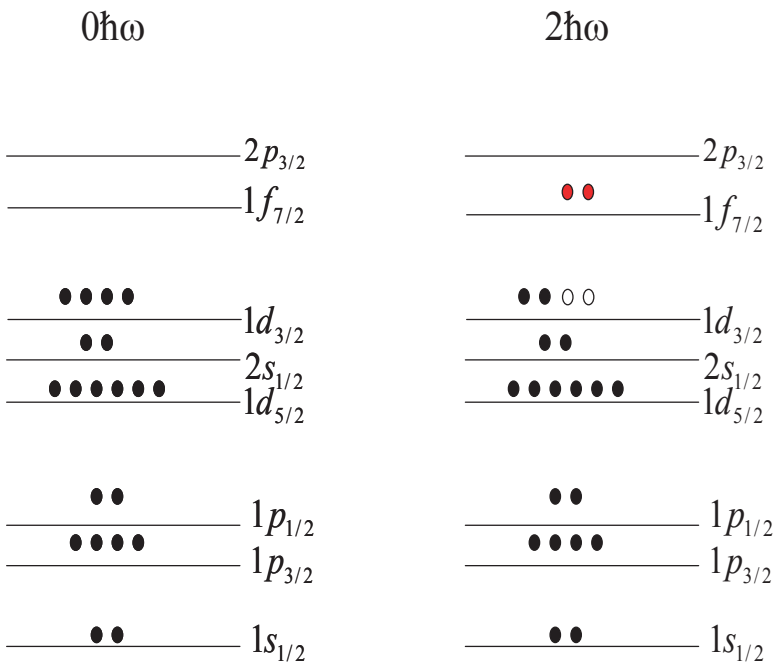

Figure 1.3: $0\hbar\omega$ and $2\hbar\omega$ configurations for 20 neutrons. The $2\hbar\omega$ configuration includes the promotion of two nucleons over the major energy gap in the standard shell model ordering. In this example, two neutrons are promoted over the $N = 20$ gap to the pf shell and two holes (open circles) are left in the $1d_{3/2}$ level.

mentum, where s is the spin of the nucleon. A level is full when it has $2j+1$ protons or neutrons since j has $2j + 1$ m-substates (projection of the angular momentum along z), and the nucleon in each m state can be $s = 1/2$ or $s = -1/2$ (spin up or spin down) [15].

Configurations of nucleons with respect to this standard shell model energy level ordering are referred to as n$\hbar\omega$ configurations. The n refers to the number of neutrons or protons that have been promoted from the sd shell to the pf shell, leaving n holes in the original level. For example, a $2\hbar\omega$ configuration promotes 2 neutrons or protons and leaves 2 holes in the original level. These are also referred to as n-particle n-hole (npnh) configurations. In stable nuclei the $0\hbar\omega$ configuration generally describes the ground state well. However, for nuclei away from stability, this is not always the case. The idea of the $2\hbar\omega$ configuration as the ground state is known as an intruder configuration and is depicted in Figure 1.3 [6].

A variety of single-particle models have been developed. The majority of them are

shell model or mean-field approaches, although there are also attempts to go beyond the mean field. The models are currently written in a variety of forms with spherical or deformed potentials, pairing and correlation energies, and even incorporating relativistic formalism in which the nucleons interact via meson exchange.

For the shell models, the single-particle states are generated and grouped into core and valence parts. The nuclear wave functions are generated in the valence shell. For a state of total angular momentum J there are $2J + 1$ M-substates, and the number of determinants for a given value of M gives the shell model dimension. The dimensions get quite large, around 10 billion for an exotic nucleus near $N = 20$, and truncation or other methods such as the Monte Carlo treatment are necessary to reduce the space such that it can be managed by the current computing technology [6, 22]. The Hamiltonian is generally a combination of a spherical potential and an effective interaction that accounts for the interactions excluded by the truncation. Complete descriptions can be found in References [6, 22].

One common mechanism utilizing the mean field are Hartree-Fock (HF) calculations. HF is a calculus of variations approach involving self-consistent calculations of the eigenstates such that the majority of the interactions are contained in the single-particle Hamiltonian [15]. The goal is to make the residual Hamiltonian small. There are a variety of interactions that may be included in this treatment. Another mean-field approach is the relativistic mean field framework (RMF). In the RMF, the nucleons are treated as Dirac spinors and interact with each other via meson exchange [23].

It is possible to make calculations from a basis and potential defined for a statically deformed nucleus. The deformed shell model developed by Sven Nilsson [24] was the first to do this and is still used as a first approach to modelling a deformed nucleus [25]. The spin-orbit term is included in the deformed potential written here

for a quadrupole field:

$$h(\mathbf{r}) = h_{HO} - \frac{1}{3}\delta\mu\omega_0^2 r^2\sqrt{\frac{16\pi}{5}}Y_{20}(\theta,\phi) + a\,\mathbf{l}\cdot\mathbf{s} + b\mathbf{l}^2 \tag{1.13}$$

where h_{HO} is the harmonic oscillator potential (spherical), $a\,l\cdot s$ includes the spin-orbit splitting, $b\mathbf{l}^2$ gives proper ordering to the single-particle states, and δ is related to the quadrupole deformation parameter by $\delta \approx 0.95\beta$ to first order [18]. Due to the statically deformed shape of such a nucleus, the quantum numbers in this model differ from the spherical shell model. N is the major harmonic oscillator number, n_z the z component of that number, and K^π is the projection of the total angular momentum J onto the symmetry axis. The projections of j, l and s onto the symmetry axis are Ω, Λ and Σ respectively. $K = \Lambda \pm \Sigma$ and $\Sigma = 1/2$. The energy eigenvalues depend on the degree of axial deformation and are called Nilsson levels. They are labelled by $K^\pi[N\,n_z\,\Lambda]$ and are displayed in what is known as a Nilsson diagram as a function of the axial quadrupole deformation. An example of such a diagram for light nuclei taken from [25] is displayed in Figure 1.4. Toward the prolate and oblate limits, the energies of the spherical levels begin to change, and in some cases the level ordering is actually inverted.

When comparing the experimental data to the models, the starting point is generally the spherical potential, $0\hbar\omega$ ground-state, standard shell model standpoint. In such an extension of the trends for the stable nuclei, the nucleus is expected to be rather stable at and near a closed shell (a magic number of nucleons). Compared to a nucleus away from a closed shell, the first excited state energy should be higher and the probability for an electric quadrupole transition should be lower for the closed shell nucleus. Compared to the closed shell nucleus, two-neutron separation energies (S_{2n}) for a nucleus with one more than the magic number of nucleons should drop off sharply [6].

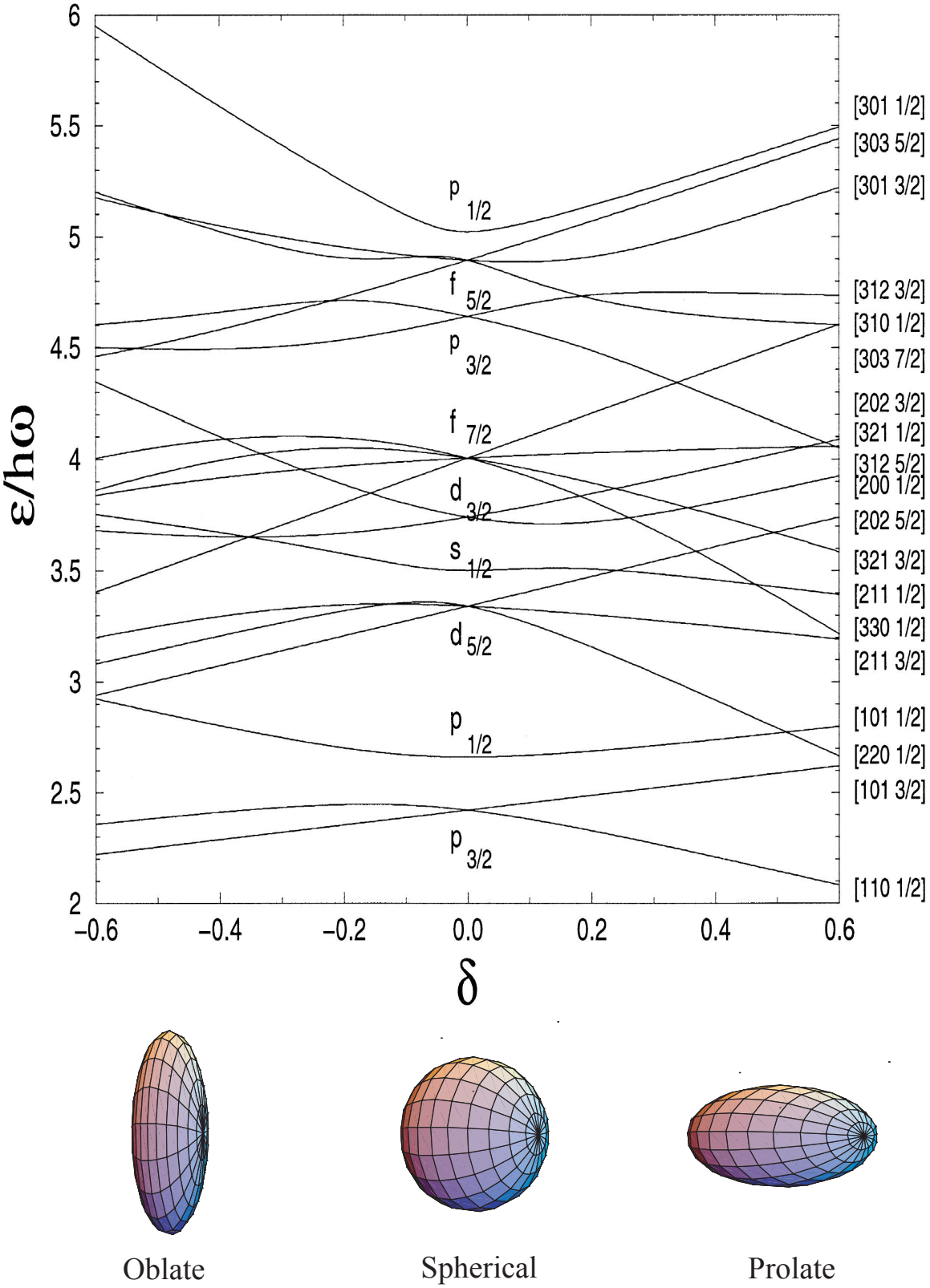

Figure 1.4: The Nilsson diagram pertinent to neutron levels for light nuclei near $N = 20$. Positive values of the distortion parameter $\delta \approx 0.945\beta_2$ to first order in the quadrupole deformation parameter β_2 indicate a prolate shape while negative indicate an oblate shape by convention. Representative shapes are depicted below the Nilsson diagram. The diagram is taken from [25].

1.4 The Island of Inversion

From the viewpoint of the standard single-particle shell model, nuclei at the magic number $N = 20$ should be spherical and are expected to exhibit non-collective or solely vibrational characteristics [6]. As a reference point, note that the doubly-magic nucleus ^{40}Ca has $E(2_1^+) = 3904.38(3)$ keV and $B(E2; 0_{g.s.}^+ \rightarrow 2_1^+) = 99(17)$ e^{2}fm^4 [17]. As the rare isotopes began to be experimentally explored, it was thought that the neutron-rich $N = 20$ isotones would also exhibit such characteristics. However, in 1975, experimental evidence to the contrary for a group of nuclei centered at $Z = 11$ and $N = 21$ began to appear [9].

1.4.1 Early Experiments

The first indication of an anomaly came with the results from Thibault's mass measurements showing the two-neutron separation energies S_{2n} of ^{31,32}Na to differ from those expected for a $0\hbar\omega$ ground state, with ^{32}Na having a larger value than ^{31}Na [9]. This discovery created a stir in the experimental and theory communities and much effort was subsequently put into the investigation of these nuclei. The $\beta^- n$ decay of ^{33}Na in 1984 [26] and Coulomb excitation in 1995 [12] showed an anomalously low first excited state energy for ^{32}Mg and it seemed as though this $N = 20$ closed shell nucleus was indeed collective. The suspicions were confirmed when a high reduced transition probability $B(E2; 0_{g.s.}^+ \rightarrow 2_1^+)$ was discovered for ^{32}Mg [12].

The extent of the region was investigated through several Coulomb excitation experiments at the NSCL. ^{31}Na was found to have a low-lying first excited state energy of 350 keV [27]. ^{28}Ne [25] and ^{34}Al [28] also showed evidence for low-lying states. Nuclei that did not demonstrate the apparent collective anomaly were the $N = 20$ nucleus ^{34}Si [29] with a first excited-state energy of 3305(55) MeV and a $B(E2\uparrow)$ value of 85(33) e^{2}fm^4.

1.4.2 Early Theory

The experimental discoveries in the region of the "Island of Inversion" [30] led to a substantial development in the theory community as well.

The general consensus among the early models is that the anomalous $B(E2)$ values and first excited state energies can be explained by a shape deformation caused by an intruder state with a $2\hbar\omega$ configuration in which one pair of $1d_{3/2}$ neutrons is promoted to the $1f_{7/2}$ level. This intruder configuration would be a highly excited state in nuclei near stability and yet is found to be lower in energy than the state with the standard $0\hbar\omega$ configuration for nuclei in the Island of Inversion. The expected configurations are in this way inverted.

In 1975, Campi first proposed that the high two-neutron separation energies S_{2n} in the sodium isotopes were due to nuclear deformation. He showed that spherical Hartree-Fock calculations cannot explain the discontinuity in the curve of two-neutron separation energies S_{2n} in the sodium isotopes while deformed Hartree-Fock theory was successful [31]. In 1981, Wildenthal and Chung showed that the standard shell model with neutron $d_{5/2} - s_{1/2} - d_{3/2}$ (sd) levels only as the valence space, could not accurately predict the ^{31}Na and ^{32}Mg mass measurements [32]. The same year, Watt added the $1f_{7/2}$ shell to the neutron *sd* valence space, restricted protons to $1d_{5/2}$ and by allowing $(0+2)\hbar\omega$ mixed configurations was able to reproduce the measured binding energies [33]. Poves and Retamosa added the $2p_{3/2}$ energy level to the neutron basis and also restricted protons to the $1d_{5/2}$ orbit. They were able to produce the experimental results for the excited-state energy, and claim that ^{30}Ne, ^{31}Na, ^{32}Mg are deformed due to the large correlation energy of these configurations [34].

The boundaries of this Island of Inversion were first predicted by Warburton, Becker and Brown in 1990 [30]. With a full *sd-fp* shell model space, and a weak coupling model, they diagonalized the n$\hbar\omega$ configurations separately and found that for the nuclei shown in Figure 1.5 , with $10 \leq Z \leq 12$ and $20 \leq N \leq 22$, the $2\hbar\omega$ configuration is lower in energy than the $0\hbar\omega$ configuration which does not allow

promotions over the neutron $1d_{3/2} - 1f_{7/2}$ gap. They described the mechanisms for this level inversion to be a small reduction in the single-particle energy gap, increased neutron-neutron pairing energy E_{nn}, and an increase in the proton-neutron interaction energy E_{pn} [30].

1.5 ^{32}Mg

Recent experiments confirm the early indications of the collectivity for the nuclei in the Island of Inversion. Support for the suspected static deformation in the region has been reported by Reference [35] in a comparison of the intrinsic quadrupole moments extracted from heavy ion scattering and an ECIS calculation with spectroscopic quadrupole moments measured through $\beta-$NMR by Reference [36] for the sodium isotopes. For the $N = 20$ nucleus, ^{31}Na, the intrinsic quadrupole moment deduced from the scattering of ^{28,30}Na differs from the spectroscopic quadrupole moment, indicating triaxiality as a possibility for the nucleus. In another recent development, the $E(2_1^+)$ value of ^{30}Ne has been measured at 791(26) keV [37]. This is lower than that for ^{32}Mg and indicates that the collectivity is enhanced with increasing neutron excess along $N = 20$ [37]. The first excited state energy and $B(E2; 0^+_{g.s.} \rightarrow 2^+_1)$ values for ^{34}Mg have also been recently measured at RIKEN [38, 39]. Of all of the recently researched nuclei in the Island of Inversion, ^{32}Mg has been the most extensively investigated nucleus both experimentally and through nuclear modelling. Because the focus of our work is the magnesium isotopes, ^{34}Mg and the well-studied ^{32}Mg, their experimental and theoretical background will be outlined in detail.

1.5.1 Experimental Background

Measurements of the lowest energy level in ^{32}Mg show it to be collective in nature. The first 2^+ level at 885 keV is well-known [12, 25, 38–41] and found to be unexpectedly low-lying for an $N = 20$ closed-shell nucleus. The corresponding $B(E2; 0^+_{g.s.} \rightarrow 2^+_1)$

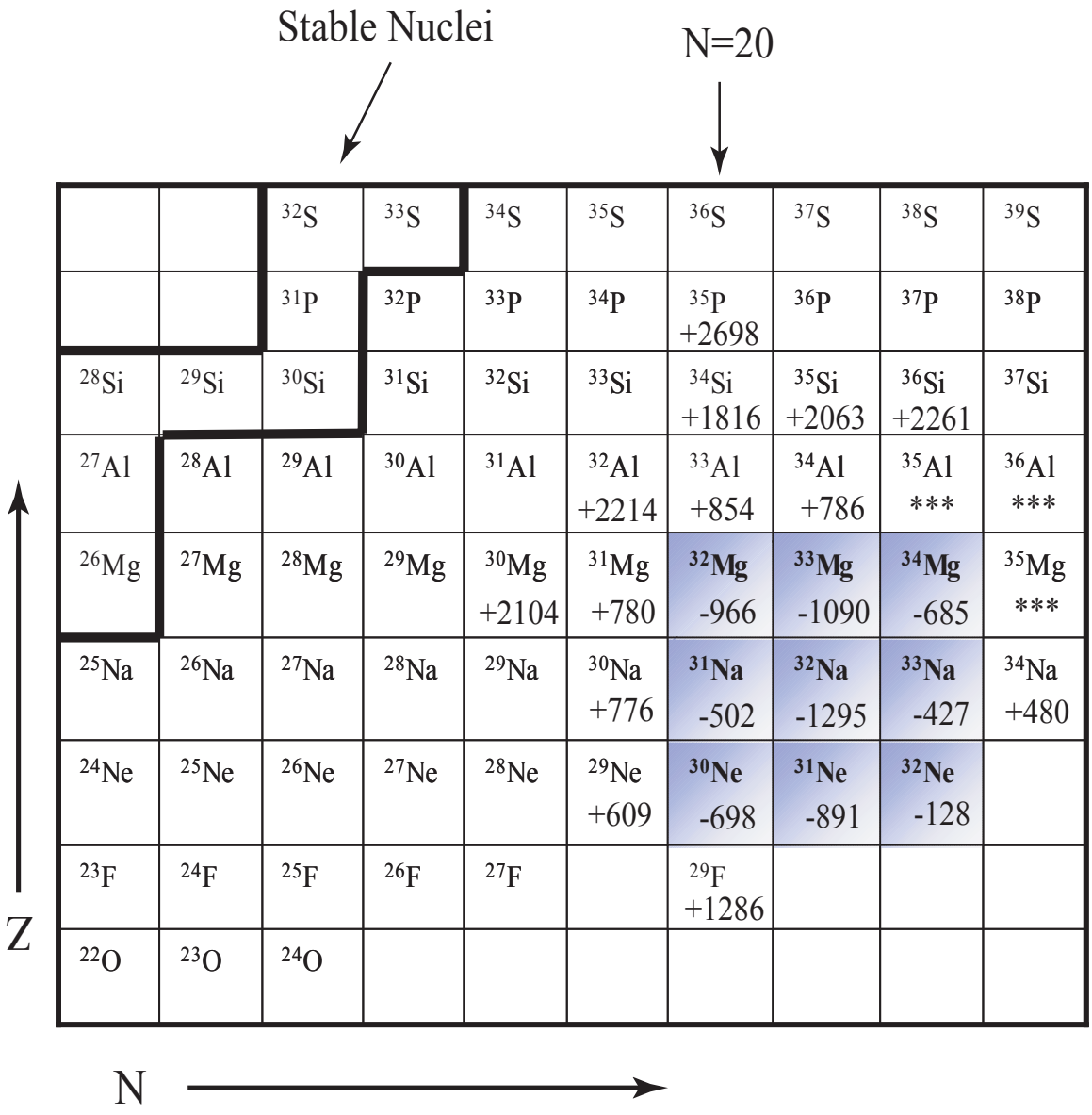

Figure 1.5: The Island of Inversion as predicted by Warburton, Becker and Brown [30]. The nuclei in the shaded boxes are predicted to exhibit a $2\hbar\omega$ ground state configuration. Excitation energies calculated from the weak-coupling model for the $2\hbar\omega$ ground state relative to the $0\hbar\omega$ state are indicated by the numbers in the boxes in keV. Nuclei with asterisks were beyond the calculation. Stable nuclei are outlined in bold.

value is also found to be uncharacteristically large [12, 25, 38, 39, 41]. A second γ-ray at 1436 keV has also been seen by Refs. [25,38,41–43], and found to be in coincidence with the 885 keV line in the β-decay studies of Refs. [26,40,42], the $\gamma-\gamma$ coincidences of Yoneda *et al.* [38], and the γ-ray spectroscopy following fragmentation performed by Belleguic *et al.* [43]. These findings place the second level at 2321 keV and show that it feeds the 2_1^+ state. This feeding has been treated differently in each of the $B(E2\uparrow)$ value measurements since its spin and parity are not well-known.

In 1995, Motobayashi *et al.* were the first to measure the $B(E2; 0^+_{g.s.} \rightarrow 2^+)$ for ^{32}Mg at RIKEN [12]. Two scattering experiments were performed, ^{208}Pb(^{32}Mg,^{32} Mgγ), and ^{12}C(^{32}Mg,^{32} Mgγ). The analysis assumes the second excited state in ^{32}Mg to be at 2858 keV with $J^\pi = 4^+$, as given in a shell-model calculation [44]. A coupled-channels calculation predicted that the $4^+ \rightarrow 2^+$ transition would be 5% of the $2^+ \rightarrow 0^+$ intensity and so the Coulomb excitation cross section for the ^{208}Pb(^{32}Mg,^{32} Mgγ) was reduced by 5%. To extract the $B(E2\uparrow)$ value, an average of four β_2 (β_C, which is the Coulomb deformation parameter) values were used in an ECIS79 [45] calculation for which $\beta_N = \beta_C$, one from an optical potential based on ^{17}O [46, 47], one extracted from a ^{208}Pb(^{40}Ar,^{40} Arγ) run [48] and two extracted from the ^{12}C run with the same optical potentials as the ^{17}O and ^{208}Pb(^{40}Ar,^{40} Arγ). From the average β_2 value of 0.512(44), the final $B(E2; 0^+_{g.s.} \rightarrow 2^+)$ value is 454(78) e^{2}fm^4.

In 1999, the $B(E2; 0^+_{g.s.} \rightarrow 2^+)$ for the nucleus was measured at the NSCL by Prytychenko *et al.* [25] via the intermediate-energy Coulomb excitation ^{197}Au(^{32}Mg,^{32} Mgγ). A RELEX coupled-channels calculation [49] excluded the possibility of a 2-step excitation of the 2321 keV level, and so the authors assumed that only direct excitation to that level could occur [27]. If the $B(E2\uparrow)$ value is constrained to the upper limits listed by Endt [50], the J^π for the 2321 keV level should be 1^- or 2^+. The feeding cross sections for the 1436 keV γ-ray for each of these transitions, E1 and E2 respectively, give essentially the same value, resulting in a correction of 24%. Without the correction, the $B(E2; 0^+_{g.s.} \rightarrow 2^+)$ reported is 440(55) e^{2}fm^4 in agreement with [12],

and with it 333(70) e^2fm^4. Nilsson calculations also reported by this reference report $\beta_2 \geq 0.31$ and predict that the ^{32}Mg is prolate.

In 2001, a significantly higher value for the $B(E2; 0^+_{g.s.} \rightarrow 2^+)$ for ^{32}Mg was measured via inelastic scattering by Chisté *et al.* [41]. Cross sections from both ^{208}Pb(^{32}Mg,^{32} Mgγ), and ^{12}C(^{32}Mg,^{32} Mgγ) were measured. Feeding contributions from the 2321 keV level were estimated by scaling the feeding cross-sections from all possible states of ^{24}Mg by the one-proton and one-neutron separation energies. This is based on the assumption that the total feeding cross-section should be proportional to the highest energy that still decays by γ-emission. They then extracted β_C and β_N using an ECIS94 [51] calculation with a combination of the optical potential of Barrette [47] and the proximity potential [52] and found the charge and mass deformations to be equal. Their extraction of the $B(E2; 0^+_{g.s.} \rightarrow 2^+_1)$ for ^{32}Mg is reported as 622(90) e^2fm^4 [41] in disagreement with the adopted value of 390(70) e^2fm^4. A similar inelastic nuclear scattering experiment by Mittig using a ^{28}Si target in place of the carbon also measured the 2321 keV state and claim that it is an excellent candidate for a $J^\pi = 3^-$ $1p1h$ state [53].

Although ^{32}Mg is obviously collective, the $B(E2\uparrow)$ alone cannot determine whether or not it is deformed. The ratio $E(4^+_1)/E(2^+_1)$ is one method which gives a good indication about the deformation. Higher-lying states were investigated by γ-ray spectroscopy following fragmentation by Belleguic *et al.* [43, 54, 55] in 2001. Using BaF_2 and Ge detectors, they report γ rays at 885, 1430, 2870, and 1950 keV. Their findings agree with levels predicted by shell model calculations [56] and indicate that the levels up to $J = 4$ are prolately deformed. Since the 2870 keV photon is a result of a decay directly to the ground state, it is a candidate for a second 2^+ level and indicates possible shape coexistence in ^{32}Mg. They assign $J^\pi = 4^+$ to the 2315 keV level.

Two more experimental papers in 2001 report on ^{32}Mg. Reference [39], whose main focus is ^{34}Mg, lists a $B(E2; 0^+_{g.s.} \rightarrow 2^+_1)$ value of 449(53) e^2fm^4 with no feeding correction thus reaffirming [12, 25]. Yoneda *et al.* [38] report the coincidence of the

885 keV and the 1438 keV γ-rays.

From the above review, it can be seen that there are several different measurements for the $B(E2\uparrow)$ for ^{32}Mg which are not all in agreement. Three similar values for the $B(E2\uparrow)$ are obtained from the three Coulomb excitation measurements [12, 25, 39] while the consideration of feeding of the 885 keV state by the 2321 keV state lowers the value [25]. Finally, the value obtained via inelastic scattering by [41] is clearly larger than the others.

1.5.2 Theory

The comparisons of the measured $B(E2; 0^+_{g.s.} \rightarrow 2^+_1)$ values, 454(78) e^{2}fm^4 [12], 440(55) e^{2}fm^4 [25], 449(53) e^{2}fm^4 [39], which are all similar, 333(70) e^{2}fm^4 [25] taking into account feeding of the 885 keV state by the 2321 keV state, and the high value of 622(90) e^{2}fm^4 [41], for ^{32}Mg, to shell model, Hartree Fock, mean field, and beyond mean field calculations are presented in this section. The β_2 values for the measurements are 0.51, 0.50, 0.43, 0.6, and 0.51 respectively, and are extracted according to Equation 1.8.

Shell Model

The shell model calculations explain the anomaly at $10 \leq Z \leq 12$, $20 \leq N \leq 22$ by including $n\hbar\omega$ promotions over the $1f_{7/2} - 1d_{3/2}$ gap in the ground state. The pairing interaction between neutrons seems to aid the deformation by creating valence particles and holes [44].

Wildenthal's $0\hbar\omega$ model, including only neutron sd levels in the valence space, uses an empirical effective interaction and predicts the energy of the first 2^+ state to be greater than 2 MeV. Of the shell model calculations, this prediction is the furthest from the experimental values [32]. Another $0\hbar\omega$, sd-space calculation predicts $E(2^+_1) = 1.69$ MeV, and a $B(E2; 0^+_{g.s.} \rightarrow 2^+_1)$ value of 180 e^{2}fm^4 with the deformation parameter β_2 equal to 0.32 [57]. With the same model allowing $2\hbar\omega$ promotions the

$E(2_1^+)$ value is 0.93 MeV, $B(E2\uparrow)$ value is 490 e^2fm^4 and the β_2 value 0.5 [57]. They also find that the $2p2h$ configuration dominates over the $4p4h$. Warburton *et al.* also allowed $2\hbar\omega$ configurations and obtain a $B(E2\uparrow)$ value of 340 e^2fm^4 with the β_2 value 0.44 [30]. It was also thought that mixing the $0\hbar\omega$ and $2\hbar\omega$ configurations would provide a better description of the ground state. The values obtained by Poves and Retamosa *et al.* with the full *sd-pf* valence, mixing $(0+2)\hbar\omega$ configurations, led to an $E(2_1^+)$ value of 0.3 MeV, $B(E2\uparrow)$ of 205 e^2fm^4 and β_2 of 0.34 [34]. Allowing 0 through $4\hbar\omega$ promotions for the first time, Fukunishi predicted the first excited state energy to be 1.17 MeV, the $B(E2\uparrow)$ value to be 449 e^2fm^4 and the deformation parameter β_2 to be 0.51 [44].

Other efforts have been made to reduce the valence space through Monte Carlo treatments [22, 56]. The number of p-h excitations is not restricted, intruder mixing is enhanced and angular momentum projection is used to restore the total angular momentum. The calculated results for ^{32}Mg are $E(2_1^+) = 0.885$ MeV, a $B(E2\uparrow) = 454$ e^2fm^4 and a $\beta_2 = 0.51$ [22, 56], which are very close to the measured values. This calculation indicates shape coexistence, showing four minima in the potential energy surface, as compared to the two found in many of the mean field treatments (see below). The ratio $E(4_1^+)/E(2_1^+)$ is predicted to be 2.55 by this model, which does not give preference to a rotational or vibrational configuration [22, 56] .

In summary, the shell model calculations allowing the maximal possible number of np-nh promotions and with the largest valence space give predictions closest to the experimental values. In these models, the $2p2h$ configuration dominates a configuration which promotes 2 pairs of neutrons over the gap [56].

Mean Field and Beyond

It has been suggested experimentally [43] by the existence of a possible second 2^+ low-lying state that ^{32}Mg may be a candidate for shape coexistence. Indeed in many cases, Mean-Field models agree and find more than one local minimum for the total

energy as a function of the deformation parameter in their calculations.

For the Hartree Fock models there are over 80 different Skyrme parametrizations that may be included in the self-consistent calculations [58]. A few representative models are presented here. ^{32}Mg is found to exhibit coexistence of prolate deformed and a spherical shapes in HF plus 10 different Skyrme interactions all described in [58], SLy4, SkO, SkT6, SkI4, Zσ, SkI3, SkP, SkM*, SkI1, or SkO'. The shape preference between the interactions depends on the surface coefficient where a large coefficient favors a spherical shape and the unpaired calculations give rise to a prolate minimum [58]. A density-dependent monopole plus HF also predicts mixed spherical and prolate shapes with for the prolate state, a β_2 value of 0.54, and a $B(E2\uparrow)$ value of 507 e^{2}fm^4 [59]. The nucleus is found to be spherical ($\beta_2 = 0$) with HF-Bogoliubov (HFB) +SLy4 in the transformed harmonic oscillator (THO) basis [60], and the deformed HFB calculation [61].

Relativistic Mean Field models predict a spherical shape [23, 62, 63]. Beyond the mean field, the Gogny force is used followed by the Angular Momentum Projection and Configuration Mixing (AMPCM) treatment revealing a mixture of prolate and oblate minima [64]. The quadrupole deformation parameter for the prolate minimum is calculated to be 0.36 by these models.

1.6 ^{34}Mg

1.6.1 Experimental Background

^{34}Mg has eight more neutrons than the stable ^{26}Mg, and because of this has been difficult to access experimentally until recently. The first attempts to measure the first 2^+ energy and $B(E2; 0^+_{g.s.} \rightarrow 2^+_1)$ value for ^{34}Mg were made at the NSCL in 1999 by Pritychenko *et al.* [25] via intermediate-energy Coulomb excitation ^{197}Au(^{34}Mg,^{34}Mg$\,\gamma$) in inverse kinematics. Because of the limited number of projectile nuclei, Pritychenko *et al.* were limited statistically to placing only an upper limit on the $B(E2\uparrow)$ value of

670 e^2fm^4. Recently however, upgrades to the rare-isotope beam facilities have made it possible to access the more neutron-rich members of the Island of Inversion at significantly improved intensities.

In February 2001, Yoneda *et al.* reported on the double fragmentation reaction used to access ^{34}Mg at RIKEN [38]. From the initial fragmentation of a ^{40}Ar primary beam on ^{9}Be ^{36}Si was selected and then in a second reaction fragmented on anohter ^{9}Be target. The de-excitation γ-rays from ^{34}Mg were detected in 66 rectangular NaI(Tl) crystals for γ-ray detection and silicon telescopes for the particle identification. Yoneda *et al.* report a first excited-state energy of 660(10) keV, the lowest of the region, and a second γ-ray at 1460(20) keV which was observed at rather low statistics and give a tentative J^π assignment to the second state at 2120 keV of 4^+. The ratio $E(4_1^+)/E(2_1^+)$ is then 3.2, indicating that the nucleus may be statically deformed.

In December 2001, Iwasaki *et al.* reported the $B(E2; 0^+_{g.s.} \rightarrow 2^+_1)$ value for ^{34}Mg [39]. Iwasaki *et al.* performed Coulomb excitation on 44.9 MeV/nucleon $/nuc34Mg$ also using 66 rectangular NaI(Tl) detectors and silicon telescopes for the experimental apparatus. Iwasaki *et al.* performed two experiments, one with a thick lead target for the Coulomb excitation ^{208}Pb(^{34}Mg,^{34}Mgγ) and the other with a carbon target ^{12}C(^{34}Mg,^{34}Mgγ) to determine the nuclear excitation contribution to the cross section. With the ECIS calculation they determine the deformation parameter β_2 to be 0.58(6) after averaging over four values obtained in a similar fashion to Motobayashi above. To extract the $B(E2\uparrow)$ value, an average of 4 β_2 (β_C, which is the Coulomb deformation parameter) values were used in an ECIS79 [45] calculation, one from an optical potential based on ^{17}O [46, 47], one extracted from a ^{208}Pb(^{40}Ar,^{40}Arγ) run [48] and two extracted from the ^{12}C run with the same optical potentials as the ^{17}O and ^{40}Ar. In the end, they report a first 2^+ energy at 656(7) keV and the large $B(E2; 0^+_{g.s.} \rightarrow 2^+)$ value of 631(126) e^2fm^4.

1.6.2 Theory

Comparisons of the measured $E(2_1^+)$, $B(E2; 0_{g.s.}^+ \rightarrow 2_1^+)$, and β_2 values 0.660(10) MeV [38]; 0.656(7) MeV, 631(126) e^2fm^4, 0.58(6) [39]; and < 670 e^2fm^4 [25] for ^{34}Mg to shell model, Hartree Fock, mean field, and beyond mean field calculations are presented in this section.

Shell Model

In the $0\hbar\omega$ *sd* shell model of Ref. [57], the $E(2_1^+)$ value is calculated to be 1.09 MeV, the $B(E2\uparrow)$ value to be 375 e^2fm^4 , and the β_2 value to be 0.45. The same model with $2\hbar\omega$ promotions to the *fp* shell gives an $E(2_1^+)$ value of 0.660 MeV, a $B(E2\uparrow)$ value of 655 e^2fm^4 , and a β_2 value of 0.6. In the Quantum Monte Carlo Shell Model (QMCSM) calculation for ^{32}Mg [56], the first excited state energy $E(2_1^+)$ is calculated to be 0.620 MeV, the $B(E2\uparrow)$ value to be 570 e^2fm^4 , and the quadrupole deformation parameter β_2 to be 0.55. Both the QMCSM and the $2\hbar\omega$ shell model predict that this nucleus is very collective and possibly statically deformed. However, while the $2\hbar\omega$ model of Ref. [30] predicts the limit of the island to be ^{34}Mg at $N = 22$, the QMCSM extends the line to $N = 24$ [56].

Mean Field and Beyond

The Hartree-Fock calculations for ^{34}Mg generally predict it to be prolate deformed with a β_2 value of 0.3-0.4 (HF+Skyrme) [58], 0.22 (DHFB) [61], 0.46 with a $B(E2\uparrow)$ value of 404 e^2fm^4 (density dependent monopole) [59]. Stoitsov predicts an oblate shape with a β_2 value of -0.1 (HFB+Sly4, THO) [60].

RMF models predict either a prolate deformed nucleus with a β_2 value of 0.3 [63] or one that is close to being spherical with the deformation parameter equal to 0.162 [62] and 0.17 [23]. The AMPCM predicts it to have the same deformation parameter as ^{32}Mg, a value of 0.36 [64].

In general, both shell model and mean field models calculate values for the deformation parameter β_2 which indicate ^{34}Mg is deformed and prolate in shape. The shell models predict a larger degree of collectivity for ^{34}Mg than ^{32}Mg while several of the mean field models above calculate similar values for the reduced transition probability and the quadrupole deformation parameter between the two nuclei.

1.7 Experiment Objective

The focus of our experiment was the measurement of the energy of the first 2^+ level and the reduced transition probability $B(E2; 0^+_{g.s.} \rightarrow 2^+_1)$ for the $N = 22$ nucleus ^{34}Mg. The nucleus is predicted to be a boundary of the Island of Inversion by the $2\hbar\omega$ shell model [30], and is expected to exhibit the $4p2h$ intruder state as its ground state configuration, with a large $B(E2\uparrow)$ value and a low first excited state energy [56]. In order to accomplish the measurement, we utilized intermediate-energy Coulomb excitation to populate the 2^+_1 state of ^{34}Mg, and by measuring the de-excitation γ-rays were able to extract the energy and probability for the quadrupole transition. The method also allows the simultaneous measurement of the de-excitation γ-rays from the other nuclei in the secondary cocktail beam, and so we also set out to measure ^{35,36}Al and ^{37}Si. A secondary goal was the measurement of the $E(2^+_1)$ and $B(E2\uparrow)$ values, again via Coulomb excitation, for the $N = 20$ nucleus ^{32}Mg. ^{26}Mg and ^{96}Mo served as test cases for the Coulomb-excitation studies.

Chapter 2

Method

2.1 Coulomb Excitation

The technique of intermediate-energy Coulomb excitation is used in experimental nuclear structure physics with exotic beams [14]. Through scattering, the interaction of a projectile and target via their Coulomb fields produces excited states in both projectile and target nuclei. For pure Coulomb excitation, the subsequent de-excitation of the nuclei is an electromagnetic transition whose probability can be measured. These probabilities along with the γ-ray energies give important information about the energy level structure of both of the nuclei (Section 1.2). The process is ideal in that it is almost completely model-independent, though it does depend on the model of intermediate-energy Coulomb excitation, and through inverse kinematics provides a method with which to measure these electromagnetic properties for neutron-rich and neutron-deficient nuclei which cannot be made into long-lived targets. Coulomb excitation has been widely used, with particular success for the investigation of light neutron-rich isotopes, for example [25, 29, 65]. The developments by Winther and Alder [66] in which the semi-classical straight line approximation is adapted to relativistic energies are necessary for the rare-isotope beams studied in the present work, and the main points of the theory are outlined here. Discussions and applications can

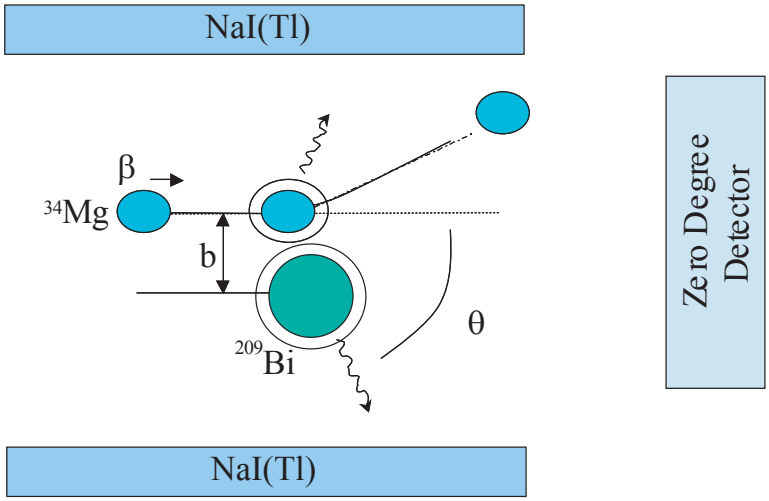

Figure 2.1: A depiction of the Coulomb excitation process for ^{34}Mg on ^{209}Bi. The angle of emission, θ, of the γ-ray and the impact parameter, b are shown. The NaI(Tl) γ-ray detectors and particle detector (zero degree detector) are also shown for this experiment.

be found in Refs. [12, 14, 27, 67–71].

Coulomb excitation was originally developed by considering the excitation of a target (Z_2) in the field of a projectile (Z_1) [3, 72]. However, it may also be thought of in the inverse situation, simply by exchanging the target nucleus and the projectile nucleus as in the following outline. Figure 2.1 depicts the Coulomb excitation setup.

2.1.1 Relativistic Coulomb Excitation at Intermediate Energies

Since intermediate-energy radioactive beams have velocities ($v/c \approx 0.3$-0.4) which are above the classical limit, relativistic effects must be considered both in the Coulomb excitation mechanism and, as outlined in Section 2.2.6, the detection of the de-excitation γ-rays. The relativistic quantities β and γ are defined as

$$\gamma = \frac{1}{\sqrt{1-(\beta)^2}}, \qquad \text{and} \quad \beta = \left(\frac{v}{c}\right). \tag{2.1}$$

In the relativistic limit, the adiabaticity parameter is the ratio of the collision time and the time of internal motion of the nucleus,

$$\xi(b) = \omega_{fi}\frac{b}{v\gamma}, \tag{2.2}$$

where $\omega = E_{fi}/\hbar$ and E_{fi} is the difference in excitation energies between the final and initial states. The impact parameter b is

$$b = \frac{a_0}{\gamma} cot\left(\frac{\theta_{cm}}{2}\right), \tag{2.3}$$

where

$$a_0 = \frac{Z_2 Z_1 e^2}{m_0 v^2}, \tag{2.4}$$

and m_0 is the reduced mass of the projectile and target, $m_0 = m_1 m_2/(m_1 + m_2)$. At intermediate beam energies the straight-line trajectory assumed for a relativistic projectile is modified by the recoil of the target. As a result, the impact parameter b is modified to

$$b + \frac{\pi a_0}{2\gamma}. \tag{2.5}$$

In the theory of intermediate-energy Coulomb excitation, the Coulomb excitation cross section is written [66]

$$\sigma_{i\to f} = \left(\frac{Z_2 e^2}{\hbar c}\right)^2 \sum_{\pi\lambda\mu} k^{2(\lambda-1)} \left(B_2(\pi\lambda, J_i \to J_f)/e^2\right) \left| G_{\pi\lambda\mu}\left(\frac{c}{v}\right)\right|^2 g_\mu(\xi(b_{min})), \tag{2.6}$$

where

$$g_\mu(\xi) = \pi\xi^2 \left[|K_{\mu+1}(\xi)|^2 - |K_\mu(\xi)|^2 - \frac{2\mu}{\xi} K_{\mu+1}(\xi) K_\mu(\xi)\right] \tag{2.7}$$

are the Winther and Alder functions which are written in terms of modified Bessel functions K_μ. The $G_{\pi\lambda\mu}$ for the electric case ($\mu \geq 0$ and $\pi = E$) are

$$\begin{aligned} G_{E\lambda\mu}\left(\frac{c}{v}\right) &= i^{\lambda+\mu}\frac{\sqrt{16\pi}}{\lambda(2\lambda+1)!!}\left(\frac{(\lambda-\mu)!}{(\lambda+\mu)!}\right)^{\frac{1}{2}}\left(\left(\frac{c}{v}\right)^2-1\right)^{-\frac{1}{2}} \\ &\times\left(\frac{(\lambda+1)(\lambda+\mu)}{2\lambda+1}P^{\mu}_{\lambda-1}\left(\frac{c}{v}\right)-\frac{\lambda(\lambda-\mu+1)}{2\lambda+1}P^{\mu}_{\lambda+1}\left(\frac{c}{v}\right)\right), \end{aligned} \tag{2.8}$$

and for the magnetic case ($\mu \geq 0$ and $\pi = M$)

$$G_{M\lambda\mu}\left(\frac{c}{v}\right) = i^{\lambda+\mu+1}\frac{\sqrt{16\pi}}{\lambda(2\lambda+1)!!}\left(\frac{(\lambda-\mu)!}{(\lambda+\mu)!}\right)^{\frac{1}{2}}\left(\left(\frac{c}{v}\right)^2-1\right)^{-\frac{1}{2}}\mu P^{\mu}_{\lambda}\left(\frac{c}{v}\right), \tag{2.9}$$

where the P^{μ}_{λ} are the associated Legendre polynomials.

An adiabatic cutoff sets in for $\xi = 1$. Below the cutoff, the collision time becomes shorter than the time it takes to excite the nucleus. In this limit, the cross section may be approximated as

$$\sigma_{\pi\lambda} \approx \left(\frac{Z_2 e^2}{\hbar c}\right)^2 \frac{B(\pi\lambda, 0\rightarrow\lambda)}{e^2 b_{min}^{2\lambda}}\pi b_{min}^2 \begin{cases} (\lambda-1)^{-1} & \text{for } \lambda \geq 2 \\ 2\ln(\frac{b_{max}}{b_{min}}) & \text{for } \lambda = 1 \end{cases} \tag{2.10}$$

which shows the proportionality

$$\sigma_{i\rightarrow f} \propto B(\pi\lambda). \tag{2.11}$$

Thus, the $B(\pi\lambda)$ can be extracted directly from the measurement of the Coulomb excitation cross section through detection of the number of de-excitation γ-rays. Experimentally, this cross section is determined by

$$\sigma_{CE} = \frac{N_\gamma^e}{N_t N_p}. \tag{2.12}$$

where N_γ^e is the number of de-excitation γ-rays emitted, N_t is the number of target

nuclei, and N_p is the number of projectile nuclei. The constraint of b such that the majority of the γ-rays detected result from Coulomb excitation requires practical considerations which will be discussed in Section 2.2.4.

2.1.2 Angular Distributions

Coulomb excitation results in a non-isotropic distribution of de-excitation γ-rays. This is important for detection considerations which will be discussed in Section 3.1.4. The derivation of the γ-ray angular distribution may be found in [70, 72] with final results presented here.

The γ-ray angular distribution is given by

$$\begin{aligned} W(\theta_{cm}) &= \sum_{\substack{k\,even,\,\mu \\ L,\,L'}} \left| G_{\lambda\mu}\left(\frac{c}{v}\right)\right|^2 g_\mu(\xi)\,(-)^\mu \begin{pmatrix} \lambda & \lambda & k \\ \mu & -\mu & 0 \end{pmatrix} \\ &\quad \times \begin{Bmatrix} I_f & I_f & k \\ \lambda & \lambda & I_i \end{Bmatrix} F_k(L, L', I_f, I_f)\,\sqrt{2k+1}\,P_k(\cos(\theta_{cm}))\,\delta_L\,\delta_{L'}. \end{aligned} \tag{2.13}$$

where g_μ are the Winther and Alder functions of Equation 2.7, $P_k(cos(\theta))$ the Legendre polynomials, the $\delta_L\,\delta_{L'}$ are Kronecker Delta functions, and the $\gamma-\gamma$ correlation functions $F_k(L, L', I_i, I_f)$ are given by

$$\begin{aligned} F_k(L, L', I_1, I_2) &= (-)^{I_1+I_2-1}\sqrt{(2k+1)(2I_2+1)(2L+1)(2L'+1)} \\ &\quad \times \begin{pmatrix} L & L' & k \\ 1 & -1 & 0 \end{pmatrix} \begin{Bmatrix} L & L' & k \\ I_2 & I_2 & I_1 \end{Bmatrix}. \end{aligned} \tag{2.14}$$

The relation is generally expressed

$$W(\theta_{cm}) = \sum_{k\,even} a_k P_k(\cos(\theta_{cm})). \tag{2.15}$$

These angular distributions are folded with the intrinsic efficiency of the γ-ray detectors for the final photopeak efficiency used in determining the number of γ-rays

emitted from the Coulomb-excited state.

2.2 Experiment

The experiment was performed at the National Superconducting Cyclotron Laboratory at Michigan State University and designated NSCL experiment 01017. The recent coupling of the two superconducting cyclotrons, the K500 cyclotron to the K1200 cyclotron, has made extremely exotic nuclei such as ^{34}Mg accessible at statistically significant intensities [13]. The facility layout is displayed in Figure 2.2. The primary beams are accelerated in the K500 cyclotron, and then injected into the K1200 cyclotron. Upon injection into the K1200 superconducting cyclotron they are stripped of the majority of their electrons, and subsequently accelerated to final energies. The advantage of the coupled system over the K1200 in stand-alone mode is the production of primary beams with greater intensities at higher energies. This results in a higher number of secondary fragment products and thus better statistics for experimenters. The fragment separator was also upgraded from the A1200 to the A1900 by increasing the angular acceptance of the beam line. As one of the first experiments to utilize beams produced by this new Coupled Cyclotron Facility (CCF), Coulomb excitation of three different secondary beams and two degraded primary beams was performed. The experiment apparatus was set up in the N3 vault. An array of 24 NaI(Tl) detectors (the APEX array [73, 74]) was used for γ-ray detection, a fast/slow plastic phoswich detector and PIN Si detectors for particle identification, and two parallel plate avalanche counters (PPACs) for beam location.

2.2.1 The Rare-Isotope Beam

Two primary beams were used over the course of the experiment. ^{48}Ca ions were produced in the room temperature ECR source ARTEMIS by heating solid ^{48}Ca with a resistive heating element mounted radially on the plasma chamber [75]. The

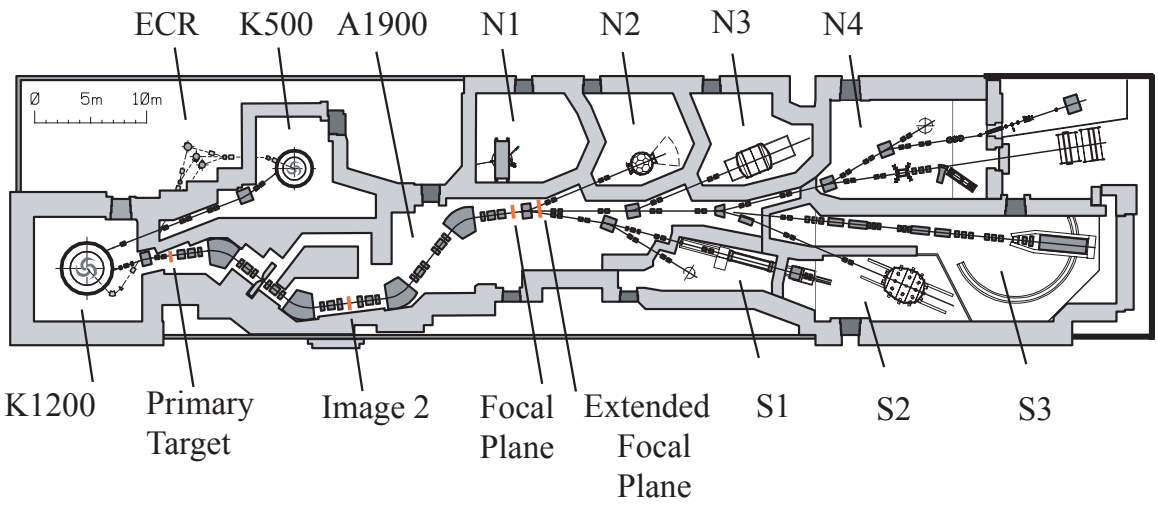

Figure 2.2: The Coupled Cyclotron Facility at the NSCL. The experiment was performed in the N3 vault.

ions were first accelerated to 10 MeV/nucleon in the K500 and then injected into the K1200 where they were immediately stripped to a charge state of 19^+ by a 0.2 mg/cm^2 ^{12}C foil. After stripping, the primary beam was accelerated to a final energy of 110 MeV/nucleon. The radio frequency (RF) of the cyclotrons was 21 MHz (a period of 47.5 ns) and the intensity of the ^{48}Ca primary beam was on average 15 pnA. ^{96}Mo was also utilized as a test case for the experimental setup. The ions were produced by sputtering. They were stripped to a charge state of 38^+, and accelerated to 110 MeV/nucleon.

Three separate secondary beams and the two degraded primary beams were studied. The three cocktail beams were produced by fragmentation of the $^{48}Ca^{19+}$ primary beam on a primary target of ^{9}Be. The ^{9}Be primary target was also used to degrade the ^{48}Ca and ^{96}Mo primary beams. The nuclei of interest were selected from the fragmentation products with the A1900 fragment separator [76]. The beam characteristics (grouped by secondary beam) for ^{26}Mg and ^{27}Al; ^{32}Mg and ^{33}Al; ^{34}Mg, ^{35,36}Al and ^{37}Si; and the degraded ^{96}Mo and ^{48}Ca are listed in Table 2.1. At the dispersive focal plane (Image 2) of the A1900, a 116 mg/cm^2 aluminum wedge reduced the number of light nuclei that would reach the focal plane and physical slits allowed particles to be

Table 2.1: Secondary beam parameters for NSCL experiment 01017. Bρ_5 is the rigidity of the beamline to the N3 vault at the exit of the A1900. The thicknesses of the primary fragmentation target ^{9}Be are given in mg/cm^2. The intensity is measured in the N3 experimental vault as is N_B, the number of projectile nuclei. The amount of energy prior to interaction with the secondary target is also listed.

Nucleus	Bρ_5 (Tm)	^{9}Be (mg/cm^2)	Intensity (N3) (particles/s)	Total N_B (particles)	Energy (MeV/nucleon)
^{26}Mg	2.822	376	5500	2.51×10^8	78.6
^{32}Mg	3.531	587	150	5.25×10^6	81.1
^{34}Mg	3.637	795	8	2.14×10^6	76.4
^{35}Al	3.637	795	23	6.22×10^6	84.2
^{36}Al	3.637	795	11	3.06×10^6	79.8
^{37}Si	3.637	795	21	5.39×10^6	87.3
^{48}Ca	3.127	587	9750	1.30×10^8	71.2
^{96}Mo	2.723	376	14100	1.44×10^8	67.1

filtered by their momentum. Particle identification was accomplished by measuring energy loss in a PIN Si detector located at the focal plane, and the time-of-flight with respect to the K1200 cyclotron's radio frequency as shown in Figure 2.3. After the desired nuclei were selected, they were guided to the N3 vault and energy loss was again recorded in a second PIN Si detector, which was retracted for the main experiment. Spectra from the the N3 PIN and the A1900 PIN were compared to ensure integrity of the beam. During one transmission test, the beam transmission was approximately 55% from the A1900 focal plane to the PIN Si detector in N3 for ^{34}Mg with a primary beam intensity of 7 pnA and and a production rate of 0.36 pps/pnA. On average, the ^{34}Mg cocktail composition in N3 was 11% ^{34}Mg, 33% ^{35}Al, 22% ^{36}Al, and 34% ^{37}Si.

2.2.2 Coulomb Excitation Targets

For a Coulomb excitation experiment, the ideal target has a high Z and is monoisotopic. Since both projectile and target nuclei are excited in the process, the energy of the target's de-excitation γ-rays, as well as its Coulomb excitation cross sections, must be considered. Because the target peaks are broadened in the frame of the

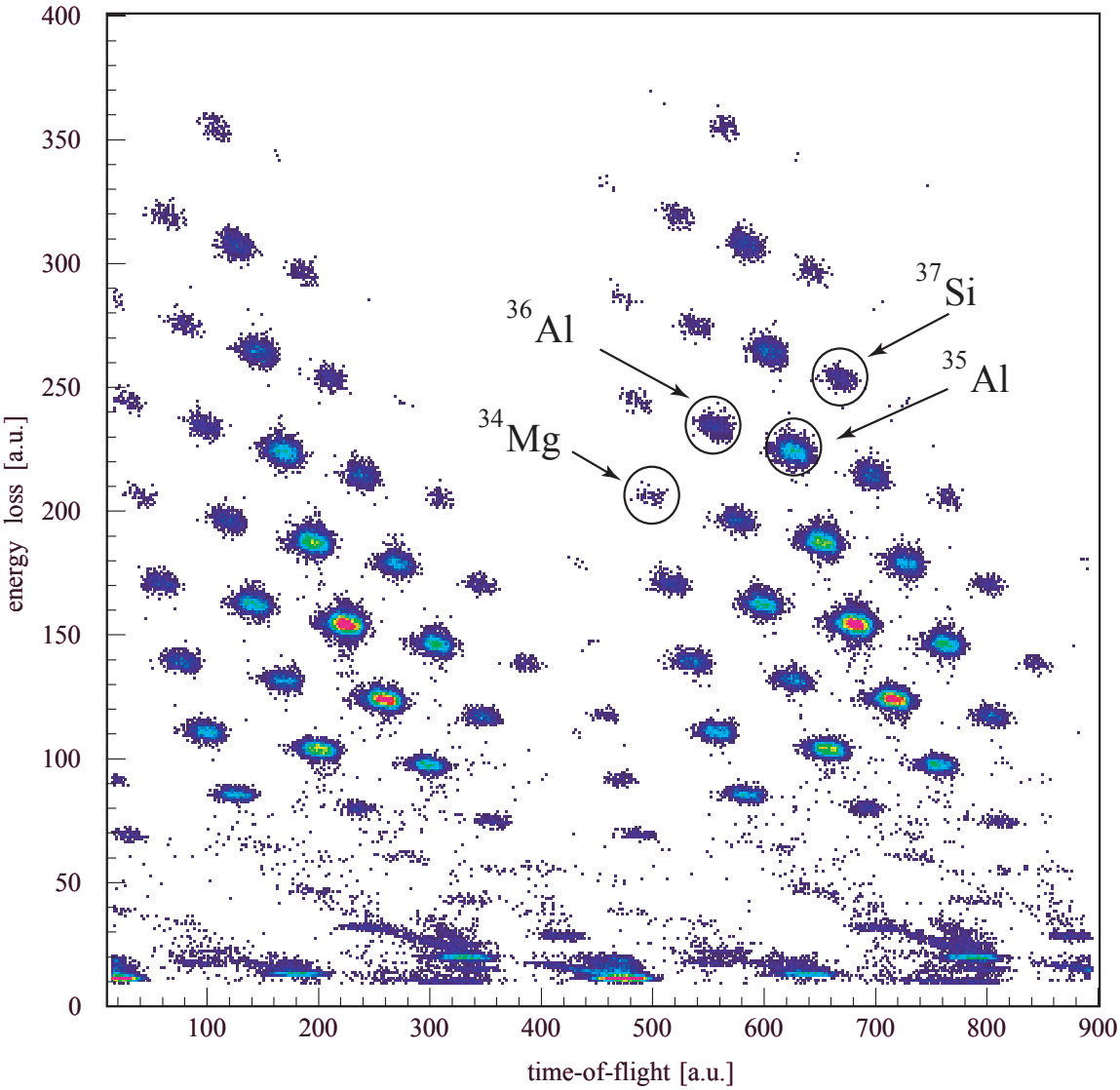

Figure 2.3: The particle identification at the focal plane of the A1900 fragment separator for the ^{34}Mg cocktail beam. The energy loss was measured with a 470 mg/cm^2-thick PIN Si detector and is plotted versus time-of-flight in arbitrary units. Two rf pulses are shown and the nuclei selected for the Coulomb excitation experiment are labelled for one of the pulses only.

projectile, they have the potential to interfere with the analysis of the projectile de-excitation γ-ray, especially if the Coulomb excitation cross section for the target is relatively large. If the energy does not interfere however, the energy and reduced transition probability obtained for the transition in the target through the analysis of the laboratory-frame spectrum can sometimes be a good test case. A common choice for the Coulomb excitation target is ^{197}Au [25, 28] for its high Z.

Table 2.2: The Coulomb excitation targets, cross sections, and expected detected number of target de-excitation γ-rays (N_γ^d, where d indicates detected versus emitted) are listed for each projectile nucleus.

Target	Thickness (mg/cm^2)	N_{target}	Projectile	N_{proj} (particles)	Cross section (mb)	Expected N_γ^d
^{209}Bi	980	2.82×10^{21}	^{26}Mg	2.51×10^{8}	0.25(3)	45
			^{34}Mg	2.14×10^{6}	0.40(4)	0.359
			^{35}Al	6.22×10^{6}	0.47(5)	1.23
			^{36}Al	3.06×10^{6}	0.46(5)	0.599
			^{37}Si	5.39×10^{6}	0.51(5)	1.17
			^{48}Ca	1.30×10^{8}	0.62(6)	33.9
^{197}Au	968	2.96×10^{21}	^{32}Mg	5.25×10^{6}	20(2)	90

The number of target nuclei is determined by

$$N_{target} = d \cdot \frac{1}{\mathcal{M}} \cdot N_A, \tag{2.16}$$

where d is the surface mass density of the target in g/cm^2, $\mathcal{M}$ is the molar mass in mol/g of the target material, and N_A is Avogadro's number.

In this experiment, a target of ^{197}Au was used for the ^{32}Mg and ^{96}Mo beams and a target of ^{209}Bi for the ^{26,34}Mg and ^{48}Ca beams. ^{197}Au has an adopted $B(E2;3/2^+ \rightarrow 7/2^+)$ value of 4488(408) e^{2}fm^4 for the 547.5(3) keV transition from the ground state to the first $7/2^+$ state [77]. The expected cross section extracted from these values for this transition in the Coulomb excitation reaction with ^{32}Mg (parameters are listed in Table 2.3) is 20(2) mb, which corresponds to an expected 90 counts to be detected in the photopeak. In contrast, ^{209}Bi has an adopted $B(E2;9/2^- \rightarrow 7/2^-)$ value of 80(9) e^{2}fm^4 for the 896.28(6) transition [78], yielding an expected cross section of 0.40(4) mb for the ^{34}Mg reaction. Due to the small cross section, the number of counts in the ^{209}Bi de-excitation photopeak was also expected to be small at 0.36 counts total in the reaction with ^{34}Mg spread over a range of 715 keV to 1256 keV. The small contribution is negligible in the estimation of the background for the analysis as

described in Section 4.2. The ^{209}Bi was chosen so that the target 547.5(3) keV γ-ray would not interfere with any photopeaks in the projectile frame with the anticipated 660(10) keV ^{34}Mg photon [38]. The interference by the 547 keV γ-ray from the ^{197}Au target in the projectile-frame spectrum of ^{32}Mg can be seen in Figure 2.10. The number of target nuclei in both the ^{209}Bi and ^{197}Au targets used here are listed in Table 2.2, Coulomb excitation cross sections and expected number of de-excitation γ-rays.

2.2.3 Particle and Gamma-ray Detection

After completing the isotope identification, the N3 PIN was retracted and the nuclei were focused through 2 PPACs onto the secondary target. Gamma rays produced from the resulting reactions were detected with an array of 24 position-sensitive NaI(Tl) detectors first used as part of the trigger for the Atlas Positron EXperiment (APEX) collaboration at Argonne National Laboratory [73, 74] (the APEX array). The scattered particles were stopped in a 4-inch-diameter fast/slow plastic phoswich detector centered at zero degrees (ZDD) which is described below. The setup is displayed in Figure 2.4.

Gamma-ray Detection

In order to accomodate the low intensities expected for the ^{34}Mg secondary beam, γ-ray detection was accomplished with an array of NaI(Tl) detectors. While segmented germanium detectors such as the SeGA array at the NSCL [79] have better energy resolution, the NaI(Tl) crystals are significantly more efficient. For a 660 keV γ-ray, SeGA has a photopeak efficiency of 3.6% for $v/c = 0.35$ with 8 detectors at a scattering angle of 90° and 7 detectors at a scattering angle of 37° [80] while the photopeak efficiency for a γ-ray of the same energy and v/c of 0.36 for the NaI(Tl) array used here is 22%.

The NaI(Tl) array was recently brought to the NSCL from Argonne National

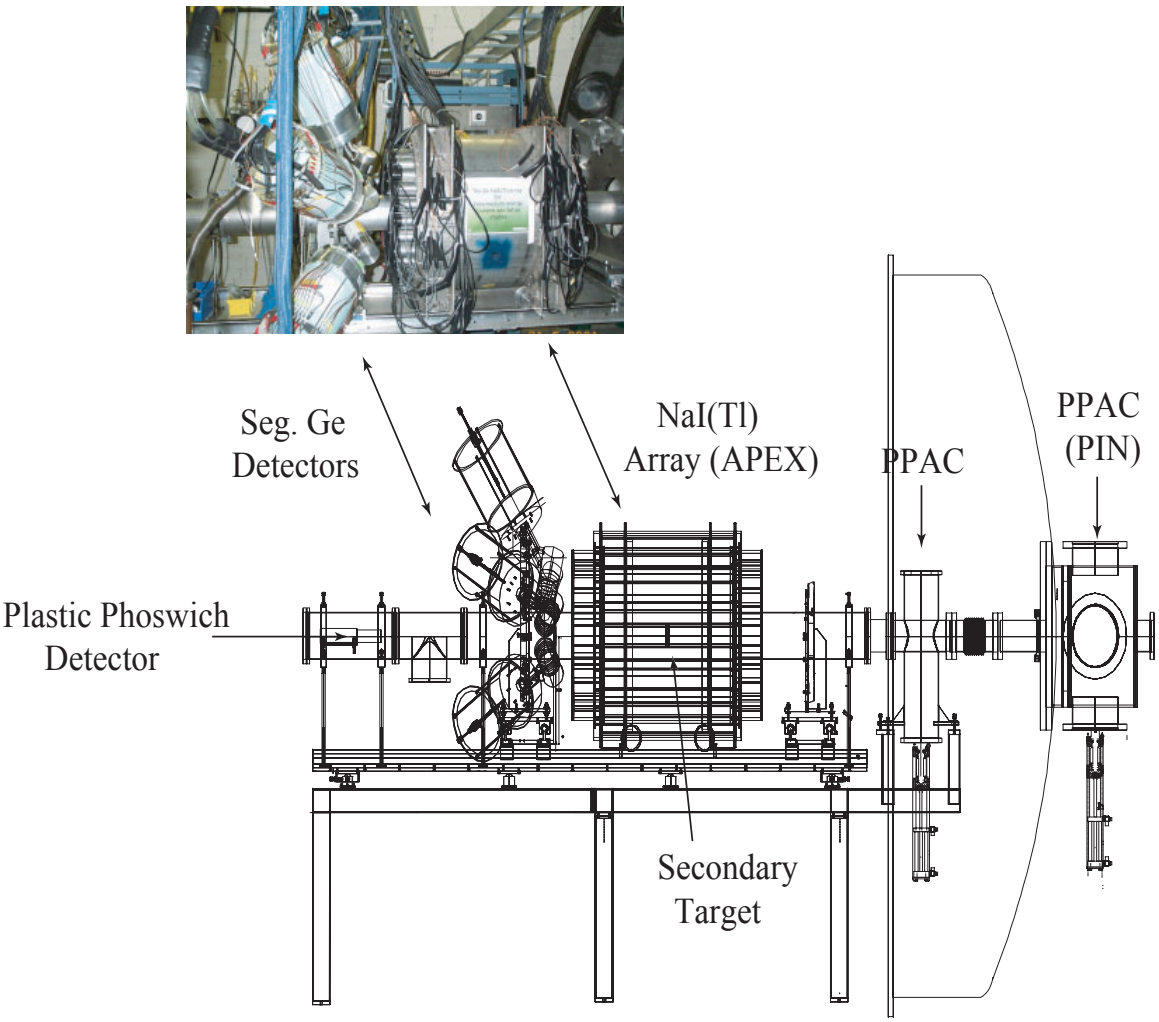

Figure 2.4: The Coulomb excitation detector setup as explained in Section 2.2.3. Although segmented germanium detectors (a portion of SeGA [79]) remained in the vault after a previous experiment, they were not used for this experiment.

Laboratory and cleaned and reassembled by B.C. Perry [74]. The array is shown in Figure 2.5 and consists of 24 long, trapezoidal NaI(Tl) crystals with photomultiplier tubes (PMTs) at each end to facilitate position sensitivity. The dimensions of each crystal are 55.0 x 6.0 x 5.5(7.0) cm^3 (L x H x W). They are encased in an evacuated 0.4 mm thick stainless steel housing. At each end of the crystal, there are 1.1 cm thick quartz windows that are 4.4 cm in diameter. Hamamatsu H2611 PMTs were used in order to reduce gain drifiting due to the high magnetic fields present in the experiment at Argonne, although that feature was not necessary for this application. The PMTs are 5.08 cm in diameter and coupled with optical couplant to the quartz

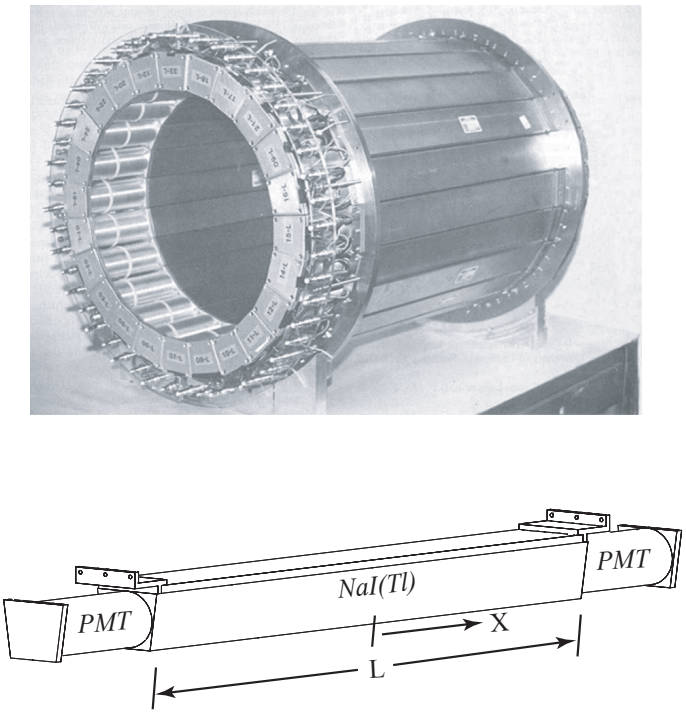

Figure 2.5: The APEX NaI(Tl) array. The top panel shows the assembled array without shielding. The bottom panel indicates the length L and the photon-interaction position X for a single detector.

windows. Light-tight PMT shields cover the junctions.

Exponential light attenuation in each crystal is achieved by diffusing the surface of the crystal via grinding and coating the crystal with an optical reflector. The diffusion causes the angle of reflection to be independent of the angle of incidence and the selection of the coating allows adjustment of the attenuation coefficient while maintaining the energy resolution of the detector [73].

Because the light attenuation is exponential, the energy of the γ-ray and position of its interaction with the crystal can be reconstructed from the PMT signals. Above 100 keV, a γ ray interacting with the NaI(Tl) produces a number of scintillation photons, N_S, proportional to the energy deposition [81]. Below 100 keV, the number of scintillation photons N_S produced is no longer linearly related to the energy deposition. We assume that half the scintillation photons contribute to the signal in each of

the PMTs. The number of photoelectrons released from the photocathodes are

$$N_{PE,d} \propto \frac{N_S}{2} e^{-\mu(L/2+X)} \qquad (2.17)$$
$$N_{PE,u} \propto \frac{N_S}{2} e^{-\mu(L/2-X)}$$

where $N_{PE,d}$ and $N_{PE,u}$ are the number of photoelectrons released from the downstream PMT and the upstream PMT respectively, X is the distance of the interaction point measured from the center of the crystal, L is the length of the crystal, and μ is the attenuation coefficient (see Figure 2.5).

The pulse heights of each of the PMTs (Y_u and Y_d) are proportional to the number of scintillation photons N_S by a factor dependent on the gain of the electronics,

$$Y_d \propto N_{PE,d} \qquad (2.18)$$
$$Y_u \propto N_{PE,u}.$$

The PMTs are gain matched by placing a ^{60}Co collimated source (also used for the position calibration see Section 3.1.1) at the center of the array and first adjusting the PMT biases so that the output signal amplitudes match on an oscilloscope. The dispersion is fine-tuned by adjusting shaper gains to the range desired, in this case 2 keV/channel [74]. Gain matching is important in order to avoid loss of dynamic range in the amplifier.

After gain matching, position and energy can be reconstructed from the pulse heights:

$$X = \frac{1}{2\mu} \left[\ln \frac{Y_u}{Y_d} \right], \qquad (2.19)$$

and

$$E = \sqrt{Y_u Y_d}. \qquad (2.20)$$

The position and energy calibrations, efficiency, and energy and position resolutions

are discussed further in Chapter 3. For a position resolution of 3.0 cm, the attenuation coefficient is $\mu = 0.047\text{cm}^{-1}$ [73] and the energy resolution (FWHM/centroid) for a section at the center of the array is 16% for the sum of all the detectors at 662 keV.

When the array is assembled, the detectors are arranged in a cylinder supported by two stainless steel rings. The inner diameter of the array is 42.8 cm, the outer diameter is 56.7 cm and it is shielded by a steel case and lead plates. For γ rays originating from the center, 75% of 4π is covered over the full length of the detectors.

Some of the physical features detract from the energy resolution of the APEX array. Near the ends of the detectors, optical-light collection efficiency decreases due to the trapezoidal shape. The junctions between the NaI(Tl) crystal, the quartz window and the PMT also cause a loss of light due to the size mismatch.

Particle Detection

After passing through the PPACs for relative beam position monitoring, and interacting with the secondary target, projectiles were detected by a fast/slow plastic phoswich detector (ZDD) [82]. The maximum scattering angle θ_{max} was determined by the detector placement. The ZDD provides a means for projectile identification and counting as well as allowing the constraint of the impact parameter (Section 2.2.4). The ZDD must be carefully placed in the beam pipe to ensure centering on the beam axis, and correct distance from the target.

The ZDD is 10 cm (4 inches) in diameter and consists of two thin (1.5 and 1 mm) pieces of BC400 fast plastic and a thick (100 mm) piece of BC444 slow plastic covered in mylar and black tape to prevent light leakage. The thickness of the fast plastic was chosen such that 19% energy was lost for ^{34}Mg, and 24% for ^{32}Mg. The estimate was simulated using LISE [83] and SRIM [84] with the material BC400 (polyvinyltoluene with an H to C atom ratio of 1.103). The plastic is optically coupled through a light guide to two THORN EMI PMTs [82]. Particles detected in the detector are identified by their energy loss in the fast plastic vs. time of flight, or the full energy deposited

in the slow plastic vs. time of flight. Both signals can be detected with one PMT by pulse shape discrimination.

Over the course of the experiment, several target changes were made including scintillation targets for beam tuning and the actual Coulomb excitation targets. In order to conserve beam time, it was important to make these changes as quickly as possible. Because the only access to the secondary target was from the downstream end of the setup, beyond the ZDD placement, it was also important to position and remove the ZDD itself as quickly as possible with the smallest uncertainty. To accomodate this, an Al frame to support the ZDD within the beam pipe was constructed such that the ZDD could be levelled on the x-z plane prior to placement in the beam pipe, where z is the beam axis, and x is the horizontal direction. In previous experiments, it was necessary to adjust the vertical and horizontal positions for each corner of the detector each time it was placed in the beam pipe. This was a tedious process and took a substantial amount of time.

The frame is displayed in Figure 2.6. It consists of two 1.27 cm thick Al rings 23.5 cm in diameter and 20.32 cm apart. They are connected by a 23 x 11 x 2 cm^3 level Al platform. Two identical carts with wheels were constructed to fit into grooves on the platform. The alignment cart holds wire crosshairs spaced 16.5 cm from a pin hole drilled in a block normal to the cart surface. It is displayed in the top panel of Figure 2.6. The ZDD cart holds the zero degree detector and is displayed in the bottom panel of Figure 2.6. The center of the ZDD face corresponds exactly to the center of the crosshairs and pin hole on the alignment cart.

In order to align the ZDD to the beam axis, the frame was inserted into the beam pipe with the alignment cart in place. The crosshairs and pin hole were then lined up with a beam telescope further downstream that had previously been centered on the beam axis. This was accomplished by adjusting the vertical and horizontal position of the platform of the frame via one dial for the vertical adjustment and two screws for the horizontal adjustment. Since the platform on the frame and the beam

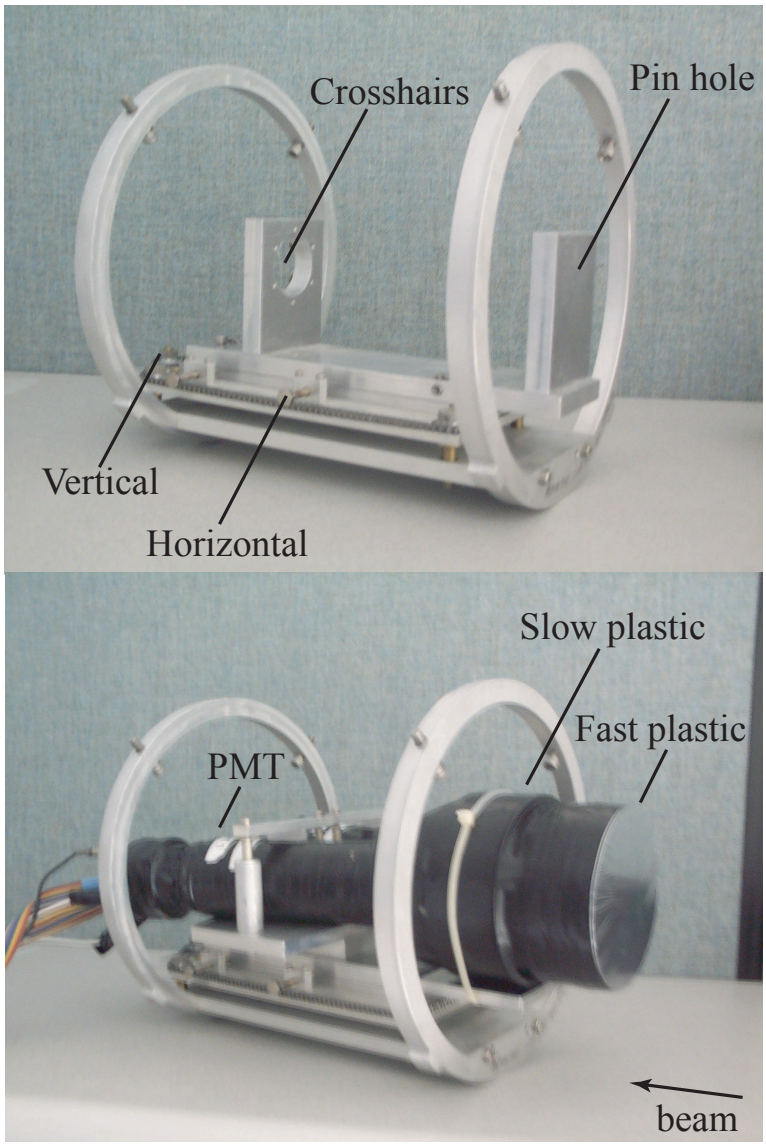

Figure 2.6: The zero degree detector and positioning frame. The frame is shown in the top panel with the alignment cart in place. In the bottom panel, the alignment cart has been replaced with the zero degree detector on the ZDD cart.

pipe were levelled in advance of the experiment, only one set of horizontal and vertical adjustments was necessary. After the frame was aligned, the alignment cart was easily removed and the ZDD cart with the zero degree detector was put in its place on the frame, cables were connected, the beam pipe evacuated and the experiment continued along in an efficient fashion.

Table 2.3: Impact parameters for NSCL experiment 01017. The energy, v/c, and b_{min} are values at the middle of the secondary target. θ_{cm}^{max} is the maximum scattering angle in the projectile frame.

Nucleus	Energy (MeV/nucleon)	v/c	θ_{max}^{cm} (deg)	b_{min} (fm)
^{26}Mg	66.8	0.36	2.68	20.4
^{32}Mg	71.9	0.37	2.63	15.4
^{34}Mg	67.3	0.36	2.77	15.5
^{35}Al	74.4	0.38	2.78	14.7
^{36}Al	70.1	0.37	2.79	15.2
^{37}Si	77.1	0.38	2.80	14.5
^{48}Ca	51.0	0.32	2.93	24.2
^{96}Mo	55.9	0.34	3.69	20.3

2.2.4 Coincidences and Constraint of the Minimum Impact Parameter

In order to exclude direct nuclear reactions from the recorded data, the impact parameter must be constrained such that no events are accepted at parameters less than the sum of the target and projectile radii plus two to four fm [85]. This minimum impact parameter b_{min} (Equation 2.3) is related to the maximum laboratory angle by

$$\theta_{lab}^{max} = \frac{2Z_1 Z_2 e^2}{\gamma m_1 v_1^2} \frac{1}{b_{min}} \tag{2.21}$$

where the projectile is denoted by the subscript 1 and the target by 2, and lab indicates the laboratory frame. The radii can be estimated by $R = 1.25A^{1/3}$ fm. In order to practically accomplish this constraint, the zero degree detector is placed at a distance that limits θ_l^{max} to a value dictated by Equation 2.21 through

$$\tan \theta_{lab}^{max} = \frac{R}{L}, \tag{2.22}$$

where R is the radius of the plastic phoswhich detector, and L is the distance from the plastic phoswich detector to the target. The master trigger is (particle AND γ)

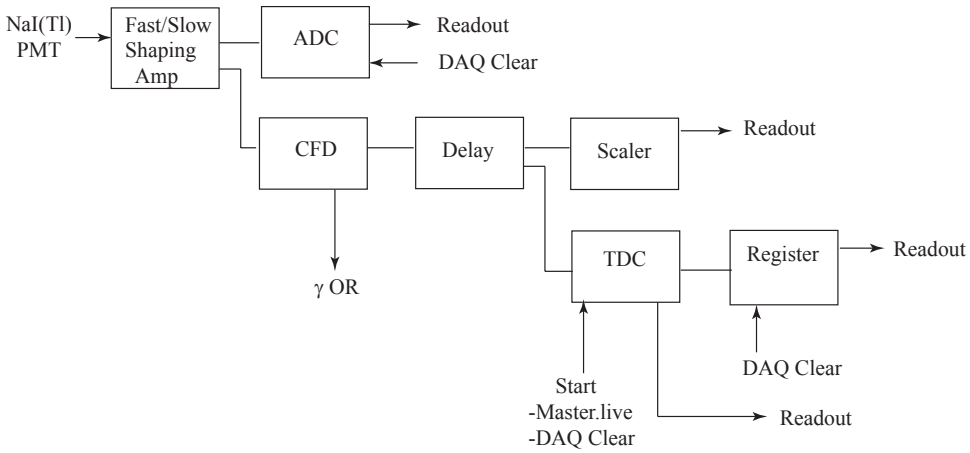

Figure 2.7: The basic electronics layout for the APEX NaI(Tl) array.

OR (downscaled particle) and binning of the γ rays is performed by placing a software gate on the appropriate particle and using that as a condition for sorting γ rays. θ_{cm}^{max} and b_{min} are listed in Table 2.3 for the nuclei studied in this work. The software gates are discussed in Section 3.2.

2.2.5 Data Flow

Detector signals were processed by a series of nuclear electronics which were read out by the SpectroDAQ data acquisition system and sorted utilizing SpecTcl [86] both online and offline.

The APEX array

The electronics diagram for the APEX array is shown in Figure 2.7. The γ-ray interaction with the NaI(Tl) crystal produces scintillation photons which are converted to photoelectrons by the PMTs at each end of the crystal. Signals from both photomultiplier tubes for each detector in the APEX NaI(Tl) array were sent to CAEN N568B shaping amplifiers. The slow branch of the signal was digitized by Phillips Scientific model 7164H peak-sensing 16-channel analog to digital converters (ADCs) and then read out for the energy information. The fast pickoff signal was directed to LeCroy 3420 16-channel constant fraction discriminators (CFDs) for discrimination.

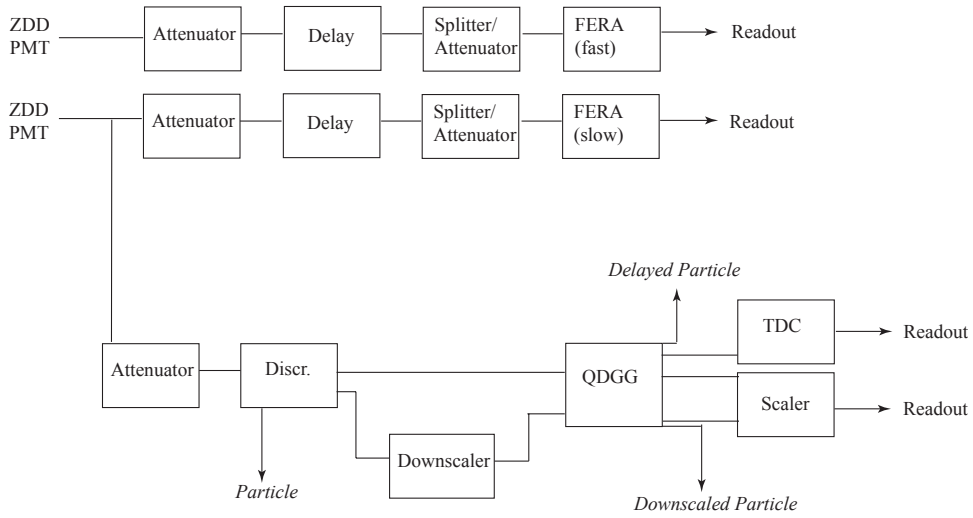

Figure 2.8: The basic electronics layout for the zero degree detector. The particle, downscaled particle, and delayed particle are indicated.

The logic-or was sent to the trigger logic unit (P/S 752) as the APEX OR. It was also delayed and split to a 4434 scaler module which was read out and a 16-channel 7186H P/S time to digital converter (TDC). The TDC was read out and the signal from the TDC was sent to a LeCroy 4448 bit register and read out.

Thresholds were placed on the CFDs such that, for a certain detector, if any one PMT signal was above the threshold, and the trigger was set, both PMTs' energy and time signals were read out. The thresholds were different for every detector, but were set to exclude signals below the ^{133}Ba line at 356 keV. The gain was set in the ADCs such that the shapers began to saturate at 2 MeV.

The ZDD

The zero degree detector electronics are shown in Figure 2.8. Signals from both of the PMTs on the zero degree detector were also read out. For the energy information, the signal was sent to a splitter. Each of these signals was then attenuated (Lecroy A101 attenuator), delayed by 500 ns, and sent through an MSU splitter/attenuator to a Lecroy 4300B FERA (fast encoding readout ADC), one for the slow signal, and the other for the fast and subsequently read out. The timing information signal was

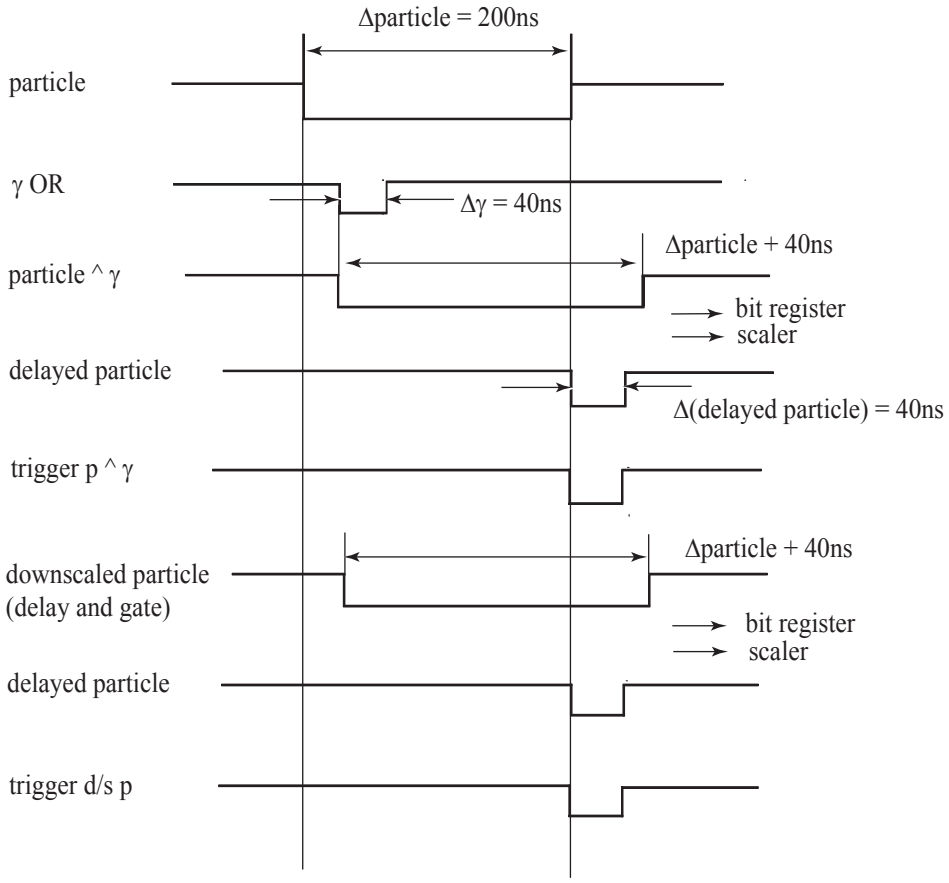

Figure 2.9: The gate widths for the trigger logic. OR is indicated by ^, particle by p and downscaled by d/s. The final Master.live is an AND of the trigger d/s p and the data aquisition not busy.

sent to a discriminator (P/S 711) and split. One signal went to the trigger logic unit as the *Particle* signal. Another signal went to a downscaler, an MSU quad gate and delay generator (QDGG) and then the trigger logic unit as the *Downscaled Particle* signal. Another went directly to the QDGG and was delayed. The delayed signal was sent to the logic unit as the *Delayed Particle* and also to a P/S 7186 TDC and the readout as the stop. The *Particle*, *Downscaled Particle*, and *Delayed Particle* signals were all read out as scalers.

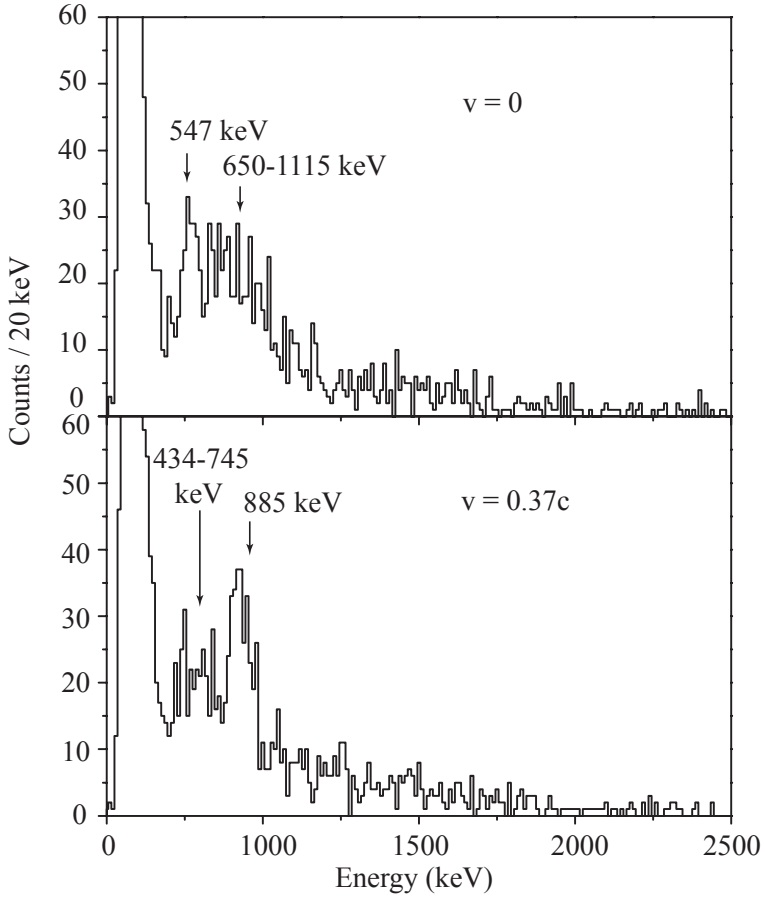

Figure 2.10: Energy spectra for ^{32}Mg demonstrating the Doppler reconstruction. The top panel is the energy spectrum without Doppler reconstruction. The target de-excitation γ-rays are prominent while the 885 keV γ-rays from the projectile are smeared over 500 keV. The bottom panel shows measured energies that have been reconstructed event-by-event in the moving frame of the projectile. Gamma-rays originating in the projectile are seen as a prominent peak, while the photopeak from the target nuclei is broadened.

Triggers

The trigger timing is shown in Figure 2.9. Phillips Scientific 752 and 755 4-fold logic units were used to set the live trigger. The Master.live was the particle-γ coincidence ((((γ-OR AND particle) OR (downscaled particle)) AND delayed particle) AND NIM not busy. The NIM busy gate start was Master.live OR data aquisition not busy. The stop was the data aquisition clear. The γ-OR was an OR between the APEX CFDs.

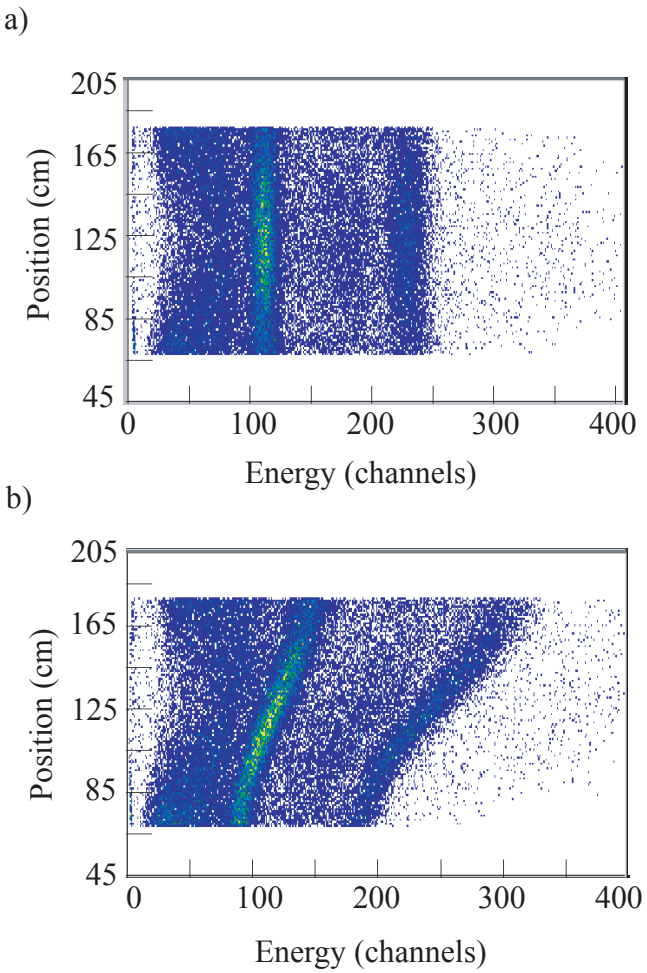

Figure 2.11: Position-versus-energy spectra for decay γ-rays emitted from ^{88}Y (898 and 1836 keV). The spectrum is shown without Doppler reconstruction of the energy in Panel a), and in panel b) the γ-ray energies are reconstructed in the projectile frame. The position is measured in the laboratory frame in both spectra. The energy dispersion is 8 keV/channel.

2.2.6 Consideration of Relativistic Effects

Because intermediate-energy radioactive beams have velocities above the classical limit, experimenters utilizing them must consider relativistic effects. In particular, de-excitation γ-rays originating in the projectile nucleus are detected in the laboratory frame. In order to obtain the energy of the γ-rays originating from the projectile at their values in the rest frame of the projectile, the change in frequency from one inertial frame to the next is taken into consideration.

A full development of the relativistic kinematics pertinent to experiments at intermediate energies can be found in [70]. The results utilized in this experiment will be summarized here. The collision of a projectile moving at $\beta = v/c$ with a stationary target is described by the following relationships between angles and energies of the massless photons in the center of mass (cm) and laboratory (lab) frames:

$$\begin{aligned} \tan\theta_{cm} &= \frac{\sin\theta_{lab}}{\gamma\left(\cos\theta_{lab} - \beta\right)} \\ \tan\theta_{lab} &= \frac{\sin\theta_{cm}}{\gamma\left(\cos\theta_{cm} + \beta\right)}, \end{aligned} \tag{2.23}$$

and

$$\begin{aligned} \mathrm{E}_{cm} &= \gamma E_{lab}\left(1 - \beta\cos\theta_{lab}\right) \\ \mathrm{E}_{lab} &= \gamma E_{cm}\left(1 + \beta\cos\theta_{cm}\right). \end{aligned} \tag{2.24}$$

The observables for the experiment are the energies and positions of the γ-rays detected in the laboratory frame. For purposes of illustration, the relationships between energy, scattering angle and velocities in the laboratory and projectile rest-frames can be thought of in the following manner. For the target (tar), $v = 0$ with respect to the lab frame and

$$E_{lab}^{tar} = E_{cm}^{tar}. \tag{2.25}$$

On the other hand, the projectile (pro) has some velocity v with respect to the laboratory frame and the quantity detected is

$$E_{lab}^{pro} = \gamma E_{cm}^{pro}\left(1 + \beta\cos\theta_{cm}^{pro}\right). \tag{2.26}$$

In order to determine the energy of the γ-rays originating from the projectile, the

observed E_{lab}^{pro} must be boosted to the projectile frame which is moving at velocity v:

$$E_{cm}^{pro} = \gamma E_{lab}^{pro} \left(1 - \beta \cos\theta_{lab}^{pro}\right). \tag{2.27}$$

There are uncertainties in the measurement of β, and the angle θ_{lab} which make small contributions to width of the energy peak. Section 3.1.3 discusses the energy resolution of the APEX array in detail, and Table 3.2 lists the contributions to the overall width of the energy peak by these uncertainties in β and θ_{lab}.

Gamma-rays originating from the target can also be boosted to the projectile frame moving at v:

$$E_{cm}^{tar} = \gamma E_{lab}^{tar} \left(1 - \beta \cos\theta_{lab}^{tar}\right). \tag{2.28}$$

This effect broadens the energy in the laboratory frame for the projectile and in the projectile frame for the target.

Chapter 3

Data Analysis

After the experiment, a detailed analysis of the raw data leads to the final Coulomb excitation cross section:

$$\sigma_{CE} = \frac{N_\gamma^e}{N_t \cdot N_p}, \tag{3.1}$$

where N_γ^e is the number of emitted de-excitation γ-rays, N_t is the number of target nuclei, and N_p is the number of incoming beam nuclei. In order to arrive at the final cross section, the energy and emission angle of the de-excitation γ rays detected by the APEX NaI(Tl) array are sorted event-by-event in coincidence with the projectile nuclei. These bombarding nuclei are also identified and counted. The overall analysis involves characterization of the NaI(Tl) array, data sorting, fitting and error analysis.

3.1 Characterization of the APEX NaI(Tl) Array

In order to examine previously unmeasured nuclei, the γ-ray detectors must be understood. Calibrations for both energy and position are performed and the energy resolution and efficiency of the array are carefully examined.

3.1.1 Calibrations

The first step in the data analysis is the calibration of the APEX NaI(Tl) array. Position and position-dependent energy calibration data taken before the test ^{96}Mo beam, and before and after the main experiment are processed through calibration routines. The results are then included in SpecTcl for the analysis of the data collected in the experiment. Calibration procedures are outlined below.

Position Calibration

Position-sensitivity of the γ-ray detectors becomes important for experiments at intermediate energies. Beam velocities such as those utilized here ($\beta \approx .4c$) require that energies of the de-excitation γ-rays be Doppler corrected, and therefore the angle of emission of the γ-ray must be known (see Equation 2.24). This emission angle can be determined from the position information given by the APEX NaI(Tl) array, whereby the point of γ-ray interaction with the crystal is reconstructed from the photomultiplier tube signal strengths (see Section 2.2.3). Position calibrations are performed immediately before and after the experiment.

A position calibration is carried out by placing a 10.45 μCi ^{60}Co source in a collimator and making measurements of the 1332 keV γ-ray along the length of the array [65, 82]. The collimator is made up of two Heavymet cylinders which are 14 cm in diameter and 7.62 cm long, with a 4.6 mm gap between the two cylinders. Heavymet is an alloy made of tungsten copper and nickel. The collimator is equipped with rollers and a long bar to facilitate movement inside the beam pipe (see Figure 3.1).

With some effort, the collimator is placed inside the beam pipe at the upstream end of the array, and data is taken at 47 positions in 1.27 cm increments through to the downstream end of the array. The detector multiplicity is restricted to 1, meaning that events are not accepted if more than one discriminator triggers. The length increments are measured with a measuring tape attached to the long bar on

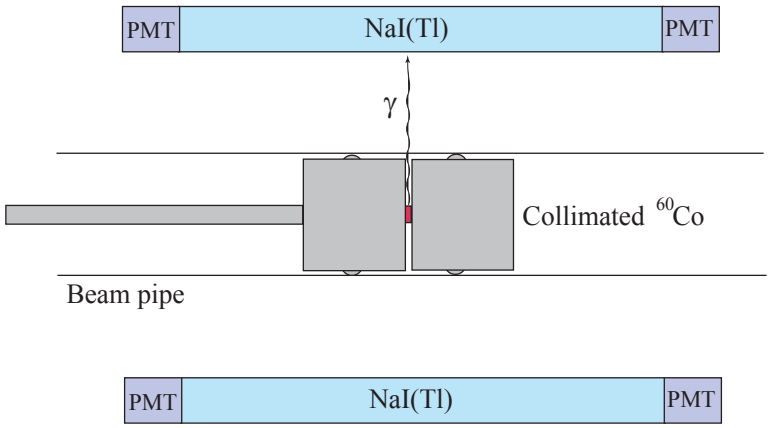

Figure 3.1: Longitudinal section depicting the position calibration for the APEX NaI(Tl) array.

the collimator. At each position, data is taken simultaneously by all 24 detectors for approximately 5 minutes. This follows closely the method used in [82].

The position is reconstructed from the measured pulse heights of both upstream and downstream photomultiplier tubes (PMTs) [73, 74]. (See section 2.2.3). In this experiment we used the expression,

$$P_R = 2000 + 1000 \log_{10}\left(\frac{Y_u}{Y_d}\right), \tag{3.2}$$

where P_R is the reconstructed position, Y_u is the signal from the upstream PMT and Y_d is the signal from the downstream PMT. Centroids of the position spectra are determined for all 47 positions for each of the 24 detectors using the fitting program GF2 [87]. The reconstructed position is then calibrated to the actual physical position through the position calibration routine. The routine utilizes a Tcl [88, 89] script to extract GF2 fit information, and Physica [90] to make the fits of the calibration curves.

As an example, the position calibration is shown for Detector 16 in Figures 3.2 and 3.3. Figure 3.2 shows the relationship between the reconstructed position and the physical position. The light collection at the ends of the detectors is non-uniform, and so portions of the detectors at each end have been excluded from the calibration and do not enter into the data analysis. The amount of crystal excluded depended

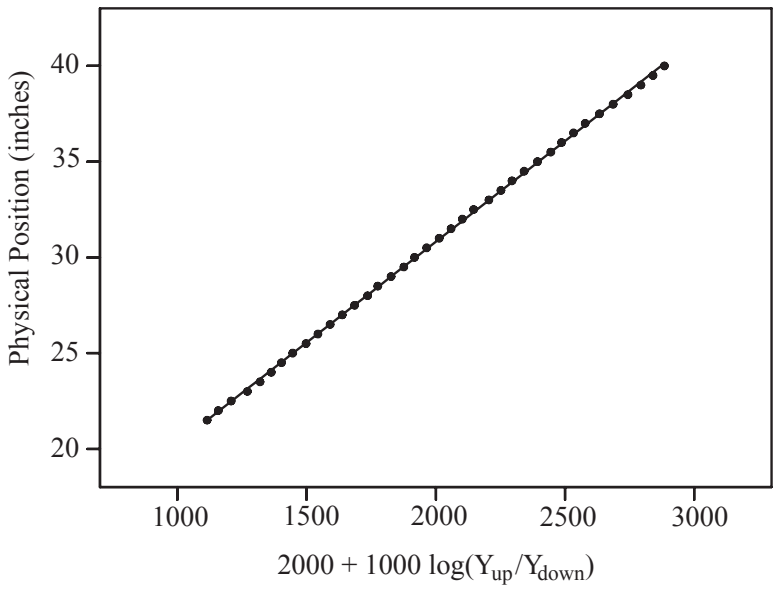

Figure 3.2: The position calibration for Detector 16 of the APEX NaI(Tl) array. There is a linear dependence between the physical and reconstructed positions.

on the detector itself, and was on average 7 cm at each end. The fit is linear for the remainder of the positions (shown). Figure 3.3 shows position spectra for several intervals at the center of the detector. The position resolution ($FWHM/centroid$) is approximately 3 cm.

The position calibration makes it feasible to bin SpecTcl parameters by position interval. The position intervals are referred to as "slices" and are created by placing software gates on the calibrated reconstructed position spectra along the longitudinal axis of the detectors. Each detector can be virtually divided into any number of these slices. For any quantity, such as the γ-ray energy, the sum of all the individual slice spectra for one detector will result in the total spectrum for that detector. The sum may also be performed for one slice over all the detectors, as is done to create the efficiency rings (see Section 3.1.4). By dividing the data in this way, it is possible to consider the position dependence of the raw energy, take into account any imperfect detector segments, and as mentioned, partition the array virtually into efficiency rings.

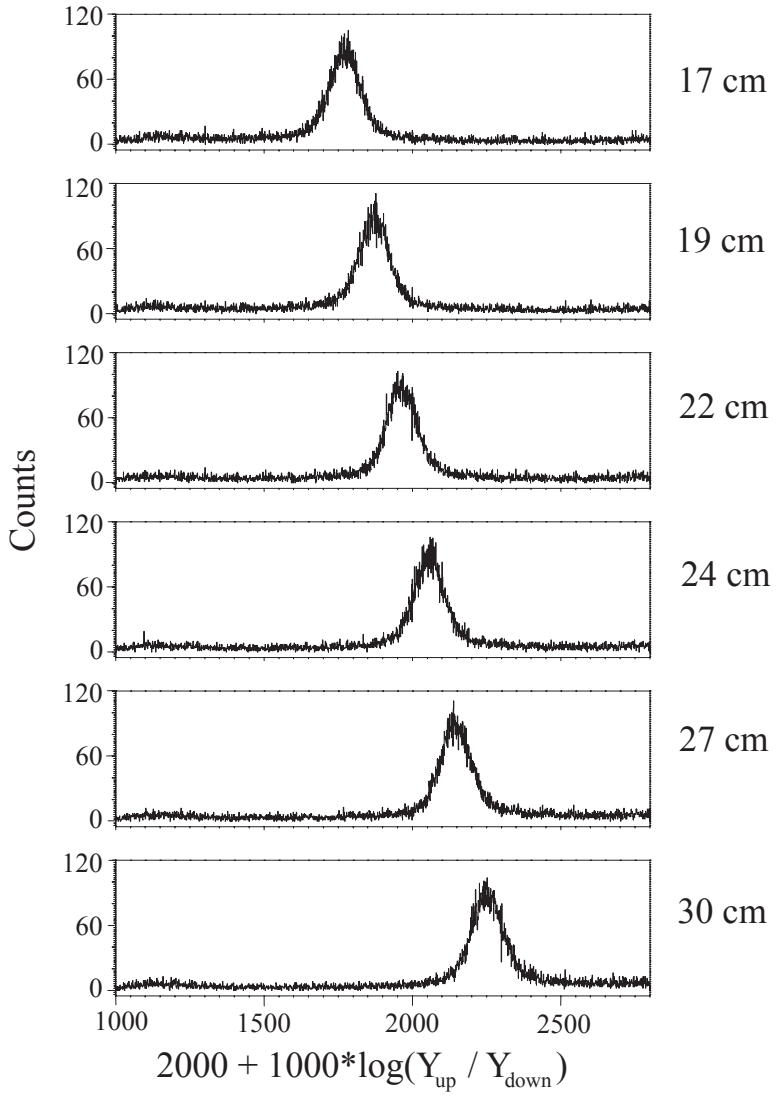

Figure 3.3: Representative reconstructed position spectra for Detector 16. These are a sample from the central region of the detector. The positions in the right margin indicate the actual physical distance from the downstream end of the array.

Source	Serial Number	Energy (keV)	A_0 (μCi) (Date)	Branching Ratio	Calibration
^{203}Hg	kf301	279.2	2.00(8) (12/1/01)	0.81	Energy/Efficiency
^{133}Ba	kf297	356.0	1.06(3) (12/1/01)	0.62	Efficiency
^{137}Cs	Z7097	661.7	1.03(4) (6/15/01)	0.85	Energy/Efficiency
^{54}Mn	kf302	834.8	1.05(3) (12/1/01)	0.99	Energy/Efficiency
^{88}Y	kf304	898.0	1.03(3) (12/1/01)	0.90	Energy/Efficiency
^{88}Y	kf304	1836.1	1.03(3) (12/1/01)	0.96	Energy/Efficiency
^{228}Th	E2881	2614.5	13.91(63) (10/1/88)	0.36	Energy/Efficiency

Table 3.1: Calibration sources used in the energy and efficiency calibrations. The branching ratios for the two Yttrium lines reflect the multiplicity 1 condition. A_0 is the initial activity of the source at the date listed.

Position-Dependent Energy Calibration

To accomodate the division into slices, the energy calibration must be position dependent; every position for each detector must have its own energy calibration. For this experiment, one position interval is approximately 2.54 cm wide and 24 slices were calibrated per detector. It was assumed that there were no unresponsive portions in the middle of the crystals, and of the 24 slices, the only slices excluded were those excluded by the position calibration.

The position-dependent energy calibration is carried out by placing a known radioactive source at the secondary target position in the center of the array and measuring decay γ-rays for 2-6 hours. Data is taken separately for several different sources over a range of energies, again with multiplicity 1. The sources used in this experiment are listed in Table 3.1.

The energy is reconstructed from the raw signals of the upstream (Y_u) and downstream (Y_d) PMTs (see also Section 2.2.3) as E_R,

$$E_R = \sqrt{Y_u \cdot Y_d}. \tag{3.3}$$

Centroids of the reconstructed energy spectra are fit with GF2 [87], and calibrated

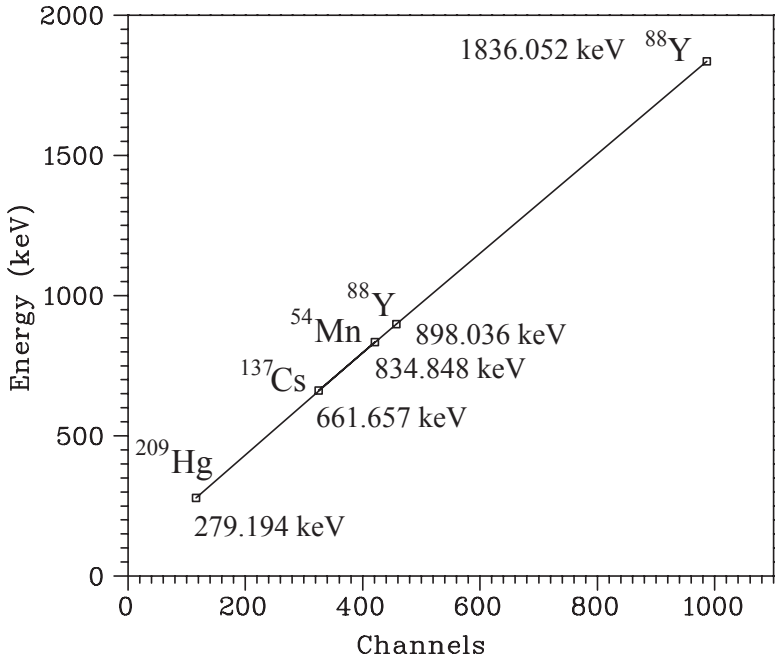

Figure 3.4: The position-dependent energy calibration for one slice in Detector 7 of the APEX NaI(Tl) array. This particular slice is approximately 18 cm upstream of the center of the array. Gamma-ray sources are indicated.

to the actual γ-ray energy with a position-dependent energy calibration routine. As with the position calibration, the routine makes use of Tcl scripts and Physica to arrive at the final energy calibration coefficients.

Examples of the energy calibration for Detector 7, Slice 1700 are shown in Figures 3.4 and 3.5. The slice number is simply a naming convention, and the location of slice 1700 is actually 18 cm upstream from the center of the array. Figure 3.4 shows the actual calibration over the range of γ-ray energies used. The fit is first-order. Reconstructed energy spectra for the ^{137}Cs and ^{88}Y sources are shown in Figure 3.5 with the corresponding decay schemes. The gain was set such that there were 2 keV/channel in the ADCs. The importance of the position-dependence of the calibration is shown in Figure 3.6. Over the entire array, there were 21,000 peaks fit in total to accomplish the calibration.

After the calibration data is taken and processed through the calibration routines, the position and position-dependent energy calibration coefficients are written to XML files which are incorporated into the SpecTcl code.

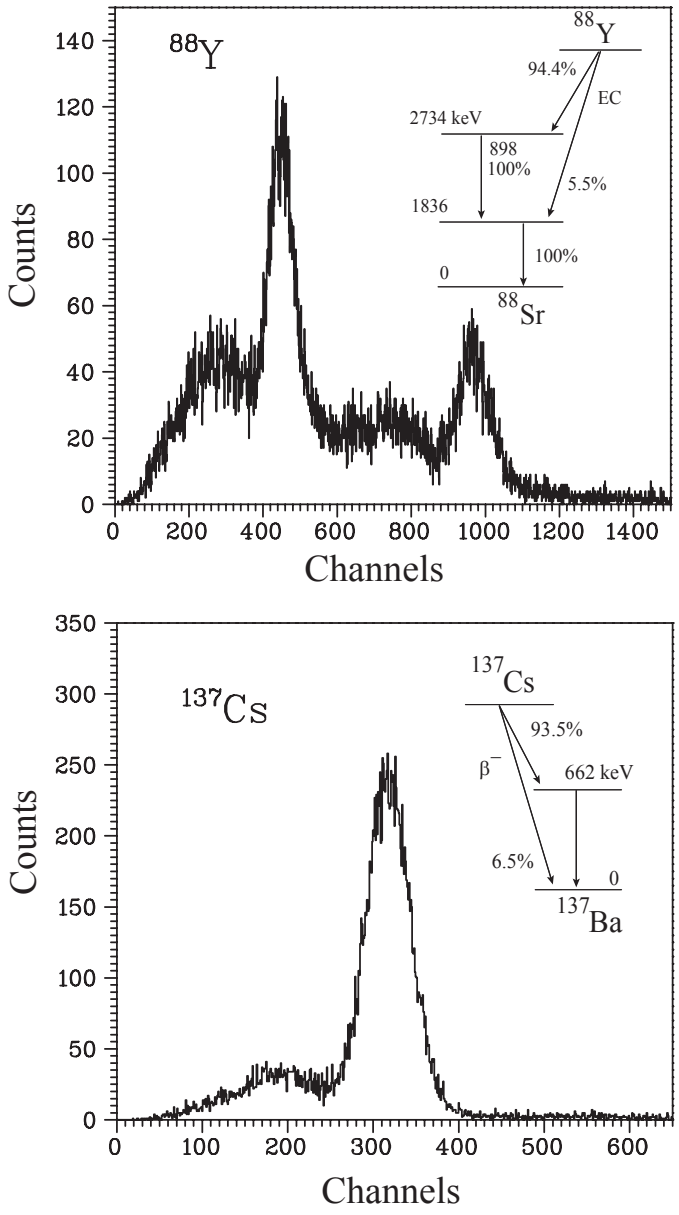

Figure 3.5: Reconstructed energy spectra for the sources ^{88}Y and ^{137}Cs as measured with one slice of the APEX NaI(Tl) detector number 17. The slice is 18 cm upstream of the center of the array. The corresponding level diagrams are shown. The dispersion is 2 keV per channel.

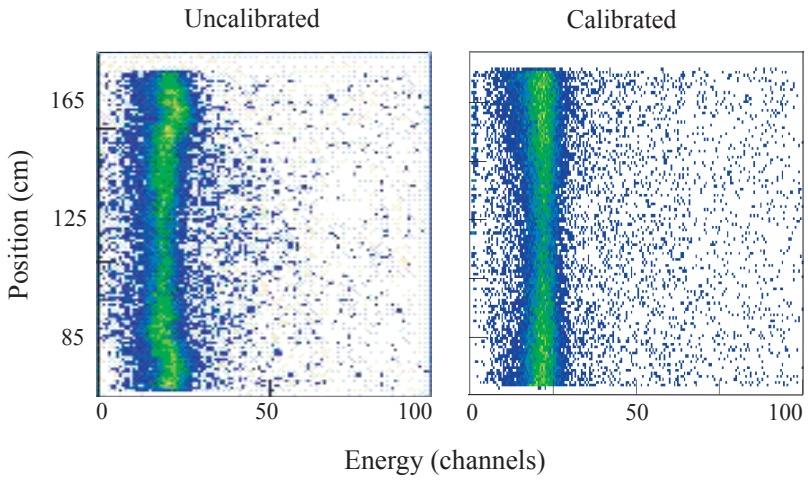

Figure 3.6: The position vs. energy plots for Detector 18. The ^{133}Ba line at 356 keV is shown on the left in the uncalibrated spectrum and on the right in the calibrated spectrum. The dispersion is 16 keV/channel.

3.1.2 In-beam Energy Calibration

The initial energy calibration was performed as outlined above with the data taken from calibration sources. A second energy calibration was performed using the energy of the de-excitation γ-rays from the projectile nuclei ^{26}Mg, ^{32}Mg and the target ^{197}Au, at 1808 keV, 885 keV and 547 keV respectively. These are all well-known energies [17, 77]. The relationship was again linear for the spectra contracted by 20:

$$y = 0.0483x + 0.0846 \tag{3.4}$$

where x is the channel number, and y is the energy in keV.

3.1.3 Energy Resolution

Resolving the energy of the detected γ rays is another important part of the data analysis. The response of a scintillation detector such as NaI(Tl) is expected to be imperfect [81]. In other words, the energy emitted is detected not as a single energy, but rather as a range of energies with a Gaussian distribution. The resolution, R is defined as the full width at half the maximum height $FWHM$ of this distribution

divided by the centroid H_0 of the same distribution.

$$R \equiv \frac{FWHM}{H_0}. \tag{3.5}$$

The energy resolution R in a scintillation detector is discussed in [81], and summarized here. Charge collection statistics, electronic noise, variations in detector response over the volume of the detector, fluctuations in PMT gains may all contribute to the response. In general, beyond the intrinsic resolution of the crystal, charge collection statistics in the PMTs are the most significant additional factor in determining the resolution. Although these factors are beyond the scope of this work, it can be shown that the gain of the APEX detectors did not fluctuate over the course of the ^{34}Mg run by comparing the centroids of the reconstructed energy peaks for all slices of detector both before and after the experiment.

For detectors with a complicated shape, such as the trapezoidal crystals that make up the APEX NaI(Tl) array, the uniformity in the light collection is not as great as that of a crystal with a simple shape, and as a result, the energy resolution R broadens. For example, the resolution of a 662 keV line for a solid right cylinder of NaI coupled to a PMT can be about 6-7% [81]. For a crystal with a well, this resolution increases by 3% [81], and for a long cylinder the resolution is about 8% [65]. In the present work with the APEX NaI(Tl) array, the resolution at 662 keV is measured to be 18%. Energy resolutions of the APEX array were also measured in two previous reports [73, 74] which are discussed below.

As is also discussed in [81], the intrinsic energy resolution is dependent on the γ-ray energy. For a scintillator with a simple shape, the energy resolution should be inversely proportional to the square root of the γ-ray energy,

$$R = \frac{C}{\sqrt{E_\gamma}}, \tag{3.6}$$

where C is a constant of proportionality, and E_γ is the γ-ray energy. When crystals

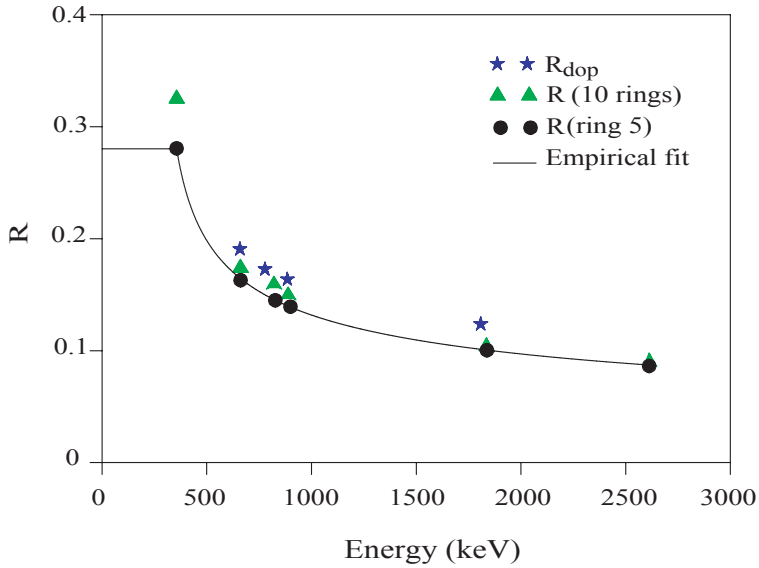

Figure 3.7: Energy resolution R for APEX NaI(Tl) source measurements for Ring 5 (filled circles) and all 10 rings (triangles). The solid line through the measured points for Ring 5 is an empirical equation pertaining to the energy range shown. The stars show the resolutions after the uncertainty in the Doppler reconstruction has been included R_{dop} (Equation 3.9).

of more complicated shapes are taken into account, the energy dependence changes and the resolution worsens as is the case with the APEX array.

Energy resolutions for the measurements taken with the APEX NaI(Tl) array are shown in Figure 3.7. Resolutions R are shown for measurements including ring 5 only (center of the detectors), all 10 rings, and with the corrections due to uncertainties in the Doppler corrections (R_{dop}). The solid line is an empirical equation that is a close fit to the source resolutions for Ring 5 in the energy range 356-2614 keV:

$$R = \frac{1.368}{(E_\gamma - 268.76)^{0.355}}. \tag{3.7}$$

The necessary Doppler correction

$$E_{cm} = \gamma E_{lab}\,(1 - \beta \cos\theta_{lab})\,, \tag{3.8}$$

also contributes to the energy resolution through the spread in velocity of the pro-

Table 3.2: Expected energy resolutions of the APEX NaI(Tl) array. The values are determined through interpolation of the source measurements via empirical fits. The corrected energy resolution R_{dop} is determined from the values interpolated from measurements including all 10 rings at 90° and corrected for uncertainties due to $\beta = v/c$ R_β and the opening angle θ R_θ in the Doppler correction. The nuclei are grouped according to their cocktail beams and mid-target energies are listed. Unless otherwise noted, E_γ are the adopted values for the first excited state energy.

Nucleus	E_γ (MeV)	E_{beam} (MeV)	R (ring 5)	R (all rings)	R_β @ 90°	R_θ @ 90°	R_{dop} @ 90°
^{26}Mg	1.808	66.8	10.1%	10.6%	1.6%	6.0%	12.4%
^{32}Mg	0.885	71.9	14.0%	15.0%	1.7%	6.5%	16.4%
^{34}Mg	0.658 [a]	67.3	16.5%	18.0%	1.7%	6.3%	19.1%
^{35}Al	1.006 [b]	74.7	13.1%	14.0%	1.8%	6.6%	14.7%
^{36}Al	0.967 [c]	70.1	13.4%	14.3%	1.7%	6.4%	15.7%
^{37}Si	1.437 [b]	77.1	11.1%	11.2%	1.8%	6.7%	13.2%
^{48}Ca	3.832	51.0	7.5%	7.6%	1.4%	5.6%	9.7%
^{96}Mo	0.778	55.9	15%	16.1%	1.5%	5.8%	17.3%

[a] Ref. [38]. [b] Ref. [29]. [c] Present work.

jectile nuclei, and the uncertainty in the opening angle of the array. The corrected resolution becomes

$$(R_{dop})^2 = \left(\frac{\cos\theta_{lab}}{1-\beta\cos\theta_{lab}} - \beta\gamma^2\right)^2 \Delta\beta^2 + \left(\frac{\beta\sin\theta_{lab}}{1-\beta\cos\theta_{lab}}\right)^2 \Delta\theta^2 + (R)^2 . \quad (3.9)$$

As will be discussed in Section 4, the widths of the Doppler corrected energy peaks play a significant role in unfolding the ^{34}Mg spectrum. It is important to note that the energy range of interest for this experiment, including all Doppler shifts, is 487-2264 keV. The interpolated expected resolutions are shown in Table 3.2.

There were two previous reports on the APEX NaI(Tl) array [73, 74]. In the first, Kaloskamis *et al.* report an energy resolution R of 13% for the 1022 keV reconstructed

photopeak for annihilation photons and a position resolution between 3.0 and 3.6 cm. The second is a report by Perry *et al.* who measured an energy resolution R of 13% at 1332 keV and a position resolution of 3 cm. In the present work, the energy resolution R for all 10 rings at 1332 keV is expected to be 12% while at 1022 keV, the expected energy resolution R for all 10 rings is 13.9%.

3.1.4 Efficiency

Another crucial step in measuring the Coulomb excitation cross section is the estimation of the number of γ rays emitted from the Coulomb excitation reactions (Equation 3.1). In order to do this correctly, the overall photopeak efficiency of the γ-ray detectors must be understood. For this experiment, the number of γ rays detected is assumed to depend on the intrinsic efficiency of the APEX NaI(Tl) array, the angular distribution of the emitted γ rays, and the photoabsorption in the secondary target. The intrinsic efficiency was determined by comparing a GEANT [91] simulation of the array to the values obtained from several radioactive source measurements. Photoabsorption cross sections for the target material were taken from [92]. For the final determination of the number of emitted Coulomb de-excitation γ-rays, the angular distribution was calculated and folded with the probablity for absorption and the intrinsic detector efficiency using MATHEMATICA [93].

Efficiency by Rings

Gamma-rays produced by Coulomb excitation have a non-isotropic angular distribution [14, 66, 70–72, 82]. To account for this distribution, as well as crystal variations over the length of a single detector, the array was subdivided virtually into 10 rings transverse to the beam axis (Figure 3.8). First, each detector was divided into 10 transverse slices by placing software gates on the reconstructed position. Slice boundaries were common over all detectors with dead portions toward the ends of the crystals excluded through the position calibration. To constitute a ring ($\mathcal{R}_i$), each of

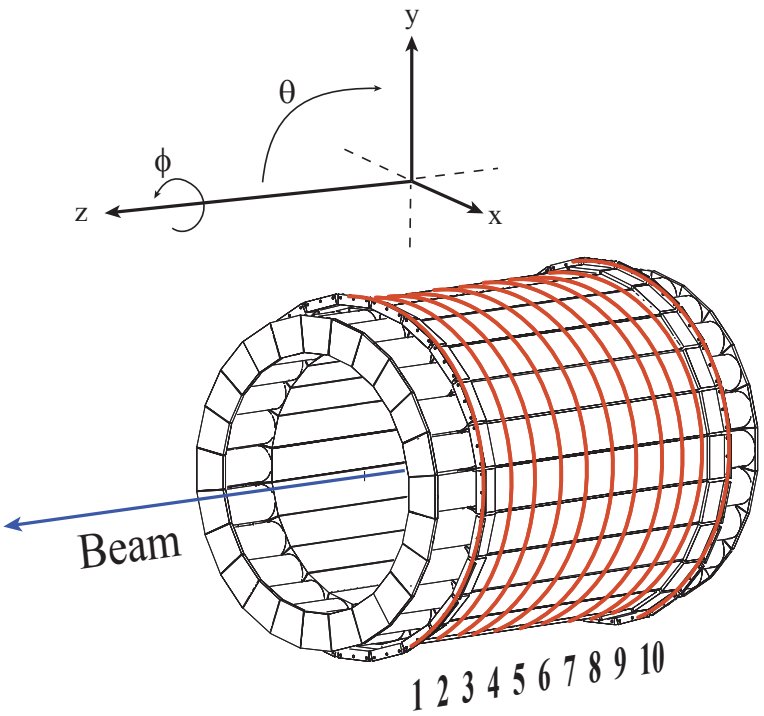

Figure 3.8: a) End view of the volumes defined in the GEANT simulation of the APEX NaI(Tl) array. b) Side View. The dashed line represents the z-axis, with the arrow indicating the positive direction.

the slice spectra ($\mathcal{S}_i$) were then summed over all 24 detectors,

$$\mathcal{R}_i = \sum_{j=1}^{24} (\mathcal{S}_i)_j. \tag{3.10}$$

In the laboratory (lab) frame, each virtual ring, $\mathcal{R}_i$ is spanned by the solid angle Ω_i^{lab} where Ω_i^{lab}=$\sin\theta_i^{lab} d\theta_i^{lab} d\phi_i^{lab}$. The discussion will assume that all angles are lab-frame angles unless otherwise noted, and the superscript lab will be dropped. All 10 rings have their symmetry axis along z, unique boundaries in θ, and a common range in ϕ from 0 to 2π. The intrinsic efficiency for $\mathcal{R}_i$ can be written:

$$\epsilon_{\Omega_i}^{\Omega_i} \equiv \frac{(number\,of\,\gamma\,rays\,detected\,in\,\Omega_i)}{(number\,of\,\gamma\,rays\,emitted\,into\,\Omega_i)}, \tag{3.11}$$

where the superscript denotes the element of solid angle over which γ-rays are detected, and the subscript indicates the element of solid angle over which γ-rays are

emitted. The sum of all 10 intrinsic ring efficiencies gives the total intrinsic efficiency ϵ_{intr}^{Tot} of the array:

$$\sum_{i=1}^{10} \epsilon_{\Omega_i}^{\Omega_i} = \epsilon_{intr}^{Tot}. \tag{3.12}$$

The number of γ rays emitted into Ω_i depends on the angular distribution of the de-excitation γ-rays, as well as the photon absorption cross section for the target material. The angular distribution is defined in the center-of-mass frame of the excited nucleus. For target nuclei this is the same as the laboratory frame, so $W_{lab}(\theta) = W(\theta_{cm})$ and $d\Omega_{lab} = d\Omega_{cm}$. Due to beam velocities of $\beta \approx 0.4c$ the relationship between $W_{lab}(\theta)$ and $W(\theta_{cm})$ for the projectile requires that θ_{cm} must be boosted according to,

$$\tan\theta_{cm} = \frac{\sin\theta_{lab}}{\gamma\left(\cos\theta_{lab} - \beta\right)}, \tag{3.13}$$

where β= (v/c) and

$$\gamma = \frac{1}{\sqrt{1-\beta^2}}. \tag{3.14}$$

Due to the change in variables, the differential solid angles must also be related by

$$d\Omega_{cm} = \frac{\left(\sin\theta_{cm}{}^2 + \gamma^2\left(\cos\theta_{cm} + \beta\right)^2\right)^{\frac{3}{2}}}{\gamma\left(1 + \beta\cos\theta_{cm}\right)}\, d\Omega_{lab}. \tag{3.15}$$

The derivation can be found in [70].

For the number of γ-rays emitted into Ω_i ($N_e^{\Omega_i}$) we have

$$N_e^{\Omega_i} = \left(\int_{\Omega_i} W_{lab}(\theta)\, \frac{\mathrm{d}\Omega_{\mathrm{cm,i}}}{\mathrm{d}\Omega_{\mathrm{i}}}\, \mathrm{d}\Omega_{\mathrm{i}} \int_{\Omega_i} \frac{I}{I_0}\, \mathrm{d}\Omega_i\right) N_e^{Tot} \tag{3.16}$$

where $\mathrm{W}_{lab}(\theta)$ is the angular distribution in the laboratory frame, I is the intensity of γ-rays half-way through the target, as described in Section 3.1.4, and I_0 is their initial intensity. Thus the number of γ-rays detected in the element of solid angle Ω_i

$(N_d^{\Omega_i})$ can be written:

$$N_d^{\Omega_i} = \left(\epsilon_{\Omega_i}^{\Omega_i}\right) \left(\int_{\Omega_i} W_{lab}(\theta) \, \frac{\mathrm{d}\Omega_{\mathrm{cm,i}}}{\mathrm{d}\Omega_{\mathrm{i}}} \, \mathrm{d}\Omega_{\mathrm{i}} \int_{\Omega_i} \frac{I}{I_0} \, \mathrm{d}\Omega_i \right) N_e^{Tot} \tag{3.17}$$

where

$$\int_0^{\pi} W_{lab}(\theta) \, \sin\theta \, \mathrm{d}\theta = 1. \tag{3.18}$$

Summing over all 10 rings, the total number of γ-rays detected is:

$$N_d^{Tot} = \left(\sum_{i=1}^{10} \left(\epsilon_{\Omega_i}^{\Omega_i}\right) \int_{\Omega_i} W_{lab}(\theta) \, \frac{\mathrm{d}\Omega_{\mathrm{cm,i}}}{\mathrm{d}\Omega_{\mathrm{i}}} \, \mathrm{d}\Omega_{\mathrm{i}} \int_{\Omega_i} \frac{I}{I_0} \, \mathrm{d}\Omega_i \right) N_e^{Tot}. \tag{3.19}$$

For an isotropic distribution, such as is emitted from a radioactive source, the number of γ-rays emitted into one element of solid angle Ω_i is a fraction $\Omega_i/4\pi$ of the number of γ rays emitted into 4π. The intrinsic ring efficiency becomes:

$$\epsilon_{\Omega_i}^{\Omega_i} = \frac{N_d^{\Omega_i}}{\left(\frac{\Omega_i}{4\pi}\right) N_e^{4\pi}} \tag{3.20}$$

$$= \left(\frac{4\pi}{\Omega_i}\right) \epsilon_{4\pi}^{\Omega_i}, \tag{3.21}$$

and enters the calculation of the final corrected efficiency at

$$E_{lab} = \frac{E_{cm}}{\gamma \left(1 - \beta \cos\theta_{lab}\right)}. \tag{3.22}$$

With this, the final expression for the total number of Coulomb de-excitation γ-rays detected by the Apex NaI(Tl) array is

$$N_d^{Tot} = \left(\sum_{i=1}^{10} \left(\frac{4\pi}{\Omega_i}\right) \epsilon_{4\pi}^{\Omega_i} \int_{\Omega_i} W_{lab}(\theta) \, \frac{\mathrm{d}\Omega_{\mathrm{cm,i}}}{\mathrm{d}\Omega_{\mathrm{i}}} \mathrm{d}\Omega_{\mathrm{i}} \int_{\Omega_i} \frac{I}{I_0} \, \mathrm{d}\Omega_i \right) N_e^{Tot}, \tag{3.23}$$

and denoting the quantity in the parenthesis by ϵ_{corr} the Coulomb excitation cross

section becomes

$$\sigma_{CE} = \frac{(N_d^{Tot})}{\epsilon_{corr}\, N_p\, N_t}. \tag{3.24}$$

Determining $\epsilon_{\Omega_i}^{4\pi}(E_\gamma)$

To determine the intrinsic efficiency of the array as a function of γ-ray energy, measurements were made with 5 calibrated radioactive sources and then compared to a GEANT simulation of the array. Placed at the target position, the sources ^{137}Cs, ^{203}Hg, ^{54}Mn, ^{223}Th, and ^{88}Y (see Table 3.1) were measured for 2-6 hours each. The detector multiplicity was restricted to 1, meaning that an event was counted if and only if no more than one detector triggered. This is the same constraint that was placed on the detectors for the analysis of the experiment data. After position and position-dependent energy calibrations were included (Section 3.1.1) by SpecTcl, these efficiency runs were sorted. For each of the 10 rings, SpecTcl output energy spectra in the gf2 format. GF2 was used to fit the spectra for each source and the efficiency was extracted from the peak areas as

$$\epsilon = \frac{N}{(br)\,(t)\,(A)}, \tag{3.25}$$

where N is the area under the photopeak, br is the branching ratio for that particular γ-ray, t is the duration of the measurement, and the A is the activity of the source at the time of the measurement. The activity is given by

$$A = A_0\, exp\left(\frac{-\ln 2}{t_{1/2}} \cdot t\right), \tag{3.26}$$

or,

$$A = A_0\ (1/2)^{t/t_{1/2}}, \tag{3.27}$$

where A_0 is the initial activity of the source, $t_{1/2}$ is the half-life, and t is the time elapsed since A_0 was determined.

The GEANT Simulation

GEANT 3.21 is a powerful detector simulation tool available from CERN [91]. It simulates the interaction of particles with all user-defined volumes and reports the energy deposited in any volume specified as active. Most known γ-ray interactions are included. For this experiment, the NaI(Tl) crystals were defined as the active volume [74], while the target, target frame, vacuum, beam pipe, air, quartz windows, and aluminum housing were included as inactive volumes (Figure 3.9). GEANT facilitates user-control of particle kinematics and also allows for simulation of data flow after the interaction has taken its course.

In order to simulate the efficiency, γ rays ranging from 0 to 5000 keV are emitted from the center of the array in a random fashion. One γ ray is fully processed before the next is triggered. The positions of the interactions in the crystal, and the energy deposits at those interaction points are recorded until none of the initial energy is left. For each of the 24 detectors, every energy deposit is converted into the light output expected to be seen by the photomultiplier tubes at each end of the detector [73]. These light outputs are incremented until there are no more energy deposits resulting from that event. The final position and energy of the initial γ ray are then reconstructed from these two quantities. Following the reconstruction, the histograms are filled. Thresholds are placed on the energy to simulate those on the CFDs and the shapers in the actual setup. The values for the thresholds are determined by direct comparison of the simulated raw energy with the actual raw energy for each photomultiplier tube. The virtual efficiency rings are also recreated at this stage in order to exclude the dead portions of the crystals.

The simulated widths of the PMT signals Y_u and Y_d are extracted from the measured width of the total reconstructed energy spectra (E). The reconstructed energy

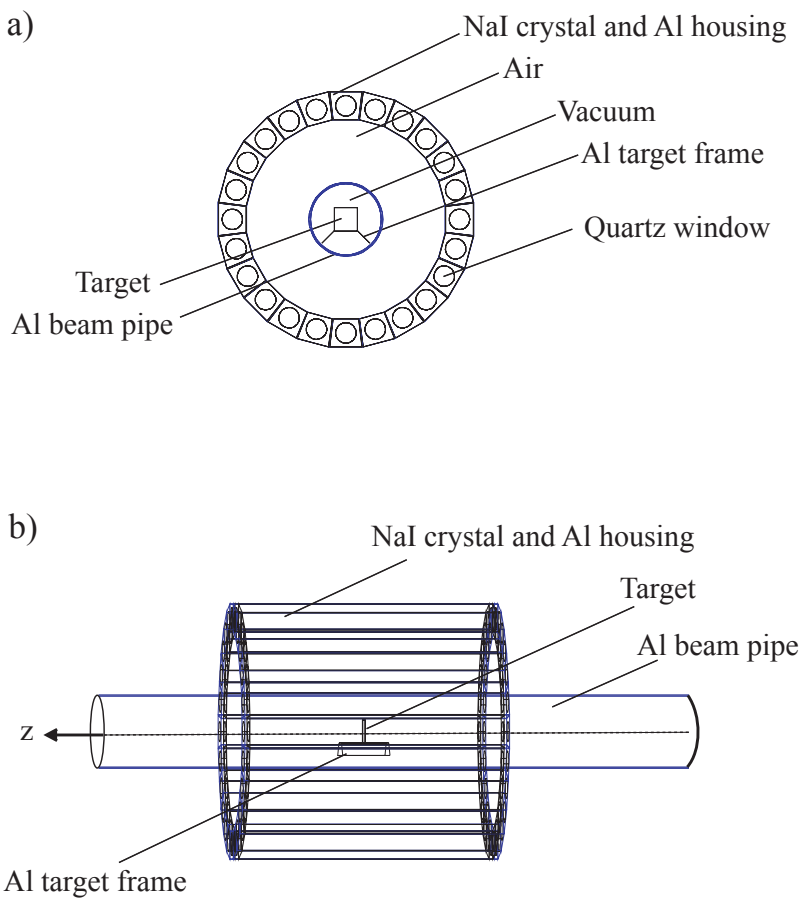

Figure 3.9: The geometry specified in the GEANT simulation of the APEX NaI(Tl) array.

is a combination of Gaussian distributions,

$$E = \sqrt{Y_u \cdot Y_d} \sim \left(exp\left(-\frac{Y_u^2}{\sigma_u^2} - \frac{Y_d^2}{\sigma_d^2} \right) \right)^{\frac{1}{2}}. \tag{3.28}$$

If the γ ray is deposited at the center of the array, the light attenuation in either direction can be assumed to be the same. If we assume both PMTs to be identical, the signals Y_d and Y_u,

$$Y_d = g\frac{E}{2}exp(-\mu(L/2 + X)), \tag{3.29}$$

and

$$Y_u = g\frac{E}{2}exp(-\mu(L/2 - X)), \tag{3.30}$$

where g is a simulated gain factor, μ= 0.047 is the attenuation coefficient obtained from [73], L is the length of the detector, and X is the position of interaction of the γ-ray, and their widths σ_u and σ_d are also equal. If this is true, $\sigma_u = \sigma_d = \sigma$, and we can extract the width σ from the total width of the reconstructed energy distribution σ_E. Combining the gaussians Y_u and Y_d leads to the relationship,

$$\sigma_E = \sqrt{\frac{\sigma^2}{2}}, \tag{3.31}$$

and the FWHM = 2.354σ [94].

The reconstructed energy source measurements for Ring 5 (center of the array) were fit and the energy dependence of this full reconstructed energy resolution is given in Equation 3.8. The form is an empirical function that fits the resolutions of the energy source measurements from 356 keV to 2614 keV and was discussed in Section 3.1.3.

For the final simulated resolution, each of the PMT signal widths were extracted individually using equation 3.31 and equation 3.8. The full detected energy was then reconstructed from these two PMT distributions.

In order to simulate the efficiency, only photopeak events with multiplicity one,

above lower and below upper energy thresholds , and within one of the 10 specified rings were binned. As in the actual data collection, the energies are binned by ring, and then the rings are summed for the total spectrum. This spectrum was then divided by the emitted energy spectrum to obtain the efficiency curve. Even with these constraints, there is a discrepancy between the GEANT prediction and the measured source points 662, 834, 898, 1836, 2614 keV. The discrepancy can be accounted for by considering the difference of backgrounds between the simulation and the measured values, and the exclusion of slices through the position calibration since the simulation was necessarily treated differently than the data in this regard. For example, the simulated efficiency (31.87%) for ^{137}Cs at 662 keV differs from the measured efficiency (22.2%) by 43%. When the measured and simulated peaks are fit with GF2, there is a 17% difference between the areas of the two. Another 22% is accounted for in the difference of excluded position slices between the simulation and the measurement.

For the final intrinsic efficiency, the values for the efficiency simulated by GEANT were scaled to fit the source data. A χ^2 analysis was performed to find a scaling factor of 0.813(24).

For the final analysis, the scaled simulated efficiency was used in the extraction of the Coulomb excitation cross section. It is compared to measured values in Figure 3.10. The discrepancy between the 356 keV measured point and the simulation is beyond the lower limit of the energy range for this experiment, 487-2264 keV. The disagreement is due to the difference between the simulated thresholds and actual thresholds. Figure 3.11 shows that varying the thresholds in the simulation does not affect the shape of the efficiency curve for the range of energy of interest to this work.

Angular Distribution

Coulomb excitation produces a non-isotropic distribution of de-excitation γ-rays. This is well-understood and has been applied and discussed in several cases [69–71,82]. The

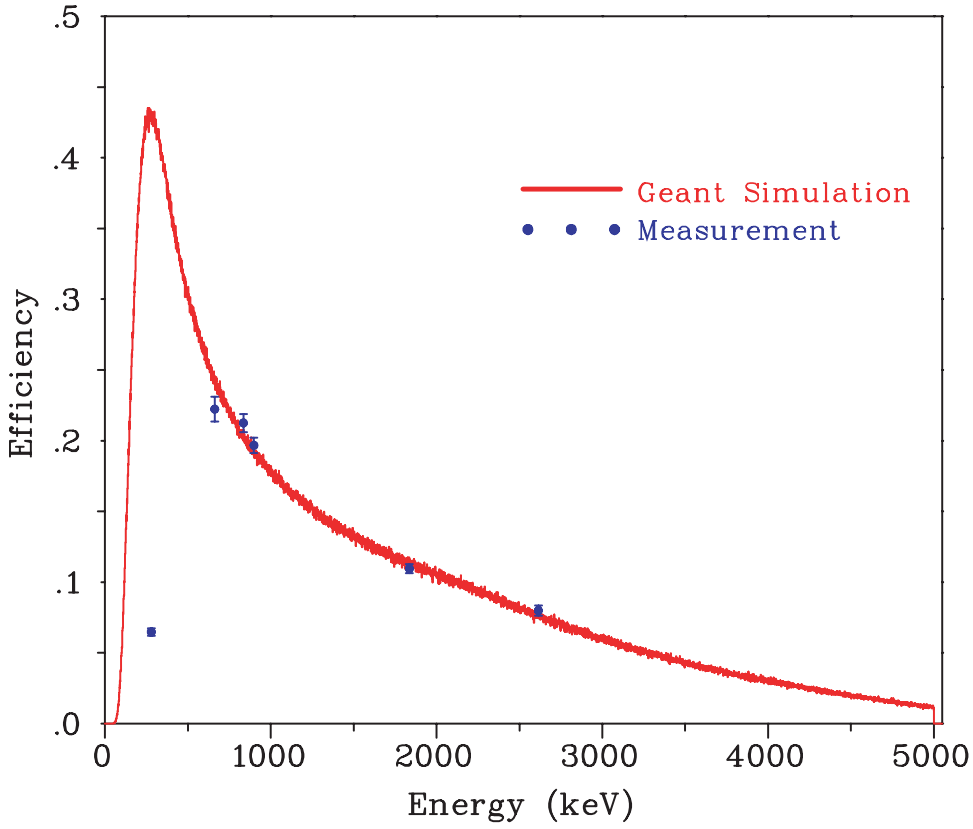

Figure 3.10: The scaled, simulated efficiency curve compared to the measured values. This is the intrinsic efficiency which is later folded with the angular distribution and photon absorption to obtain the final value for the efficiency. Thresholds in this simulation are matched to actual experiment threshold values.

full derivation can be found in [66, 72]. The application in this case follows [27, 70] and only the final expressions will be stated here for continuity. Since the APEX NaI(Tl) detectors are arranged symmetrically around z, we integrate over ϕ and from the minimum impact parameter b_{min} to ∞, and the angular distribution is expressed as a function of θ_{cm}:

$$W(\theta_{cm}) = \sum_{\substack{k\,even,\,\mu \\ L,\,L'}} \left| G_{\lambda\mu}\left(\frac{c}{v}\right)\right|^2 g_\mu(\xi)(-)^\mu \begin{pmatrix} \lambda & \lambda & k \\ \mu & -\mu & 0 \end{pmatrix} \times \begin{Bmatrix} I_f & I_f & k \\ \lambda & \lambda & I_i \end{Bmatrix} F_k(L, L', I_{ff}, I_f)\sqrt{2k+1}\, P_k(\cos(\theta_{cm}))\,\delta_L\,\delta_{L'}. \tag{3.32}$$

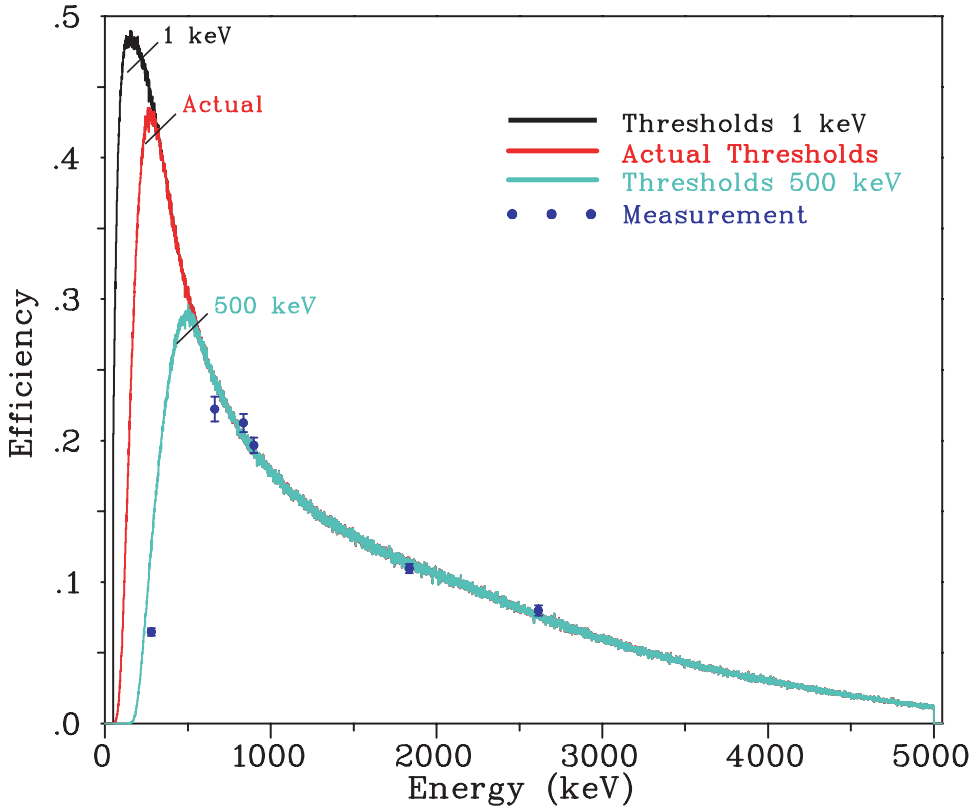

Figure 3.11: The shape of the efficiency curve does not vary with changes in the simulated thresholds for the energy range 487-2264 keV.

where $g_\mu(\xi)$ are the Winther and Alder functions (Equation 2.7), $G_{\lambda\mu}\,(c/v)$ are given in equations 2.9 and 2.9, F_k (Equation 2.15) expresses $\gamma-\gamma$ correlations, the $\mathrm{P}_k\,(\cos\,(\theta_{cm}))$ are the usual Legendre polynomials, and the $\delta_L\,\delta_{L'}$ are Kronecker Delta functions. This is usually expressed:

$$W(\theta_{cm}) = \sum_{k\,even} a_k P_k\,(\cos\,(\theta_{cm})). \tag{3.33}$$

The angular distributions for ^{26}Mg, ^{32}Mg, and ^{34}Mg are shown in Figure 3.12 along with the corresponding b_{min} and β. The bottom panel shows the m-state distributions as calculated by [95]. The middle panel shows the distinction between the laboratory frame and the center-of-mass frames, and the top panel shows the difference between a boosted isotropic distribution and that of the true $W(\theta)$ of the projectile, in the laboratory frame. The range of effective detector coverage in θ_{lab} is indicated in both Figures. The a_k calculation was taken from [27, 70]. For all three of these examples,

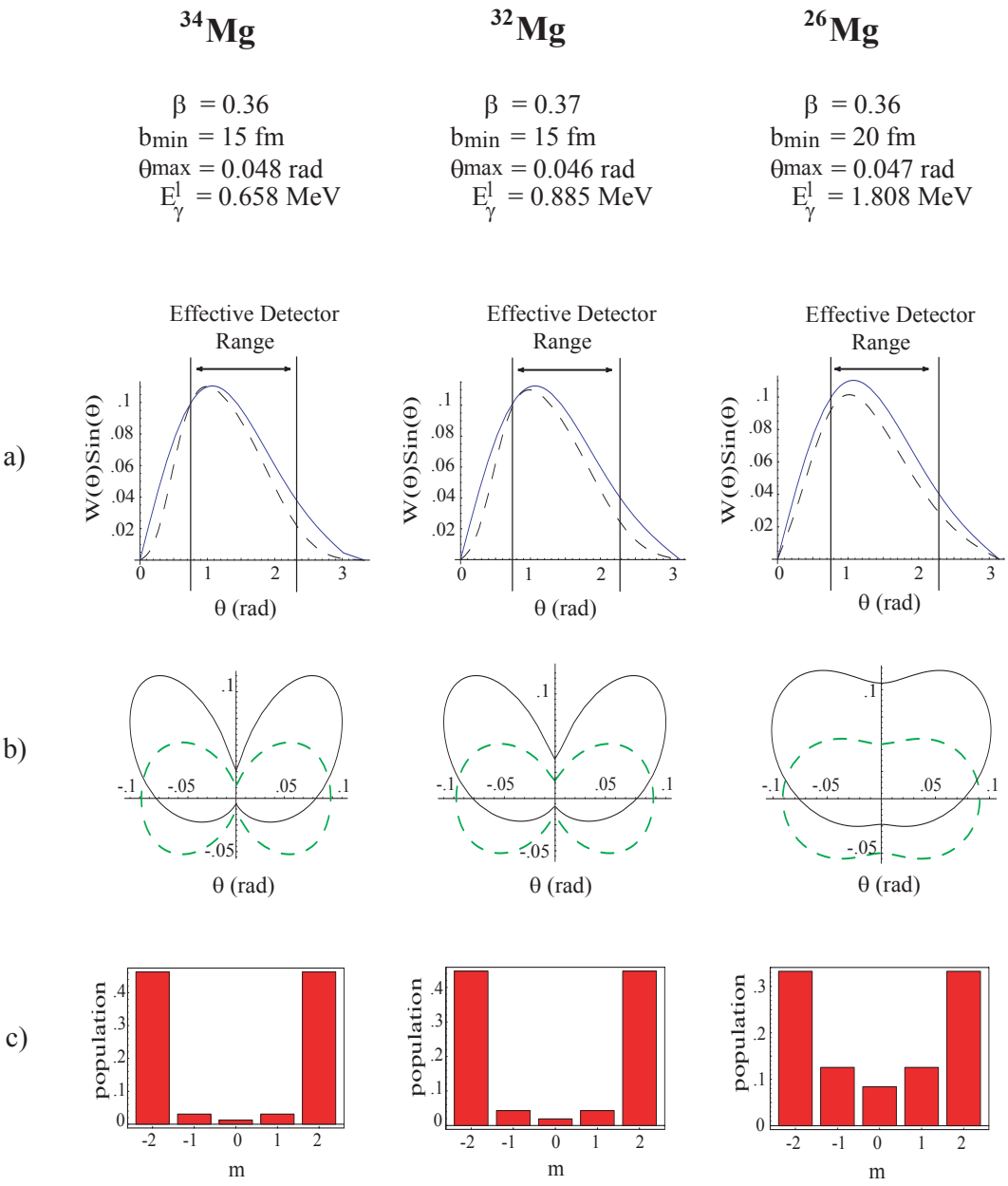

Figure 3.12: The Coulomb excitation angular distributions are presented for ^{26}Mg, ^{32}Mg, and ^{34}Mg at the listed velocity, β, and minimum impact parameter, b_{min}. a) The importance of including the angular distribution as a correction, where the dashed line indicates $W(\theta)$ and the solid line is the boosted isotropic distribution. The effective detector range after exclusion of the ends of the detectors is indicated. b) Parametric plots highlighting the difference between the center-of-mass indicated by the dashed line, and the boosted, indicated by the solid line, frames. c) The population of the m-states as determined by [95].

it can be seen that the distribution is close to that expected for an $l = 2$, $m = \pm 2$ state.

Photon absorption in the target

As lifetimes for excited states considered here are on the order of picoseconds [17], it is likely that the Coulomb de-excitation γ-rays will be emitted somewhere inside the target material. Interactions of photons with the target material through the photoelectric effect, Compton scattering, and pair production reduce the fraction of photons that leave the target, but do not decrease their energy. As was shown in [82], these interactions are a significant factor in the estimate of the final number of γ-rays detected in a Coulomb excitation experiment. Here, the probability for a single photon to survive the target thickness is folded with the angular distribution and the measured efficiency for each ring in the determination of the final number of γ rays detected by the APEX array.

For a beam of parallel photons, the intensity loss after passing through a material of thickness d is exponential:

$$I_{abs} = I_0 2^{\frac{-d}{d_{1/2}}}, \tag{3.34}$$

where I_0 is the initial intensity of the beam, and $d_{1/2}$ is the half-thickness of the material [96]. The half-thickness is the thickness of material through which half the intensity of the photon beam is lost:

$$d_{1/2} = \frac{A \log 2}{N_A \rho \sigma (E_\gamma)}, \tag{3.35}$$

where A is the mass number and ρ is the density of the absorbing material, N_A is Avogadro's number, E_γ is the γ-ray energy and σ is the photon absorption cross section (b/atom):

$$\sigma = \phi_{photo} + Z\sigma_c + \tau_{pair}, \tag{3.36}$$

which depends on the photoelectric effect (ϕ_{photo}), Compton scattering (σ_c), and pair production (τ_{pair}) cross sections. As there are Z electrons per atom, the Compton scattering cross section is multiplied by Z [81, 97].

In terms of the virtual rings and the solid angle Ω_i for the APEX NaI(Tl) array, the probability that the photon exits the material in that solid angle becomes:

$$\begin{aligned} Pr &= \int_{\Omega_i} \frac{I_{abs}}{I_0}\, \mathrm{d}\Omega_i \\ &= \int_{\Omega_i} 2^{\frac{-d}{d_{1/2}}}\, \mathrm{d}\Omega_i. \end{aligned} \tag{3.37}$$

Photon absorption cross section values taken from [92] have been fitted for both the ^{197}Au and ^{209}Bi targets in Figure 3.13 with the second order exponential [82, 92]:

$$\sigma(E_\gamma) = A + B\, exp\left(\frac{-E_\gamma}{C}\right) + D\, exp\left(\frac{-E_\gamma}{F}\right). \tag{3.38}$$

where A, B, C, D, and F are fit parameters and E_γ is the energy of the γ ray. The coefficients are shown in Table 3.3.

Values taken from the fits were folded with the intrinsic efficiency and the angular distribution to determine the final number of detected γ rays.

The Final Efficiency Estimation

The final efficiency at each γ-ray energy of interest is folded together using MATHEMATICA. For each ring$_i$, $W(\theta)$ (Equation 3.33) is calculated and integrated over Ω_i.

Target	A	B	C	D	F
^{197}Au	7.7424	87.515	324.59	1958.4	75.364
^{209}Bi	8.4175	104.76	325.66	2111.0	76.724

Table 3.3: Photoabsorption cross section fit parameters.

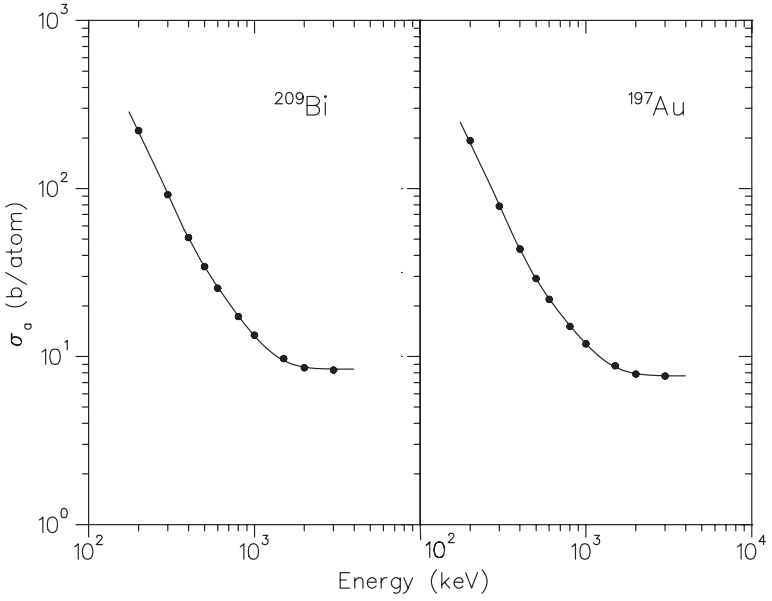

Figure 3.13: Photon absorption cross sections σ_a for the gold and bismuth secondary targets.

It is then folded with the photon absorption probability (Equation 3.37) and finally with the intrinsic efficiency for that ring and when combined with the number of γ rays detected, give the number of emitted de-excitation γ-rays:

$$N_d^{Tot} = \left(\sum_{i=1}^{10} \left(\epsilon_{\Omega_i}^{\Omega_i} \right) \int_{\Omega_i} W(\theta) \frac{\mathrm{d}\Omega_{\mathrm{cm,i}}}{\mathrm{d}\Omega_{\mathrm{i}}} \mathrm{d}\Omega_{\mathrm{i}} \int_{\Omega_i} \frac{I_{abs}}{I_0} \mathrm{d}\Omega_i \right) N_e^{Tot}. \tag{3.39}$$

Table 3.4 lists the efficiencies for the range of energies pertinent to this study.

3.2 Gamma-ray and Particle Sorting

Once the calibrations, energy resolutions and efficiencies are understood, the actual experiment data can be processed to obtain the number of detected de-excitation γ-rays and the number of projectile nuclei. Using the histogrammer SpecTcl, several contours are placed on the data and used as software gates in order to distinguish between the particle-γ coincidences for different isotopes in the cocktail beam. Energies, emission angles, and counts of de-excitation γ-rays are recorded in addition to the numbers of identified projectile nuclei.

Table 3.4: The efficiencies for the APEX NaI(Tl) array are listed. The $\epsilon(E_{lab})$ values are raw efficiencies for Doppler corrected energies integrated over the Ω_i for each Ring$_i$. Corrections are made for W(θ) and photon absorption in the target. The sums over all 10 rings are performed for the listed values. The values used in the analysis are listed in the right-most column. The E_{cm} (E_γ) are taken from the sources listed in Table 3.2. E2 transitions are assumed, and the γ-ray energies for ^{34}Mg, ^{35,36}Al and ^{37}Si were measured in the present work.

Isotope	E$_{cm}$ (keV)	E$_{lab}$ (keV)	$\sum_{i=1}^{10}\left(\frac{4\pi}{\Omega_i}\right)\epsilon_{4\pi}^{\Omega_i}(E_{lab})$	Corrected $\epsilon\,(E_{lab})$	
				W(θ) only	W(θ) and I$_{abs}$
^{26}Mg	1808	1344-2264	12.2%	11.6%	10.7%
^{32}Mg	885	650-1115	20.47%	20.45%	17.9%
^{34}Mg	659	487-822	25.5%	26.2%	21.8%
^{35}Al	985	734-1272	18.9%	17.7%	14.7%
^{36}Al	967	713-1216	19.2%	18.0%	15.1%
^{37}Si	1437	1043-1822	14.3%	13.3%	11.1%
^{96}Mo	778	589-964	22.1%	22.3%	21.4%

3.2.1 Projectile Nuclei

The particle identification is achieved by placing contours on the energy loss (ΔE) versus time-of-flight spectrum built from the zero degree detector (Section 2.2.3) fast plastic signal and the cyclotron radio frequency (rf). Four sets of these particle software gates were required over the entire ^{34}Mg,^{35,36} Al,^{37} Si run to account for small shifts in the time-of-flight. For the remainder of the runs ^{96}Mo,^{26} Mg, and ^{48}Ca, only one set was necessary. Each set consists of one contour per isotope per rf pulse. Figure 3.14 shows one set of the particle gates for the ^{34}Mg beam. The radio frequency was 21 MHz corresponding to 47.5 ns between pulses.

The particle contours are used as a condition for binning the γ rays. A de-excitation γ-ray is binned as originating from a particular nucleus only if it is detected in coincidence with a projectile nucleus that falls into that particular particle's software gate. When the data is completely scanned, integrating the ΔE/time-of-flight spectrum also gives the number of incoming projectile nuclei per particle gate (N_p)

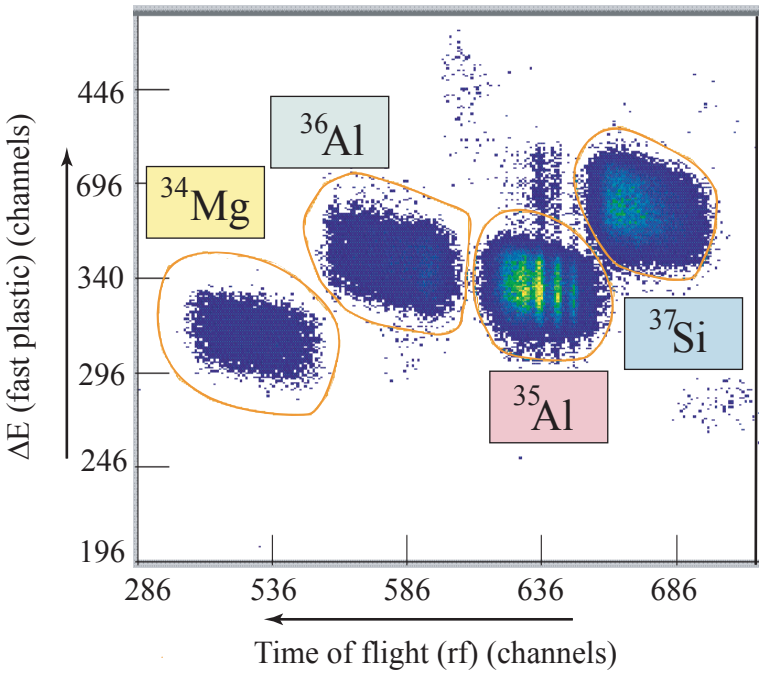

Figure 3.14: Contours on the ΔE vs. time-of-flight spectrum serve as software gates identifying the isotope species. The ^{34}Mg cocktail is shown here.

divided by the zero degree detector's down-scale factor, as listed in Table 2.2.

3.2.2 Time Cuts

Accidental coincidences with γ rays originating from the zero degree detector's plastic can also be excluded through software gating. They can be excluded from the γ-ray energy spectra by making cuts on the time spectra. This is illustrated in Figure 3.15 which depicts the following example and shows the time spectrum and effects of the time cuts on the energy spectra. In the case of ^{26}Mg, the distance from the target to the array is 25 cm, from the target to the zero degree detector 122 cm, and from the zero degree detector to the center of the array is 124 cm. The speed of the projectiles after the target is 0.3c. Assuming the γ rays to be traveling at the speed of light, we can deduce from these values that γ rays originating from the zero degree detector should be detected 15 ns after those originating at the secondary target position. The delay is evident in the time spectra in which the TDC stop is binned. The 15 ns delay is resolvable in this spectrum and so cuts may be placed on the γ rays originating at

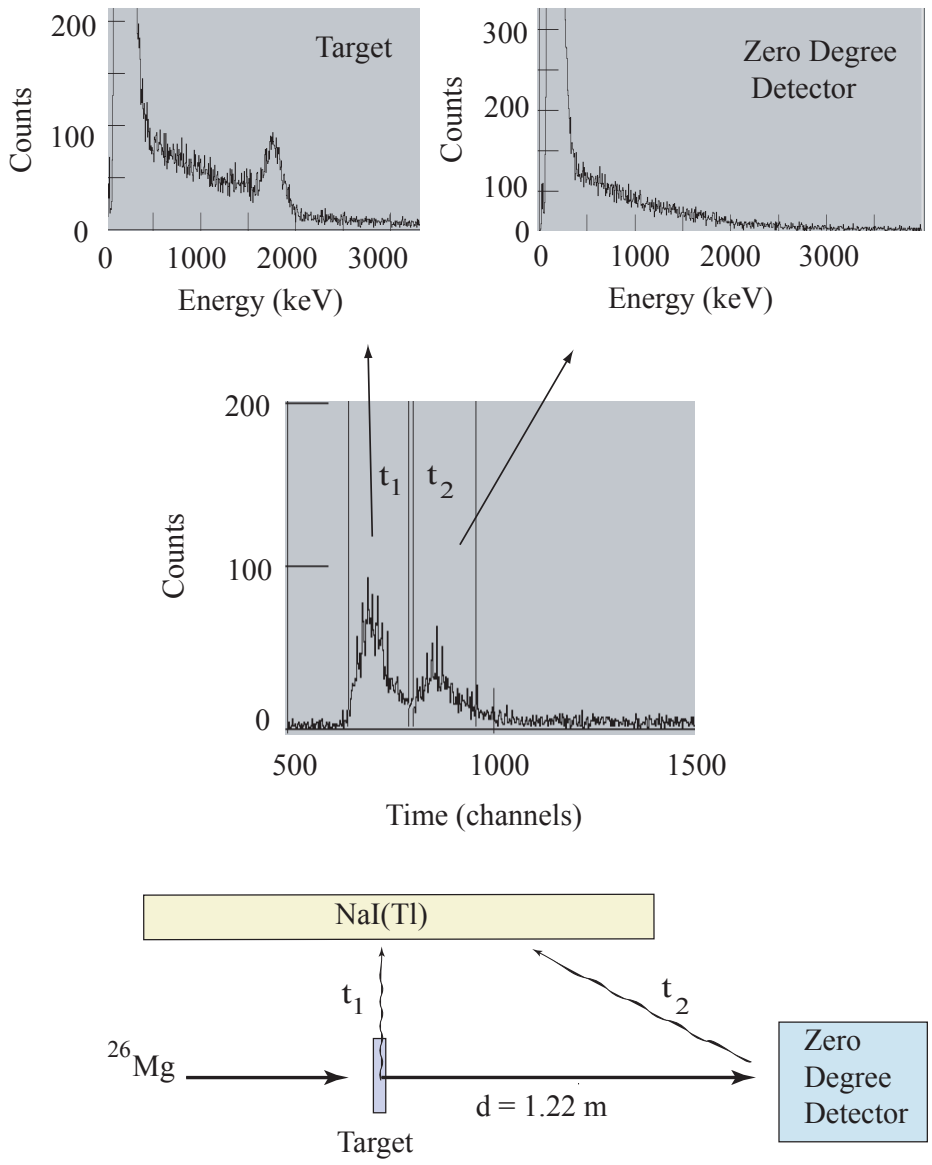

Figure 3.15: The time cuts for ^{26}Mg are shown. The top panels show the effects of the time cut on the Doppler-corrected energy spectra. On the left is the spectrum resulting from the cut made on γ rays originating at the target position. On the right are the γ rays originating at the zero degree detector. The time spectrum is shown in the middle panel with 10 channels per nanosecond (1 ns/10 ch). The origination of the γ rays is depicted in the drawing at the bottom.

^{26}Mg				TOTAL
E_γ	Fit	Systematic		
	<2%	<0.5%		$< \pm 2.1\%$
σ_{CE}	N_γ	$\epsilon_{intrinsic}$	ϵ_{corr}	
	2.8%	2.9%	1%	$\pm 4.8\%$
B(E2)	σ_{CE}	$\theta_{max} \pm 0.1^\circ$		
	4.8%	7.3%		$\pm 8.8\%$

Table 3.5: Uncertainties in γ-ray energy, E_γ, Coulomb excitation cross section, σ_{CE}, and the reduced quadrupole transition probability $B(E2)$ value for ^{26}Mg.

the target and applied to the rest of the γ-ray spectra.

3.3 Error Analysis

Uncertainties in the measurements and extracted $B(E2)$ values are listed in Table 3.5. The largest contributions to the error were the statistical uncertainties associated with peak fitting. Systematic errors resulted from target placement ($\pm$5mm) and the efficiency estimation.

The statistical uncertainty in E_γ was primarily due to the large intrinsic resolution (Section 3.1.3) of the APEX NaI(Tl) array. Contributions via Doppler broadening by the beam spread and uncertainty in the energy loss in the target are insignificant when compared to the energy resolution. The statistical error is then fully determined by the peak fit. Systematic errors arise from the energy calibration which contributes less than 2%, and the placement of the target with a contribution less than 0.5%.

The uncertainty in the Coulomb excitation cross section results from counting the number of detected γ rays N_γ, the intrinsic efficiency estimation, and the corrections to the efficiency by photoabsorption in the target and the angular distribution. For N_γ, the entire uncertainty comes from counting statistics as determined using the fitting program GF2.

Uncertainty in the intrinsic efficiency has a combination of contributions. This

includes the uncertainties in the half-life $t_{1/2}$, initial activity, A_0, and the peak fits, which were folded together through error propagation [94]. The final uncertainty in the intrinsic efficiency is 2.9%.

The corrections to the intrinsic efficiency due to photoabsorption in the target and the angular distribution, $W(\theta)$, were on the order of 10%. Uncertainties on these 10% corrections were 10% for the absorption cross sections and negligible for $W(\theta)$. An uncertainty of 10% on a 10% correction results in a 1% contribution to the overall uncertainty in the efficiency.

Together, for the example of ^{26}Mg in Table 3.5, the uncertainty in the Coulomb excitation cross section is 4.8% after the error propagation. Uncertainties in the number of target nuclei, N_t, and the number of projectile nuclei, N_p, are small compared to those of the cross section and the efficiency, and may be omitted.

For the $B(E2)$ value, errors arise from the cross section, and the constant of proportionality (equation 2.10) which depends heavily on the maximum scattering angle. θ_{max} was taken to vary by $\pm 0.1^\circ$ and when combined with the uncertainties in the cross section, σ_{CE}, the total uncertainty in the B(E2) value for ^{26}Mg is 8.75%. The analysis of the uncertainties in the other nuclei follow the same treatment, but will not be shown.

The values for the first excited-state energy, Coulomb excitation cross section and $B(E2\uparrow)$ were obtained with the method outlined here, and will be presented in the next chapter.

Chapter 4

Observations

Observed Coulomb excitation cross sections, and excited state energies were measured and $B(E2\uparrow)$ values were extracted from the experimental data with the general analysis methods outlined in Chapter 3. In total, nine nuclei were analyzed: the secondary fragments ^{26}Mg, ^{32}Mg, ^{34}Mg, ^{35,36}Al, and ^{37}Si, two degraded primary beams ^{96}Mo, and ^{48}Ca, and the target nucleus ^{197}Au. The well-known nuclei ^{96}Mo, ^{26}Mg, and ^{197}Au were used as test cases. Beam production and parameters can be found in Table 2.1, and reaction specifics in Table 4.1 and Table 4.3.

4.1 Degraded ^{96}Mo

Prior to the main experiment, the $B(E2; 0^+_{g.s} \rightarrow 2^+_1)$ and $E(2^+_1)$ values of a degraded ^{96}Mo primary beam were measured via Coulomb excitation with a 0.184 g/cm^2 ^{197}Au target as a first test. ^{96}Mo is an even-even $Z = 42$, $N = 54$, stable nucleus with a relatively low first-excited state energy and high $B(E2\uparrow)$ value. The adopted values for E(2^+_1) and the $B(E2; 0^+_{g.s.} \rightarrow 2^+_1)$ are 778.245(12) keV and 2711(50) e^{2}fm^4 respectively [17]. The nucleus was measured several times via Coulomb excitation [98–101] in which ^{96}Mo participated in the reaction as a target nucleus, rather than the projectile as is the case here.

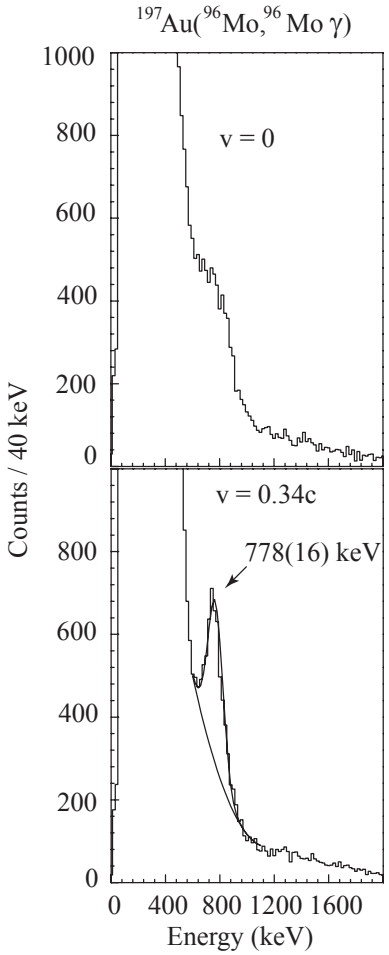

Figure 4.1: Gamma-rays in coincidence with degraded ^{96}Mo nuclei. Energies without Doppler reconstruction are displayed in the top panel while those following Doppler reconstruction in the projectile frame are displayed at the bottom. The mid-target velocity is listed and is assumed to be the velocity at the time of γ-ray emission. Gamma-rays originating from the ^{197}Au target are expected at 547 keV in the upper panel but are not distinguishable from the low energy background.

Coulomb de-excitation γ-ray energy spectra for each of the positions in the APEX array were obtained by the methods outlined in Chapter 3. The spectra for each of the slices not excluded by the position calibration were then summed over all 24 detectors to create the final total energy spectrum. Both the projectile-frame ($v = 0.34c$) and laboratory-frame ($v = 0$) spectra are shown in Figure 4.1. The photopeak at 778(16) keV was fit on top of a continuous quadratic background of the form $N = 200 - 15.8x + 0.5496$ where N is the number of counts in channel x. The fit yields 3273(134) counts in the photopeak corresponding to a Coulomb excitation

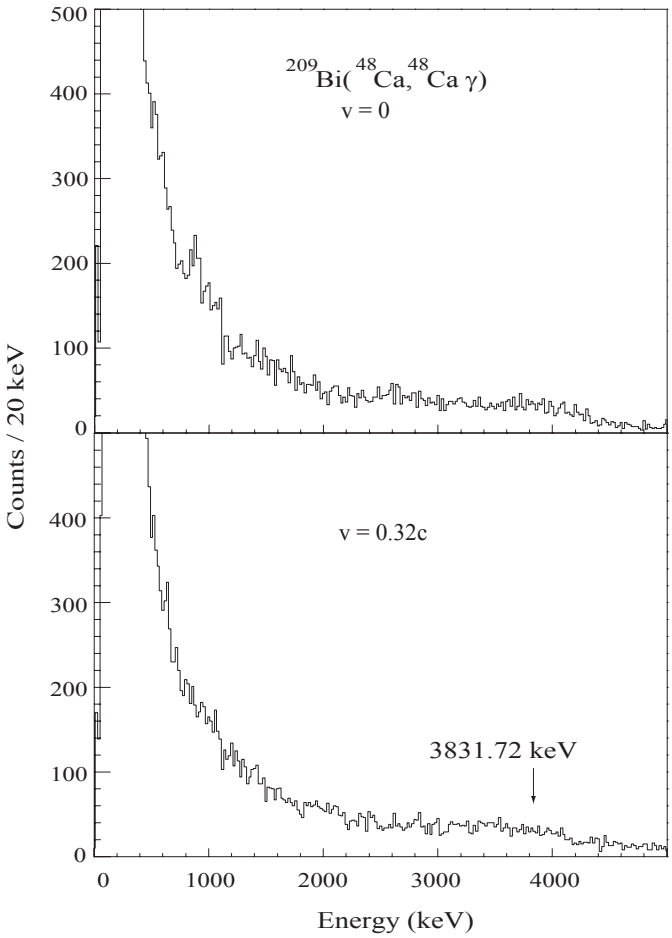

Figure 4.2: Gamma-rays in coincidence with ^{48}Ca nuclei after the reaction ^{209}Bi(^{48}Ca,^{48}Ca γ). The arrow marks the location of the expected 3831.72 keV peak.

cross section of 182(11)mb, and a $B(E2; 0^+_{g.s} \rightarrow 2^+_1)$ value of 2640(260) e^{2}fm^4. Both first excited state energy and reduced transition probability values agree with the adopted E(2^+_1) value of 778.245(12) keV and the $B(E2; 0^+_{g.s.} \rightarrow 2^+_1)$ value of 2711(50) e^{2}fm^4 [17].

4.2 The ^{48}Ca Primary Beam

All secondary beams were produced by fragmentation of the ^{48}Ca primary beam. In addition, the ^{48}Ca itself was degraded and directed to the N3 vault for Coulomb excitation with the 0.980 g/cm^2 ^{209}Bi target also used with the ^{26}Mg, and ^{34}Mg beams.

^{48}Ca is a stable, even-even nucleus with 20 protons and 28 neutrons. ^{48}Ca has a

high E(2_1^+) of 3831.72 keV [17], and the known $B(E2; 0^+_{g.s.} \rightarrow 2^+_1)$ value of 95(32) e^2fm^4 [17] yields a Coulomb excitation cross section of only 10.4 mb for this setup. This corresponds to 114 expected counts in the photopeak with an expected width of 410 keV (FWHM) for the total 1.3×10^8 incoming projectile ^{48}Ca nuclei. The energy spectra of the γ-rays detected in coincidence with the ^{48}Ca are shown in Figure 4.2. The spectrum is the sum of the energy spectra of all 24 detectors after particle and time and position gates are applied. For the projectile-frame spectrum, the energies are Doppler shifted into the projectile frame on an event-by-event basis.

The goal of the analysis of the ^{48}Ca energy spectrum is to obtain a background spectrum. In order to estimate the contributions to the overall spectrum by the ^{48}Ca de-excitation γ-rays, the interaction of the known 3831.72 keV γ-ray corresponding to the $0 \rightarrow 2^+$ transition was simulated using GEANT. The contribution to the energy spectrum by γ rays originating in ^{48}Ca over the energy range covering the lowest and highest energy Doppler shift in the whole experiment, 487-2264 keV, which is the range of interest for the experiment, was estimated by integrating the simulated spectrum in that energy range and comparing it to the integral of the photopeak. For 10,000,000 simulated counts overall, there were 4.0×10^5 counts in the photopeak and 6.7×10^5 counts in the energy range of 487-2264 keV. From the adopted B(E2) value of 95 e^2fm^4, 114 counts are expected for the photopeak in the experiment. Scaling the simulated spectrum to this expected number, 2.1 counts per 20 keV from the first 2^+ de-excitation γ-rays are expected in the experimental data for Figure 4.2 in the energy range 487-2264 keV. The range is below the single-escape, double-escape and photopeaks and so the contributions can be mainly attributed to Compton scattering, the target de-excitation and accidental background radiation. The random background has not been subtracted from the spectrum, and we use this spectrum as part of the background that will be scaled to each experiment.

There is a small cross section of 0.617 mb for the Coulomb excitation of ^{209}Bi in this reaction with ^{48}Ca as well (Section 2.2.2), and γ-rays originating there make

a similarly small contribution to the overall spectrum. For the ^{48}Ca experiment we expect 33.9 detected de-excitation γ-rays originating from the ^{209}Bi target spread from 700 to 1235 keV in the projectile-frame spectrum.

Because both the ^{48}Ca and the target ^{209}Bi make only small contributions to the full ^{48}Ca energy spectrum in the energy range of 487-2264 keV, the majority of the γ-rays in that range for the ^{48}Ca spectrum are described as room and beam-related background counts. A fit energy spectrum of ^{209}Bi(^{48}Ca,^{48} Ca γ) over 600-2400 keV is therefore used in determining the shape of the background for the other nuclei in the experiment. The form of the fit is $N = 51.73 - 1.035x + 0.0207x^2$ where N is the number of counts in channel x. For each of the other nuclei in the experiment, this background form needs to be scaled by the number of target nuclei times the number of incoming beam particles $N_t N_p$.

Below 600 keV, the energy spectra show a dependence on A and Z which cannot be extracted consistently from the data available here. The dependence is shown in Figure 4.3 which shows the low-energy γ-ray spectra of ^{197}Au(^{96}Mo,^{96} Mo γ), ^{209}Bi(^{48}Ca,^{48} Ca γ), and ^{209}Bi(^{26}Mg,^{26} Mg γ) after normalization to the target and projectile nuclei, N_t and N_p. In order to understand the shape of the low energy background for $Z = 12$, the ^{48}Ca fit was scaled by the quantity $N_t N_p$ to the ^{26}Mg spectrum. This scaled fit, $N = 100 - 2x + 0.04x^2$ where N is the number of counts in channel x, describes the shape of the ^{26}Mg spectrum in the low-energy range, and was used as the background shape after scaling by the number of target and projectile nuclei, N_t and N_p, for the Mg, Al, and Si isotopes.

4.3 The Test Case ^{26}Mg

Coulomb excitation of the stable nucleus ^{26}Mg on a 0.980 g/cm^2 ^{209}Bi target provided a test of the experimental apparatus and data analysis method. Gamma-ray energies and $B(E2; 0^+_{g.s.} \rightarrow 2^+_1)$ values were checked against the adopted [17] $E(2^+_1)$ value

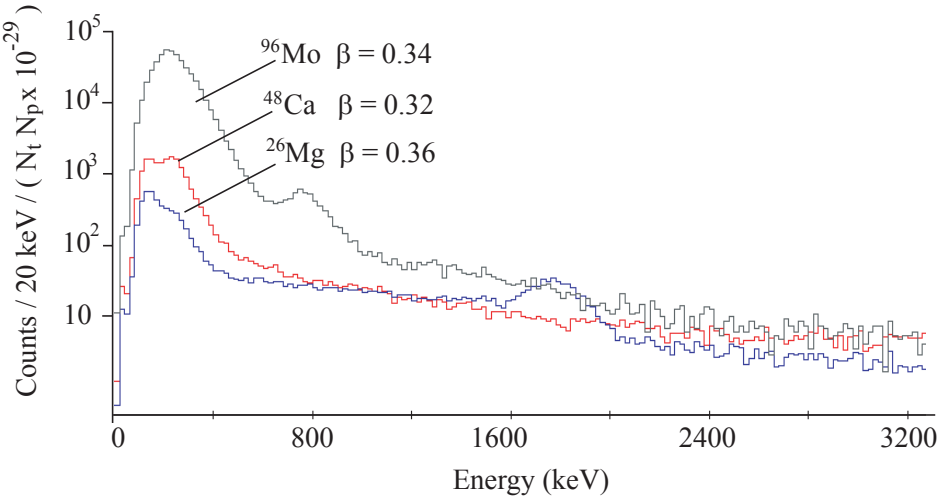

Figure 4.3: Energy spectra for ^{197}Au(^{96}Mo,^{96}Mo$\,\gamma$) at 55.9 MeV/nucleon, ^{209}Bi(^{48}Ca,^{48}Ca$\,\gamma$) at 51.0 MeV/nucleon, and ^{209}Bi(^{26}Mg,^{26}Mg$\,\gamma$) at 66.8 MeV/nucleon are shown on a log scale normalized by the number of target and projectile nuclei, N_t, N_p. The plot shows the low-energy background for nuclei of different A and Z. Mid-target velocities are listed for each nucleus.

of 1808.73(3) and $B(E2; 0^+_{g.s.} \rightarrow 2^+_1)$ value of 305(13) e^{2}fm^4 for ^{26}Mg. In addition, the energy resolution of the ^{26}Mg peak was used to incorporate in-beam data and the uncertainty in the Doppler reconstuction into the characterization of the energy resolution of the APEX NaI(Tl) array as discussed in Section 3.1.3.

Gamma rays in coincidence with the stable nucleus ^{26}Mg are shown in Figure 4.4. The background was not subtracted, instead, the parametrization of the ^{48}Ca background was used to fit the spectrum in addition to a Gaussian for the photopeak. The ^{48}Ca background was scaled by the number of target and incoming projectile nuclei N_tN_p from the ^{48}Ca fit described in Section 4.2 by a factor of 2.1. This resulted in a quadratic background $N = 100 - 2x + .04x^2$ for the ^{26}Mg energy spectra, where N is the number of counts in channel x.

In the ^{26}Mg projectile-frame spectrum there are 3376(116) counts on top of the background in the 1808(38) keV photopeak for ^{26}Mg corresponding to a Coulomb excitation cross section of 44.4(19) mb, a $B(E2; 0^+_{g.s.} \rightarrow 2^+_1)$ value of 315(28) e^{2}fm^4 and the deformation parameter $|\beta_2|$ value of 0.49(2). Both energy and reduced transition matrix element values are in agreement with the adopted [17] $E(2^+_1)$ value of

1808.73(3) and $B(E2; 0^+_{g.s.} \rightarrow 2^+_1)$ value of 305(13) e^2fm^4.

Two peaks of unknown origin are visible in the spectrum corresponding to energies in the laboratory frame. One peak is seen at 926 keV, corresponding to counts from the $9/2^- \rightarrow 7/2^-$ 896.28(6) keV transition in ^{209}Bi plus additional background contribution. Additional γ-ray flux of unknown origin apparently at rest is observed at 528(6) keV. In addition to these are the ^{26}Mg de-excitation photons which are spread over a range of 1340-2264 keV, and the ^{26}Mg Compton continuum. In order to estimate the contribution of the 528(6) keV and 926(15) keV peaks to the background estimation, they were fit using GF2 varying the width, position and height on a continuous quadratic background. The cross sections for the 528(6) keV and 926(15) keV peaks are 4.8(4) mb and 5.0(10) mb respectively.

While the origin of these peaks is unknown, we conclude that they originate from sources at rest in the laboratory and thus we expect them to contribute to the energy spectra in coincidence with ^{32,34}Mg as well. We estimate the contribution by scaling the ^{26}Mg spectrum. The cross sections for the 528(6) keV and 926(15) keV peaks are 4.8(4) mb and 5.0(10) mb respectively. This corresponds to 19(2) counts in the 528(6) peak and 12(2) counts in the 926(15) keV peak for ^{32}Mg. For ^{34}Mg the estimate is 8(1) and 5(1) counts respectively. In the projectile frame, the Doppler shift spreads the 528 keV peak over 300 keV and the 926 peak over a range of 512 keV on average for the ^{26,32,34}Mg spectra. For ^{32}Mg therefore, there are 0.060(6) counts per keV over the range of the 528 keV peak and 0.024(4) counts per keV from the 926 keV peak. In the ^{34}Mg projectile-frame spectrum, the estimates are 0.030(3) counts per keV and 0.010(2) counts per keV for the 528 keV and 926 keV peaks, respectively. The contributions by these 528(6) keV and 926(15) keV peaks in the ^{32,34}Mg spectra are minimal.

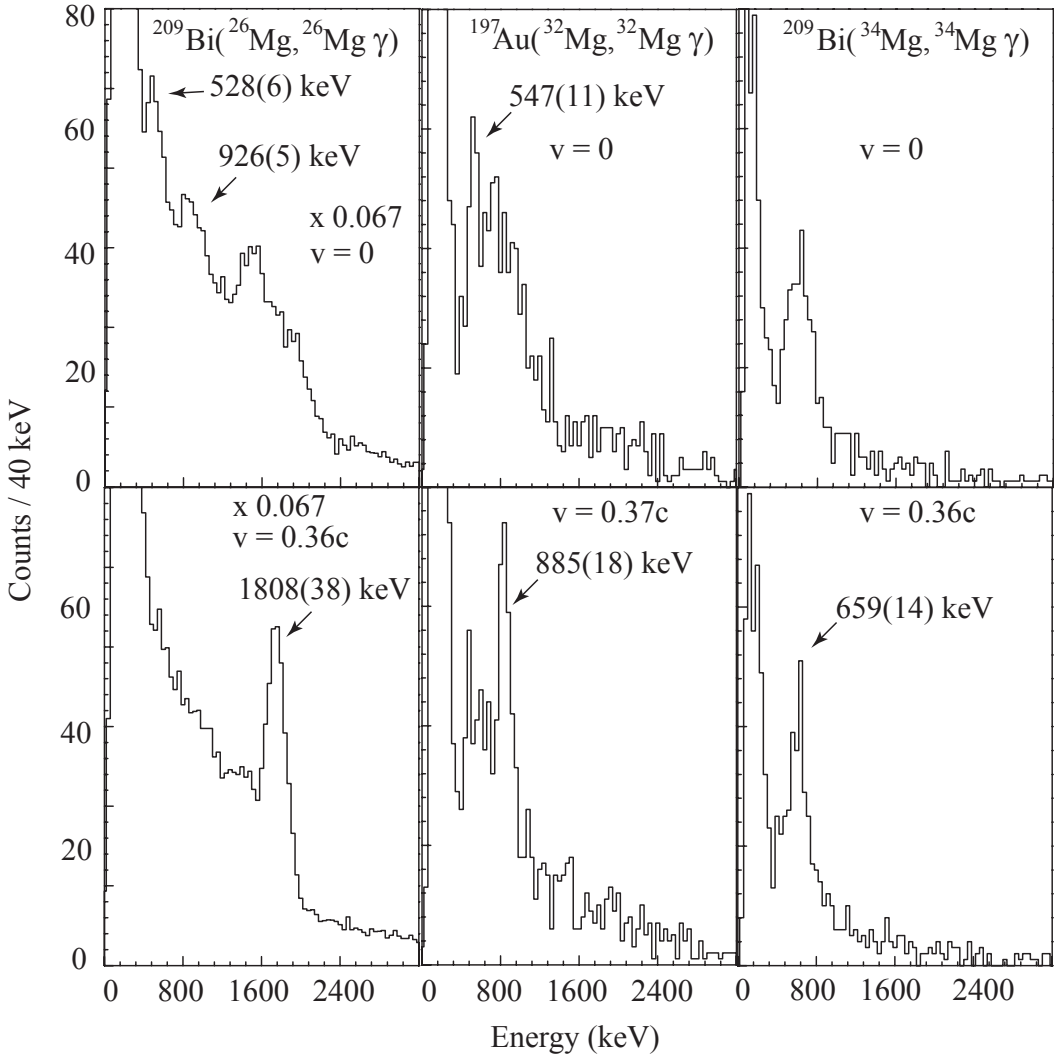

Figure 4.4: Gamma-ray energy spectra are shown for ^{26}Mg, ^{32}Mg, and ^{34}Mg, left, middle and right respectively. Spectra are displayed in the top panel without Doppler reconstruction, and in the bottom panels after they have been Doppler reconstructed to the projectile frame. Velocities listed for each of the reactions are mid-target values. The ^{26}Mg spectra are scaled by 0.067 for display purposes. In the top panel for ^{26}Mg the two background peaks as described in the text are shown. In the top panel for ^{32}Mg, the ^{197}Au γ-rays are seen. In the top panel for ^{34}Mg, the 659(14) keV γ-rays are Doppler boosted to 611(13) keV at 90°. The bottom panels show the reconstructed energies in the frame of the moving projectile.

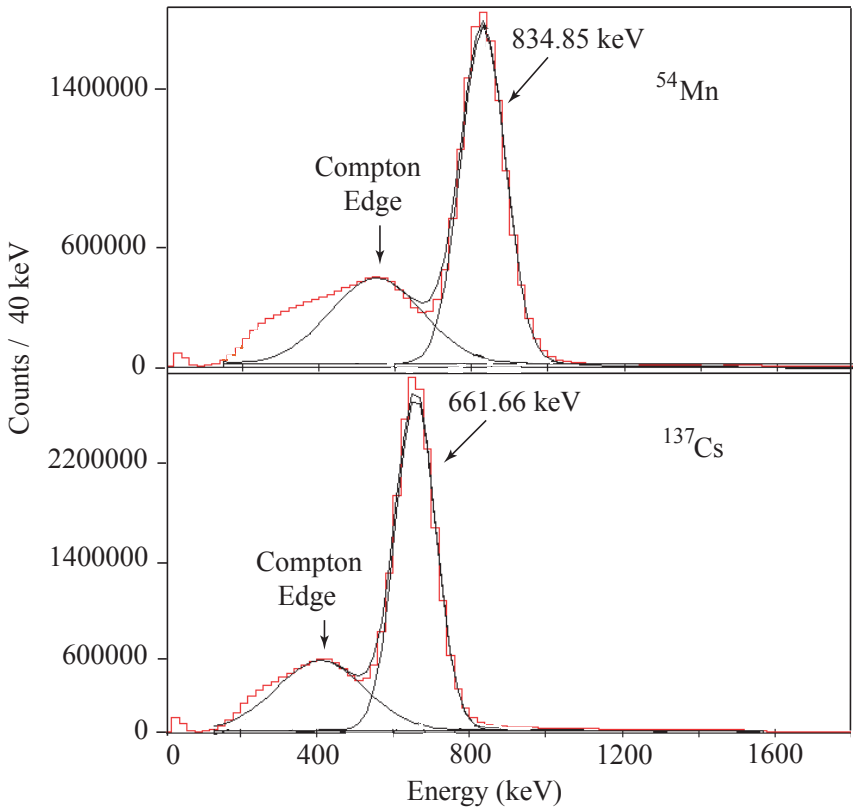

Figure 4.5: Measured energy spectra for the calibration sources ^{54}Mn (top) and ^{137}Cs (bottom). The spectra are used to determine the height and position of the Compton edge at these energies. The solid lines are GF2 fits. The energies listed are the adopted values [17].

4.4 ^{32}Mg and ^{197}Au

In the analysis of the ^{197}Au(^{32}Mg,^{32} Mgγ) reaction, de-excitation γ-rays resulting from the Coulomb excitation of both the projectile ^{32}Mg and the target ^{197}Au were binned for the sum of the 24 detectors and are shown in Figure 4.4. For each spectrum, the same-frame photopeak, Compton scattered ^{32}Mg events, and the Doppler broadened opposing-frame photopeak were fit on top of a quadratic background using GF2. In the γ-ray spectrum for ^{32}Mg we see a peak in the laboratory frame at 547 keV and another after the energies have been reconstructed to the projectile frame corresponding at 885 keV. The 547 keV photopeak is broadened after Doppler reconstruction to the projectile frame and is also visible. The 885 keV photopeak is visible in the laboratory frame as a broad peak as well.

4.4.1 Background and Compton Contribution

The shape of the background was taken from the ^{48}Ca fit described in Section 4.2 scaled by 0.042 the number of projectile nuclei and the number of target nuclei, N_t, N_p. The final quadratic for the background was $N = 2.15 - .0430x + .0005x^2$ for the ^{32}Mg and ^{197}Au energy spectra, where N is the number of counts in channel x.

The contribution to the spectra by Compton scattered ^{32}Mg events was estimated by fitting a Gaussian to the Compton edge for the calibration source ^{54}Mn which has a photopeak at 834 keV. The ^{54}Mn fit is displayed in Figure 4.5. The FWHM of this Gaussian is 2.10 times the FWHM of the photopeak, the height is 0.25 times the height of the photopeak. The height of the ^{32}Mg Compton edge was fixed by these parameters in the final ^{32}Mg and ^{197}Au fits.

Because of the energy resolution of the APEX array and the close proximity of the ^{32}Mg and ^{197}Au photopeaks, it is important to consider the width of the ^{32}Mg photopeak in the laboratory frame and the ^{197}Au photopeak in the projectile frame. The de-excitation γ-rays emitted by the ^{32}Mg projectile are spread over 650-1115 keV in the laboratory frame, while those emitted by the ^{197}Au target have a range of 434-745 keV in the projectile frame. In addition to the Doppler spread, the energy resolution of the NaI(Tl) array is taken into account when determining the width of the ^{32}Mg peak in the laboratory frame spectrum and ^{197}Au in the projectile frame spectrum. The range including the largest Doppler shifted value at its expected width due to the resolution of the array, and the smallest Doppler shifted value at its expected width is 310-890 keV for ^{197}Au target in the projectile frame and 508-1285 keV for the projectile ^{32}Mg in the target frame. These energy ranges are used to determine the width of the opposing-frame photopeak in the final fit.

4.4.2 ^{197}Au

The peak observed at 547 keV is a superposition of contributions from the ^{197}Au photopeak, the Doppler broadened ^{32}Mg and the ^{32}Mg Compton edge. All of these contributions are considered. From the adopted $B(E2\uparrow)$ value of 4488(408) e^{2}fm^4 [77], the expected cross section for the $3/2^+ \rightarrow 7/2^+$ 547 keV transition to the first excited-state in ^{197}Au is 20 mb and the number of expected ^{197}Au de-excitation γ-rays is 90 for the reaction with ^{32}Mg. The energy resolution of the ^{197}Au peak in the target frame is expected to be 18.5% based on the analysis in Section 3.1.3. This corresponds to a FWHM of 101 keV and the standard deviation, σ, of 43 keV. The 547 keV peak is spread over 460-633 keV for a range of $\pm 2\sigma$. This peak along with the Doppler smeared ^{32}Mg peak was fit on top of the ^{48}Ca scaled background. In order to estimate the full contribution due to the Compton scattering of ^{32}Mg, the height of the Gaussian estimated from the ^{54}Mn Compton was 25% of the photopeak. In ^{32}Mg this corresponds 0.430(2) counts per keV. This height of 0.430(2) counts was multiplied by the range extending to $\pm 2\sigma$ of 461-633 keV of the ^{197}Au peak, resulting in a flat contribution by the Compton scattered events of 70(3) counts over the 172(7) keV. This is taken to be a maximum Compton contribution. There were 159(16) counts under the fit of the full Gaussian and subtracting the estimated Compton contribution resulted in 89(10) counts. This corresponds to a lower limit for the cross section for the Coulomb excitation of ^{197}Au of 21(3) mb and a lower limit for the $B(E2\uparrow)$ of 4609(876) e^{2}fm^4.

4.4.3 ^{32}Mg

The previously-measured and predicted $E(2_1^+)$ and $B(E2; 0_{g.s.}^+ \rightarrow 2_1^+)$ values are discussed in Section 1.5. The adopted $E(2_1^+)$ value is 885.5(7) keV with a $B(E2\uparrow)$ value of 390(70) e^{2}fm^4 [17] for the $0_{g.s.}^+ \rightarrow 2_1^+$ transition. Of the measurements of the $B(E2\uparrow)$, all of the $B(E2; 0_{g.s.}^+ \rightarrow 2_1^+)$ values agree with the adopted value when the

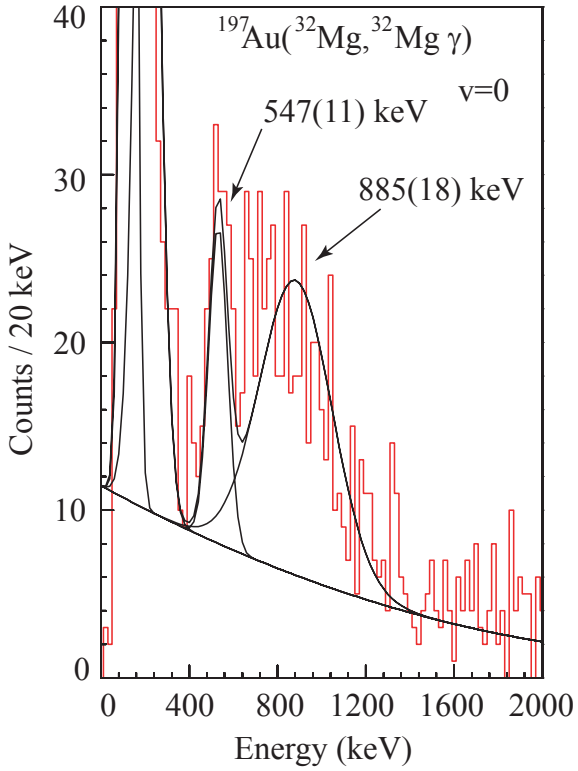

Figure 4.6: ^{197}Au energy spectrum showing the fit determined with GF2. The Doppler-broadened photopeak of ^{32}Mg is included with the ^{197}Au photopeak.

data are analyzed the same way, with the exception of [41] who measured the large value of 622(90) e^2fm^4 [41].

The energy spectrum for ^{32}Mg after reconstruction to the projectile frame shows two peaks, one at 885 keV and a broad peak at 547 keV corresponding to the transition in the ^{197}Au target nuclei. The ^{32}Mg peak was fit in a similar manner to the ^{197}Au peak. The background was again scaled by $N_t N_p$ from the ^{48}Ca fit and the Doppler broadened ^{197}Au peak and ^{32}Mg Compton edge fit with the parameters determined above. The 885 keV photopeak is also fit with a Gaussian, and while the 1436 keV γ-ray [25, 38, 42, 43] is noticable, there are only a few counts in the peak. The fit is shown in Figure 4.7. The ^{197}Au peak spread over $\pm 2\sigma$ was 351-842 keV.

The Compton contribution by ^{32}Mg was estimated by multiplying the height of the Compton edge expected from the ^{54}Mn source measurement over that range. The height of the ^{54}Mn Compton edge is 25% the height of the photopeak, corresponding

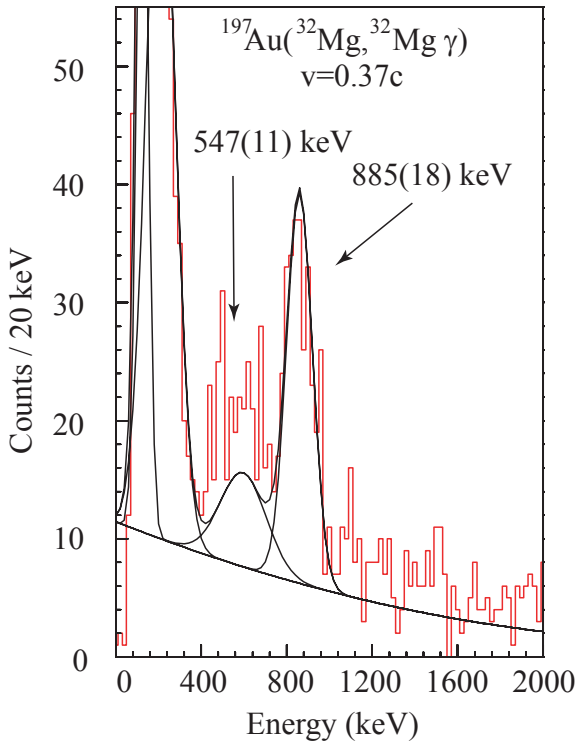

Figure 4.7: ^{32}Mg energy spectrum after Doppler reconstruction in the projectile frame showing the fit determined using GF2.

to 0.430(2) counts at the height of the Compton edge for ^{32}Mg. This height multiplied by the range of the ^{197}Au peak leads to an expected contribution to the spectrum in the range 351-842 keV of 207 counts by the Compton edge of ^{32}Mg and the Doppler broadened ^{197}Au peak together.

The result of the fit of the ^{32}Mg photopeak with no correction for feeding from the 2321 keV state is 252(25) counts in the ^{32}Mg photopeak at 885(18) keV, and an average of 101(33) counts due to the Doppler broadened ^{197}Au peak. The Coulomb excitation cross section is 91(10) mb and the $B(E2; 0^+_{g.s} \rightarrow 2^+_1)$ value extracted from our data for ^{32}Mg is 447(57) e^{2}fm^4 which results in a value for $|\beta_2|$ of 0.51(3).

We treat the feeding of the 885 keV state by the 2321 keV state as in [25]. Although the number of counts in the 1436 keV peak is small compared to the photopeak of the ^{32}Mg which has 252(25) counts, a maximum area under this peak of 41 counts is estimated by multiplying the height of the highest channel above the background, approximately 12 counts, times a width of 2σ above and below 1436 keV, where

$\sigma = 68$ keV is the standard deviation obtained from the expected FWHM of 160 keV. Because the actual area of the peak does not extend over the full area of the rectangle defined by the width $1436 \pm 2\sigma$ keV times the height of the highest channel over the background, the area of this rectangle was then divided by 2 to obtain an estimate for the maximum number of counts under the 1436 keV peak.

Because we do not know the spin and parity assignment for the 2321 keV state, we compare values for transition probabilities for E1, M1 and E2 transitions extracted from our estimated maximum number of counts in the 1436 keV peak to those listed as recommended upper limits by Reference [50]. The reduced transition probabilities extracted from our measured maximum number of counts corresponding to a cross secition of 23 mb for this setup in the 1436 keV peak are $B(E1; 0^+_{g.s.} \rightarrow 1^-) = 0.004$ e^{2}fm^2, $B(M1; 0^+_{g.s.} \rightarrow 1^+) = 0.36$ μ^2_{N}, $B(E2; 0^+_{g.s.} \rightarrow 2^+) = 115$ e^{2}fm^4 and $B(M2; 0^+_{g.s.} \rightarrow 1^-) = 12$ μ^2_{N}fm^2. The recommended upper limits are $B(E1; 0^+_{g.s.} \rightarrow 1^-) = 0.06$ e^{2}fm^2, $B(M1; 0^+_{g.s.} \rightarrow 1^+) = 8.95$ μ^2_{N}, $B(E2; 0^+_{g.s.} \rightarrow 2^+) = 600$ e^{2}fm^4 and $B(M2; 0^+_{g.s.} \rightarrow 1^-) = 830$ μ^2_{N}fm^2. The only transition for which our measured value exceeds the recommended upper limit is the M2 transition. The number of γ-rays actually emitted at 1436 keV can be estimated by making an efficiency correction to the estimated number of counts in the 1436 keV peak in our spectrum. The value for an efficiency-corrected number of counts emitted at 1436 keV is 372 counts. For each of these 372 counts, a γ-ray is emitted at 885 keV and detected with an efficiency of 18%. This corresponds to a maximum 67 counts detected in the 885 keV photopeak that are caused by feeding from the 2321 keV level. With this correction, the number of 885 keV de-excitation γ-rays becomes maximum 185(25), which yields a $B(E2\uparrow)$ minimum value of 328(48) e^{2}fm^4 and the minimum deformation parameter $|\beta_2|$ of 0.42(3) including the maximum correction for feeding from the 2321 keV state.

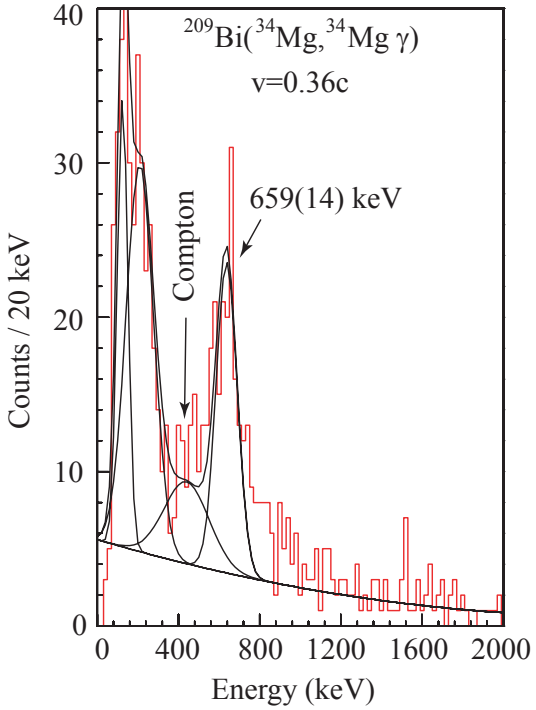

Figure 4.8: ^{34}Mg energy spectrum. The Compton edge estimate is shown for demonstration purposes only. The actual fit did not include this Gaussian for the Compton edge.

4.5 ^{34}Mg

The previously-measured $E(2_1^+)$ and $B(E2; 0_{g.s.}^+ \rightarrow 2_1^+)$ values are discussed in Section 1.6. These measurements indicate that ^{34}Mg is more collective than ^{32}Mg [38, 102].

The energy spectra for ^{34}Mg are shown in Figure 4.4. One peak is visible in each of the spectra. In order to fit the photopeak after Doppler reconstruction to the projectile frame, a Gaussian was fit on top of the parametrized ^{48}Ca background. The background was taken as the form of the ^{48}Ca fit scaled by the number of target and projectile nuclei, $N_t N_p$, a factor of 0.016 for ^{34}Mg. The quadratic background is described by $N = 0.86 - .0173x + .0003x^2$ for the ^{34}Mg energy spectra, where N is the number of counts in channel x. Gamma-ray spectra gated on both time- and particle-gates in coincidence with ^{34}Mg are shown in Figure 4.4.

The contribution to the spectra by Compton scattered ^{34}Mg events was estimated

Table 4.1: Coulomb excitation cross section parameters for the $0^+_{g.s.} \rightarrow 2^+_1$ transitions in ^{26,32,34}Mg and ^{96}Mo. E_γ is the γ-ray energy, N_t is the number of nuclei in the target, N_B is the number of incoming projectile nuclei, N_γ is the number of detected γ rays, σ is the Coulomb excitation cross section, and the $B(E2\uparrow)$ is the reduced electric quadrupole transition probability.

Nucleus	E_γ (keV)	θ_{cm} deg.	v/c	N_t	N_B	N_γ	σ (mb)
^{26}Mg	1808(38)	2.68	0.36	2.82×10^{21}	2.51×10^{8}	3376(116)	44.4(19)
^{96}Mo	778(16)	3.69	0.34	5.63×10^{20}	1.44×10^{8}	3273(134)	182(11)
^{32}Mg	885(18)	2.63	0.37	2.96×10^{21}	5.25×10^{6}	252(25)	90.6(95)
^{34}Mg	659(14)	2.77	0.36	2.82×10^{21}	2.14×10^{6}	166(28)	126(22)

by fitting a Gaussian to the Compton edge for the calibration source ^{137}Cs which has a photopeak at 662 keV. The ^{137}Cs fit is displayed in Figure 4.5. The FWHM of this Gaussian is 2.13 times the FWHM of the photopeak, the height is 0.22 times the height of the photopeak. The height of the Compton edge was fixed by these parameters in order to estimate the Compton contribution to the final ^{34}Mg fit. Contributions to the spectrum by ^{209}Bi target excitations can be neglected. Less than one count total is expected from target excitations over the energy range of 715-1210 keV.

The final fit of ^{34}Mg was performed by constraining the width of the peak to 19.1% FWHM, according to the analysis in Section 3.1.3. For an energy near 650 keV as is seen in the ^{34}Mg spectrum, the energy resolution of the APEX array is expected to be 0.19. The peak fit on top of the quadratic background given above is shown in Figure 4.8 with an additional display of a Gaussian representing the Compton edge. The Compton edge was not included in the final fit. The number of γ rays in the ^{34}Mg photopeak is 166(28), at an energy of 659(14) keV. The resulting cross section is 126(22) mb and the $B(E2; 0^+_{g.s.} \rightarrow 2^+_1)$ value extracted from our data is 541(102) e^2fm^4 corresponding to the deformation parameter $|\beta_2| = 0.54(5)$.

Table 4.2: Extracted and adopted $B(E2\uparrow)$ values for the $0^+_{g.s.} \rightarrow 2^+_1$ transitions in ^{26,32,34}Mg and ^{96}Mo. E_γ is the γ-ray energy, σ is the Coulomb excitation cross section, and $B(E2\uparrow)$ is the reduced electric quadrupole transition probability. The ^{32}Mg extracted value listed has not been corrected for feeding of the 885 keV state by the 2321 keV state.

Nucleus	E_γ (keV)	σ (mb)	Extracted $B(E2\uparrow)$ e^2fm^4	Adopted $B(E2\uparrow)$ e^2fm^4
^{26}Mg	1808(38)	44.4(19)	315(48)	305(13)
^{96}Mo	778(16)	182(11)	2640(260)	2711(50)
^{32}Mg	885(18)	90.6(95)	447(57)	390(70)
^{34}Mg	659(14)	126(22)	541(102)	none

4.5.1 Nuclear Contribution

The possibility for contribution to the cross sections of ^{26,32,34}Mg by direct nuclear reactions was evaluated through an ECIS88 coupled-channels calculation [103]. The calculation assumes isoscalar behavior for which the Coulomb deformation β_C is assumed to be the same as the nuclear deformation β_N, $\beta_C = \beta_N$. The optical model parameter set is taken from that determined for the ^{17}O+^{208}Pb reaction [47]. Figure 4.9 shows the calculated differential cross sections for ^{34}Mg, with Coulomb only contributions and with Coulomb plus nuclear contributions, versus scattering angle. The calculations show the nuclear contributions to be at maximum 7% for all 3 nuclei. Similarly small contributions have also been reported in References [12] and [82].

4.6 ^{35,36}Al and ^{37}Si

In addition to the even-even nuclei already discussed, three odd nuclei were constituents of the ^{34}Mg cocktail beam. Gamma-rays resulting from Coulomb excitation reactions of ^{35,36}Al and ^{37}Si with the 0.980 g/cm^2 ^{209}Bi target were recorded and analyzed following the general analysis procedure outlined above. Excited state energies and $B(\pi\lambda)$ values were measured and extracted. Particle identification was performed by placing software gates on the plastic phoswich detector's energy loss versus time-

of-flight spectrum. The energy spectra were constrained by these particle gates as well as prompt time cuts and then fit using GF2. The form of the background was again taken from the ^{48}Ca background scaled by the number of projectile nuclei and the number of target nuclei. The spectra are shown in Figure 4.10

Of these three nuclei, only ^{35}Al and ^{37}Si have been observed via Coulomb excitation before. Excitation energies and $B(E2\uparrow)$ values were observed [29] to be 1006(19) keV and 142(52) e^{2}fm^4 for ^{35}Al and 1437(27) keV and 101(45) e^{2}fm^4 for ^{37}Si. The ground state spin and parity for ^{37}Si has a value of $(7/2^-)$ [104] while for ^{35,36}Al there are no adopted values for the spin and parity. The ground state spin and parity for ^{35,36}Al and ^{37}Si have been predicted by an OXBASH shell model calculations [105] to be $5/2^+$ for ^{35}Al, 4^- or 5^- for ^{36}Al and $7/2^-$ for ^{37}Si. Excited state energies and $B(\pi\lambda)$ values for ^{36}Al have not been measured previously.

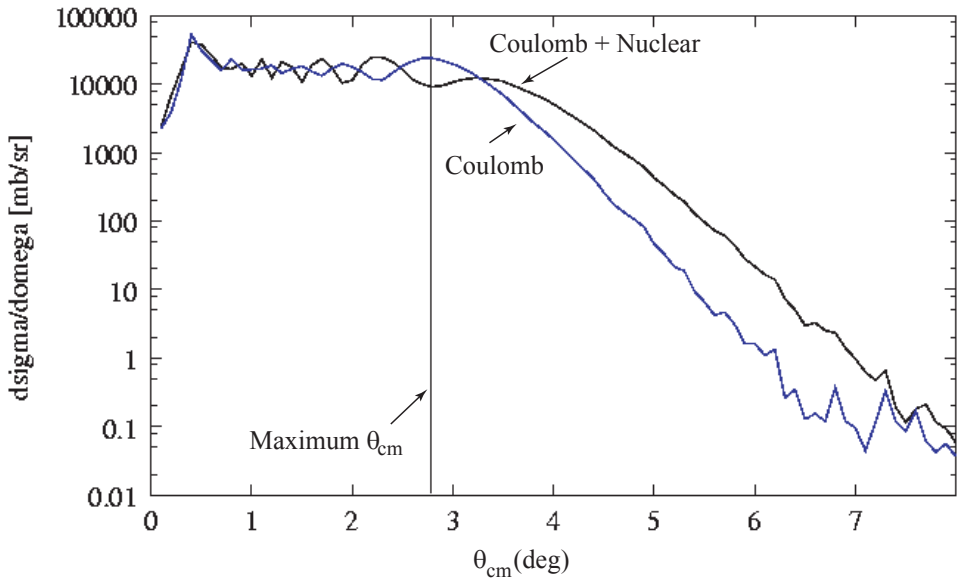

Figure 4.9: ECIS calculation for ^{34}Mg on ^{209}Bi at 67.3 MeV/nucleon. The differential cross section is shown as a function of center-of-mass scattering angle for both Coulomb only and Coulomb plus nuclear contributions.

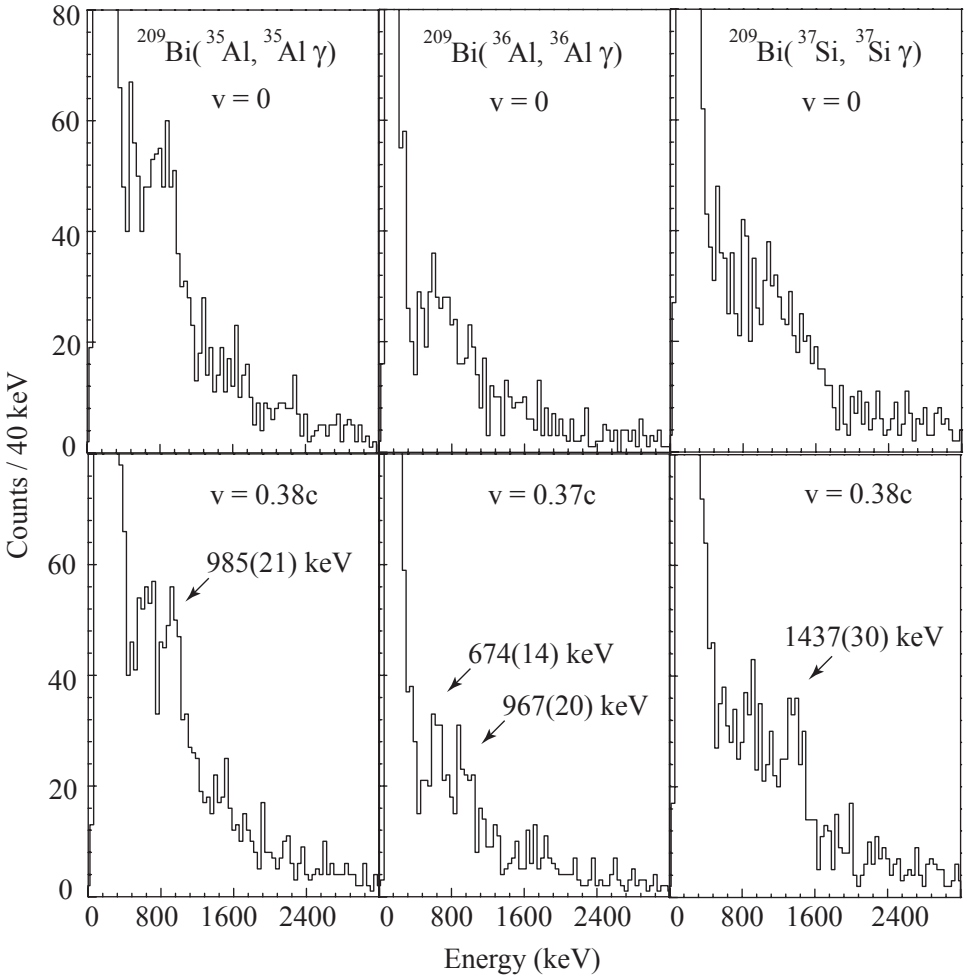

Figure 4.10: Energy spectra are shown for ^{35}Al, ^{36}Al, and ^{37}Si, left, middle and right respectively. The bottom panels show the γ-rays after they have been Doppler reconstructed in the projectile frame. Velocities listed for each of the reactions are mid-target values.

4.6.1 ^{37}Si

One prominent γ-ray peak in coincidence with ^{37}Si is observed at 1437(30) keV. The projectile-frame spectrum is shown in Figure 4.11 as it was fit with GF2. The background was scaled from the ^{48}Ca background by a factor of 0.041 obtained by scaling by the number of target nuclei times the number of incoming projectile nuclei, $N_t N_p$. The form of the quadratic background is $N = 2.12 - 0.042x + 0.0008x^2$, where N is the number of counts in channel x. The width of the peak was again fixed to the value obtained from the expected energy resolution of the array discussed in Section 3.1.3. Contributions by the Compton continuum to the energy spectrum were also estimated in the same manner as the ^{32}Mg analysis from the ^{54}Mn source peak.

The ^{37}Si photopeak fit yielded a total of 144(22) γ-rays for the 1437(30) keV transition. Cross sections were extracted for assumed E1 ($7/2^- \rightarrow 9/2^+$), M1 ($7/2^- \rightarrow 9/2^-$), E2 ($7/2^- \rightarrow 9/2^-$) and E2 ($7/2^- \rightarrow 11/2^+$) transitions resulting in 90(14) mb, 91(14) mb, 90(14) mb, and 85(13) mb respectively. The γ-ray angular distributions do not affect cross sections significantly. From shell model calculations [105], the ground state is expected to have a spin and parity of $7/2^-$. The corresponding $B(\pi\lambda)$ values are $B(E1; 7/2^- \rightarrow 9/2^+) = 0.078(12)$ e^{2}fm^2, $B(M1; 7/2^- \rightarrow 9/2^-) = 0.0079(11)$ μ_N^2, $B(E2; 7/2^- \rightarrow 9/2^-) = 380(63)$ e^{2}fm^4 and $B(E2; 7/2^- \rightarrow 11/2^-) = 360(62)$ e^{2}fm^4.

4.6.2 ^{35}Al

One clearly distinguishable peak is observed at 985(21) keV in coincidence with ^{35}Al and are shown in Figure 4.12 with the GF2 fit. The lower energy γ-rays centered at approximately 650 keV are of unknown origin as they are visible in the laboratory-frame spectrum as well, and so were not fit. Gamma rays in coincidence with ^{35}Al are shown in Figure 4.12 with the GF2 fit. The background was scaled from the ^{48}Ca background by a factor of 0.048 obtained by scaling by the number of target nuclei times the number of incoming projectile nuclei, $N_t N_p$ and is of the form $N =$

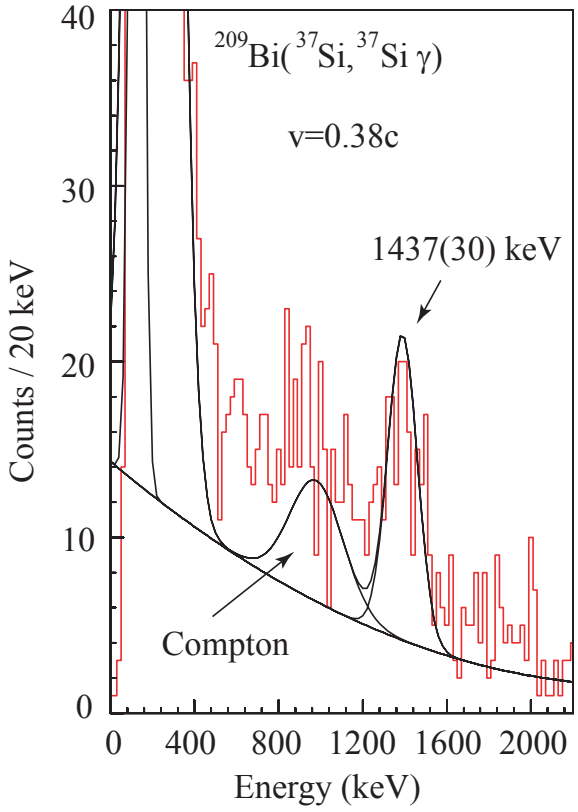

Figure 4.11: Energy spectrum after Doppler reconstruction in the projectile frame in coincidence with ^{37}Si. The fit includes both the photopeak and the estimate for the position and height of the Compton edge.

$2.48 - 0.049x + 0.001x^2$, where N is the number of counts in channel x. The width of the peak was again fixed to the value obtained from the expected energy resolution of the array discussed in Section 3.1.3. Contributions by the Compton continuum were also estimated in the same manner as the ^{32}Mg analysis from the ^{54}Mn source peak.

The peak fit yielded a total of 193(25) γ rays corresponding to the 985(21) keV transition. Cross sections were extracted for assumed E1 ($5/2^+ \rightarrow 7/2^-$) , M1 ($5/2^+ \rightarrow 7/2^+$), E2 ($5/2^+ \rightarrow 7/2^+$) and E2 ($5/2^+ \rightarrow 9/2^+$) transitions resulting in 80(11) mb, 81(12) mb, 80(12) mb and 75(10) mb, respectively. We assume the spin and parity of the ground state to be $5/2^+$ as calculated with the OXBASH shell model code [105]. The corresponding $B(\pi\lambda)$ values are $B(E1; 5/2^+ \rightarrow 7/2^-) = 0.053(7)$ e^{2}fm^2, $B(M1; 5/2^+ \rightarrow 7/2^+) = 0.0053(8)\ \mu_N^2$, $B(E2; 5/2^+ \rightarrow 7/2^+) = 330(51)$ e^{2}fm^4, and $B(E2; 5/2^+ \rightarrow 9/2^+) = 310(45)$ e^{2}fm^4.

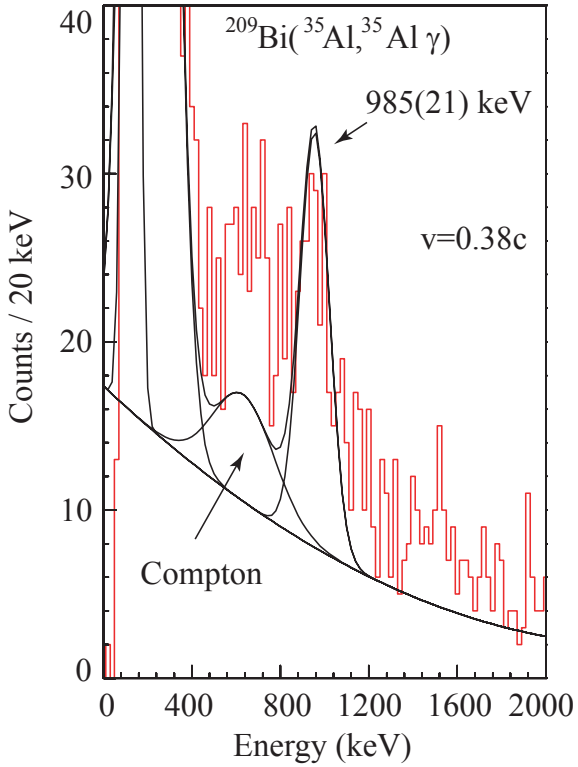

Figure 4.12: Energy spectrum after Doppler reconstruction in the projectile frame for ^{35}Al. The fit includes both the photopeak and the estimate for the position and height of the Compton edge.

4.6.3 ^{36}Al

Two γ-ray peaks are observed in coincidence with ^{36}Al at 674(14) keV and 967(20) keV. The ^{36}Al spectrum and fit are shown in Figure 4.13. The background was scaled from the ^{48}Ca background by a factor of 0.024 obtained by scaling by the number of target nuclei times the number of incoming projectile nuclei, $N_t N_p$. The form of the quadratic background is $N = 1.24 - 0.025x + 0.0005x^2$, where N is the number of counts in channel x. The width of the peaks were again fixed to the value obtained from the expected energy resolution of the array discussed in Section 3.1.3. Contributions by the Compton continuum were estimated from the ^{137}Cs source for the 674(14) keV line, and from the ^{54}Mn peak for the 967(20) keV peak.

The lower energy 674(14) keV peak fit yielded a total of 60(11) γ-rays. Cross sections were extracted for assumed E1, M1 and E2 transitions resulting in the values

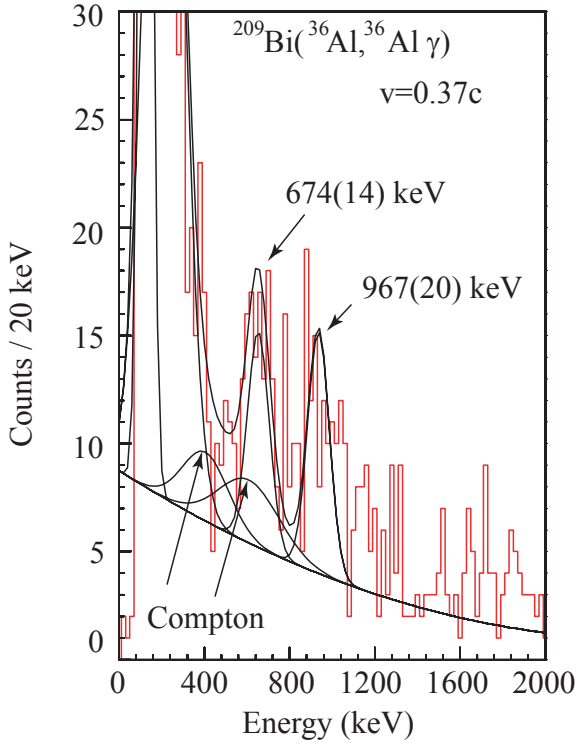

Figure 4.13: Energy spectrum after Doppler reconstruction in the projectile frame in coincidence with ^{36}Al. The fit includes both the photopeak and the estimate for the position and height of the Compton edge.

listed in Table 4.3. Shell model calculations for this nucleus reveal two possibilities for the spin and parity of the ground state [105]. It could either have a J^π value of $4-$ or a value of 5^-. The corresponding $B(\pi\lambda)$ values for a 4^- ground state are a $B(E1; 4^- \rightarrow 5^+)$ value of 0.02(4) e^2fm^2, $B(M1; 4^- \rightarrow 5^-) = 0.0020(3)\ \mu_N^2$, $B(E2; 4^- \rightarrow 5^-) = 160(33)\ e^2fm^4$ and $B(E2; 4^- \rightarrow 6^-) = 150(27)\ e^2fm^4$. For a 5^- ground state, the values extracted from the measured cross sections are $B(E1; 5^- \rightarrow 6^+) = 0.02(4)$ e^2fm^2, $B(M1; 5^- \rightarrow 6^-) = 0.0020(3)\ \mu_N^2$, $B(E2; 5^- \rightarrow 6^-) = 160(31)\ e^2fm^4$ and $B(E2; 5^- \rightarrow 7^-) = 150(27)\ e^2fm^4$.

The higher energy 967(20) keV peak was found to have 89(12) counts. Cross sections were extracted for assumed E1, M1 and E2 transitions resulting in the values listed in Table 4.3. For the assumption of a 4^- ground state the transition probabilities are $B(E1; 4^- \rightarrow 5^+) = 0.047(7)\ e^2fm^2$, $B(M1; 4^- \rightarrow 5^-) = 0.0050(7)\ \mu_N^2$, $B(E2; 4^- \rightarrow 5^-) = 310(45)$ and $B(E2; 4^- \rightarrow 6^-) = 280(41)\ e^2fm^4$, while those for an assumed 5^-

ground state are $B(E1; 5^- \rightarrow 6^+) = 0.047(7)$ e^{2}fm^2, $B(M1; 5^- \rightarrow 6^-) = 0.0050(7)$ μ_N^2, $B(E2; 5^- \rightarrow 6^-) = 300(43)$ e^{2}fm^4, and $B(E2; 5^- \rightarrow 7^-) = 280(41)$ e^{2}fm^4.

The reduced transition probabilities and deformation parameters extracted from our observations are discussed as they relate to theoretical calculations in Chapter 5.

4.6.4 Upper Limits

Because the spin and parity of the higher-lying states are unknown, the $B(\pi\lambda)$ values extracted from our measured cross sections were compared to the recommended upper limits for the electromagnetic transitions listed in References [50,106]. The recommended upper limits for this mass region are a $B(E1)$ value of 0.1 W.u., a $B(M1)$ value of 5 W.u. and a $B(E2)$ value of 100 W.u. The smallest $B(E2)$ values in this mass region are on the order of 3 W.u. Because the largest M1 transition strengths correspond to the the smallest E2 strengths, an observation of a strong transition can be assumed to be E2 in nature. Here we compare the recommended upper limits with our measurements analyzed under the assumption of M1, E1 and E2 transitions. The cross sections and extracted transition probabilities for each of the considered transitions are listed in Table 4.3.

For ^{37}Si the recommended upper limits are 0.07 e^{2}fm^2, 8.95μ_N^2 and 732 e^{2}fm^4 for the corresponding $B(\pi\lambda)$ values. From our measured values listed above, we cannot exclude any of the transitions. For ^{35}Al, the recommended upper limits are 0.07 e^{2}fm^2, 8.95 μ_N^2 and 680 e^{2}fm^4 for the corresponding $B(\pi\lambda)$ values. Again, we cannot exclude E1, M1 or E2 transitions. For the 674(14) keV peak in ^{36}Al the recommended upper limits are 0.07 e^{2}fm^2, 8.95 μ_N^2 and 706 e^{2}fm^4 respectively for the corresponding $B(\pi\lambda)$ values, none of which can be excluded. Finally, for the 967(20) keV peak in ^{36}Al, the recommended upper limits are 0.07 e^{2}fm^2, 8.95 μ_N^2 and 706 e^{2}fm^4 for the corresponding $B(\pi\lambda)$ values. Comparing our measurements to these upper limits, we again cannot exclude E1, M1 or E2 transitions as possible origins of the observed γ-rays.

Table 4.3: Coulomb excitation cross section parameters for transitions assumed for ^{35,36}Al and ^{37}Si. E1, M1 and E2 are considered as possible transitions. Assumed transitions are listed and explained in the text. E_γ is the γ-ray energy, N_t is the number of nuclei in the target, N_p is the number of incoming projectile nuclei, N_γ is the number of detected γ rays, σ is the Coulomb excitation cross section, and the $B(\pi\lambda\uparrow)$ is the reduced transition probability. The units for the $B(\pi\lambda\uparrow)$ values are $e^2fm^{2\lambda}$ for $E\lambda$ transitions and $\mu_N^2 fm^{2\lambda-2}$ for $M\lambda$ transitions.

Nucleus	E_γ (keV)	Assumed Transition	N_p	N_γ	σ (mb)	$B(\pi\lambda\uparrow)$
^{35}Al	985(21)	E1; $\frac{5}{2}^+ \rightarrow \frac{7}{2}^-$	6.22×10^6	193(25)	80(11)	0.053(7)
		M1; $\frac{5}{2}^+ \rightarrow \frac{7}{2}^+$			81(12)	0.0053(8)
		E2; $\frac{5}{2}^+ \rightarrow \frac{7}{2}^+$			80(12)	330(51)
		E2; $\frac{5}{2}^+ \rightarrow \frac{9}{2}^+$			75(10)	310(45)
^{36}Al	674(14)	E1; $4^- \rightarrow 5^+$	3.06×10^6	60(11)	37(7)	0.02(4)
		M1; $4^- \rightarrow 5^-$			38(7)	0.0020(3)
		E2; $4^- \rightarrow 5^-$			36(7)	160(33)
		E2; $4^- \rightarrow 6^-$			35(6)	150(27)
		E1; $5^- \rightarrow 6^+$			37(7)	0.02(4)
		M1; $5^- \rightarrow 6^-$			38(7)	0.0020(3)
		E2; $5^- \rightarrow 6^-$			37(7)	160(31)
		E2; $5^- \rightarrow 7^-$			35(6)	150(27)
	967(20)	E1; $4^- \rightarrow 5^+$		89(12)	73(10)	0.047(7)
		M1; $4^- \rightarrow 5^-$			74(10)	0.0050(7)
		E2; $4^- \rightarrow 5^-$			73(9)	310(45)
		E2; $4^- \rightarrow 6^-$			68(9)	280(41)
		E1; $5^- \rightarrow 6^+$			73(10)	0.047(7)
		M1; $5^- \rightarrow 6^-$			74(10)	0.0050(7)
		E2; $5^- \rightarrow 6^-$			72(9)	300(43)
		E2; $5^- \rightarrow 7^-$			69(9)	280(41)
^{37}Si	1437(30)	E1; $\frac{7}{2}^- \rightarrow \frac{9}{2}^+$	5.39×10^6	144(22)	90(14)	0.078(12)
		M1; $\frac{7}{2}^- \rightarrow \frac{9}{2}^-$			91(14)	0.0079(11)
		E2; $\frac{7}{2}^- \rightarrow \frac{9}{2}^-$			90(14)	380(63)
		E2; $\frac{7}{2}^- \rightarrow \frac{11}{2}^-$			85(13)	360(62)

Chapter 5

Discussion

Gamma-rays resulting from the transition from states populated via intermediate-energy Coulomb excitation and the ground state have been observed for the nuclei ^{26,32,34}Mg, ^{35,36}Al, ^{37}Si, ^{96}Mo and ^{197}Au. Energies of the observed γ-rays were measured and reduced electric quadrupole transition matrix elements were extracted from the measured Coulomb excitation cross sections. The observables reported in Chapter 4 are discussed here as compared to adopted values, previously measured values and theoretical calculations.

5.1 The Island-of-Inversion Nuclei ^{32,34}Mg

5.1.1 ^{32}Mg

Our measured $E(2_1^+)$ value of 885(18) keV and extracted $B(E2; 0_{g.s.}^+ \rightarrow 2_1^+)$ value without a feeding correction from the 2321 keV state of 447(57) e^{2}fm^4 agree with the other measured values [12, 25, 38, 39]. However, our value is not in direct agreement with the 622(90) e^{2}fm^4 $B(E2; 0_{g.s.}^+ \rightarrow 2_1^+)$ value measured by Reference [41], although it still agrees to within 2σ. The adopted, measured and calculated $B(E2; 0_{g.s.}^+ \rightarrow 2_1^+)$ values for ^{32}Mg are displayed in Figure 5.1. Several experiments have reported the 1436 keV γ-ray to be in coincidence with the 885 keV γ ray [26,38,40,42,43], and the

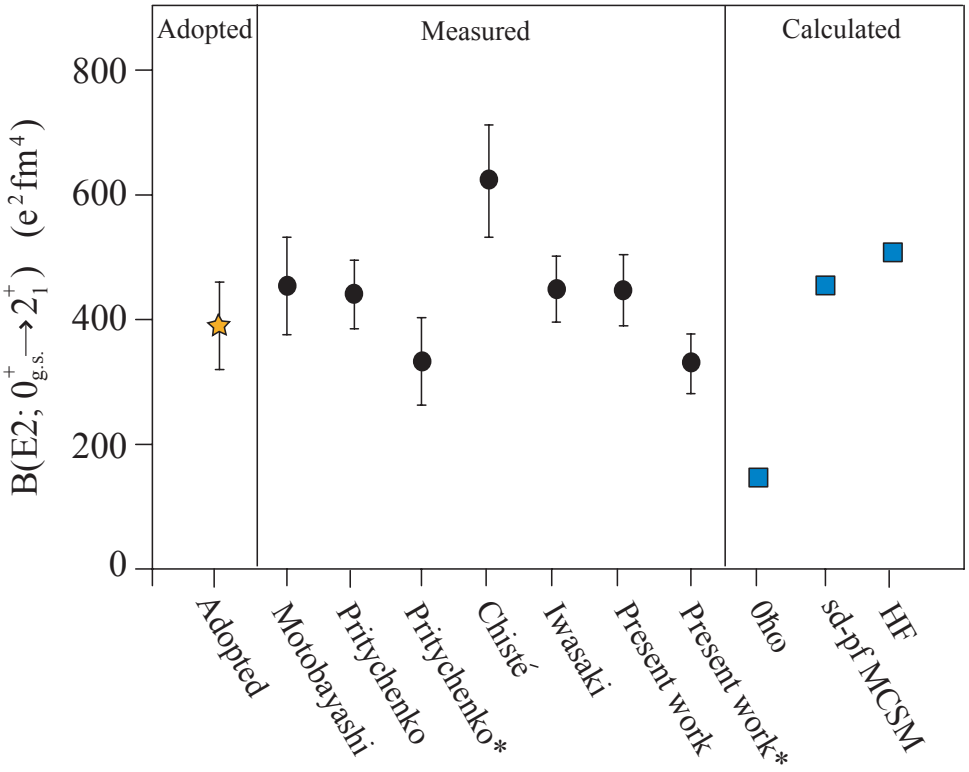

Figure 5.1: Reduced electric quadrupole transition probabilities, $B(E2; 0^+_{g.s.} \rightarrow 2^+_1)$, for ^{32}Mg. Values measured by Motobayashi *et al.* [12], Pritychenko *et al.* [25], Chisté *et al.* [41], Iwasaki *et al.* [39] and the present work are compared to the adopted value [17] and a $0\hbar\omega$ shell model calculation [107], the $sd-pf$ Monte Carlo Shell Model (MCSM) [22, 56], and an example of a Hartree-Fock calculation (HF) [59]. Asterisks indicate that the feeding of the 885 keV state by the 2321 keV state has been included in the analysis.

feeding of the 2^+_1 state is treated differently among the reports. The $B(E2\uparrow)$ value of 328(48) e^{2}fm^4 we obtain after including a contribution to the 885 keV peak by feeding from the 2321 keV state, agrees with the feeding-corrected value of 333(70) e^{2}fm^4 obtained by Ref. [25].

As discussed in Section 1.5, this $N = 20$ nucleus is significantly more collective than expected for a closed-shell nucleus. Although the investigation of the quadrupole moments in the sodium isotopes provides evidence that the region is most likely statically deformed [35], recent fragmentation studies by Ref [43] report an $E(4^+_1)/E(2^+_1)$ ratio of 2.6 for ^{32}Mg. This is not definitively close to either the rotational limit of

3.3 nor the vibrational of 2. In addition, their reported 2870 keV γ-ray is a decay directly to the ground state, and a good candidate for a second 2^+ level indicating a possibility for shape coexistence in the nucleus [43]. We cannot draw a conclusion about the possibility of a coexisting spherical excited state from our data.

Because the feeding from the 2321 keV state is not well-understood, we will compare our uncorrected values to the theory. Our $E(2_1^+)$, $B(E2; 0_{g.s.}^+ \rightarrow 2_1^+)$ and β_2 values agree with shell model calculations which include $2\hbar\omega$ intruder configurations in the ground state [30, 57] and as expected, deviate from $0\hbar\omega$ models [32]. The best agreement comes with the $sd-pf$ Quantum Monte Carlo Shell Model [22, 56], which predicts an $E(2_1^+)$ value of 885 keV, the $B(E2; 0_{g.s.}^+ \rightarrow 2_1^+)$ value to be 454 e^2fm^4 and a deformation parameter, β_2, of 0.51. The $E(4_1^+)/E(2_1^+)$ ratio predicted by this model is 2.55, and is in agreement with the measurement of Ref [43] contributing to the argument that the nucleus exhibits shape coexistence.

Hartree Fock models predict either a spherical shape [60, 61] or shape coexistence with more than one minimum in the plot of energy versus deformation parameter [58, 59]. The deformation parameter, $\beta_2 = 0.51(3)$ extracted from our measurement does not agree with the example of the spherical nucleus ^{40}Ca which has an adopted β_2 value of 0.123(11) [17]. An example of the shape coexistence is found in Reference [59] predicting a β_2 value of 0.54 and the $B(E2; 0_{g.s.}^+ \rightarrow 2_1^+)$ value of 507 e^2fm^4 for the prolate shape. Both of the calculations are in agreement with our measurement. Relativistic Mean Field calculations find the nucleus to be spherical [23, 62, 63]. The Angular Momentum Configuration Mixing model predicts a combination of prolate and oblate minima with a β_2 value of 0.36 for the prolate minimum [64]. Our measured value for $|\beta_2|$ is larger than this at 0.51(3).

5.1.2 ^{34}Mg

Three other experiments have been performed previously on ^{34}Mg. The first [25], placed an upper limit on the $B(E2; 0_{g.s.}^+ \rightarrow 2_1^+)$ value of 670 e^2fm^4. The second

measurement [38], found an $E(2_1^+)$ value of 660(10) keV via a double fragmentation experiment at RIKEN. Finally Ref. [39] used Coulomb excitation ^{208}Pb(^{34}Mg,^{34} Mgγ) to measure the $E(2_1^+)$ value of 656(7) keV, $B(E2;0_{g.s.}^+ \rightarrow 2_1^+) = 631(126)$ e^{2}fm^4, and a $\beta_2 = 0.58(6)$. Our measured $E(2_1^+)$ value of 659(14) agrees. Our $B(E2;0_{g.s.}^+ \rightarrow 2_1^+)$ value of 541(102) e^{2}fm^4, and β_2 value of 0.54(5) are slightly lower but still agree. The second γ-ray at 1460 keV seen by [38] does not appear in our spectrum.

All of the measurements agree with the $sd-pf$ Quantum Monte Carlo Shell Model (QMCSM) predictions of a first 2^+ excited state energy of 620 keV, a $B(E2;0_{g.s.}^+ \rightarrow 2_1^+)$ value of 570 e^{2}fm^4, and the β_2 value of 0.55 [22,56] as well as the $2\hbar\omega$ shell model predictions of a 660 keV $E(2_1^+)$ value, a $B(E2;0_{g.s.}^+ \rightarrow 2_1^+)$ value of 655 e^{2}fm^4, and a β_2 of 0.6 [57]. The $0\hbar\omega$ values [32] do not agree with the measurements. From this evaluation it is apparent that the intruder-configuration ground state explanation is supported by the experimental data, and ^{34}Mg can decidedly be included in the Island of Inversion.

Hartree Fock models predict a range of both prolate and oblate deformation parameters. The prolate predictions calculate β_2 values of 0.3-0.4 [58], 0.22 [61], and 0.46 [59] and the oblate calculation is a β_2 value equal to -0.1 which is close to spherical [60]. We measured a $|\beta_2| = 0.54(5)$. Our measurement also does not agree with the Relativistic Mean Field theory calculations for the deformation parameter of 0.3 [63], 0.162 [62], and 0.17 [23]. We find ^{34}Mg exhibits more collectivity than ^{32}Mg, contrary to the prediction of the Angular Momentum Projection and Configuration Mixing model which predicts a β_2 value of 0.36 [64] for both ^{32}Mg and ^{34}Mg .

5.2 ^{35,36}Al and ^{37}Si

Reduced transition probabilities were also extracted from measurements of the electromagnetic transitions in 3 neutron-rich nuclei with odd numbers of nucleons, ^{37}Si and ^{35,36}Al. ^{36}Al was until now unmeasured via Coulomb excitation. The spin and

parity of the states for all 3 nuclei are also unmeasured and so were assumed from an OXBASH Shell Model calculation [105]. The $B(\pi\lambda\uparrow)$ values extracted from assumed E1, M1 and E2 transitions were therefore compared to the recommended upper limits listed by Endt [50].

Our measured low-lying excited state energies for ^{37}Si and ^{35}Al, 1437(30) keV and 985(21) keV, are in agreement with those of Ibbotson *et al.* [108], 1437(27) keV and 1006(19) keV respectively. However, the values for the $B(E2\uparrow)$ extracted from our data, 362(62) e^2fm^4 and 360(24) e^2fm^4, differ significantly from Ibbotson's of 101(45) e^2fm^4 and 142(52) e^2fm^4. The discrepancy may be due to the low statistics in the Ibbotson experiment, as described in the reference. As mentioned, the 674(14) keV and 967(20) keV γ-rays in the ^{36}Al energy spectrum have not been measured before via Coulomb excitation. The adopted values for the nearest even-even nucleus ^{36}Si, with $N = 22$ and $Z = 14$, are a $B(E2; 0^+_{g.s.} \rightarrow 2^+_1)$ value of 190(60) e^2fm^4, an $E(2^+_1)$ value of 1399(25) keV and a deformation parameter β_2 of 0.259(42) [17]. This nucleus has two protons more than ^{34}Mg and is significantly less collective. As discussed in Reference [29], the quick onset for the difference in collectivity is also found for the $N = 20$ isotopes ^{34}Si and ^{32}Mg, and experimentally marks the boundary of the Island of Inversion. In comparison to these even-even nuclei, we can consider the strength of the $E2$ transitions extracted from our measurements of the odd nuclei to be lower limits of the collectivity in these odd nuclei. Our extracted $B(E2; 5/2^+ \rightarrow 9/2^+)$ value for ^{35}Al of 310(45) e^2fm^4 and $B(E2; 7/2^- \rightarrow 11/2^-) = 360(62)$ e^2fm^4 for ^{37}Si are higher than those of the even-even nuclei, while the observed states for ^{36}Al have $B(E2; 4^- \rightarrow 6^-)$ values that are comparable, at 150(27) e^2fm^4 and 280(41) e^2fm^4 for the two observed γ-rays.

5.3 Summary

In summary, first 2^+ excited states of the projectiles ^{26,32,34}Mg, ^{96}Mo, and ^{48}Ca have been populated via intermediate energy Coulomb excitation in one of the early experiments at the Coupled Cyclotron Facility at the NSCL. Low-lying states of the odd-nucleon nuclei ^{35,36}Al and ^{37}Si and the target nucleus ^{197}Au were also populated by the same method. The energy and number of de-excitation γ-rays were observed using the APEX NaI(Tl) array and reduced transition probabilities were extracted from the observed quantitites, thereby providing a means for examination of the excited states of these nuclei. ^{32}Mg and ^{34}Mg are predicted to be members of the Island of Inversion, and as such were expected to exhibit characteristics indicative of a $2\hbar\omega$ intruder ground state.

The reduced quadrupole transition probabilities extracted from the observations of the $0_{g.s.} \rightarrow 2_1^+$ electric transitions in ^{32,34}Mg indicate that they are extremely collective nuclei. The values for the $B(E2; 0_{g.s.}^+ \rightarrow 2_1^+)$ and quadrupole deformation parameters, β_2, agree with calculations made with shell models that include a $2\hbar\omega$ ground state configuration in the model space. Of the mean-field calculations our measurements agree with those that calculate a prolate deformed shape, or possibly shape coexistence in ^{32}Mg, although our data do not reveal the coexisting state. Beyond the mean-field, models tend to predict smaller β_2 values than our measurements.

We find ^{34}Mg to have a higher degree of collectivity than ^{32}Mg and that our measurement agrees with that of Iwasaki *et al.* [39]. As compared to the theory, our measurement contrasts with models which predict a spherical shape for ^{34}Mg as well as the $0\hbar\omega$ shell model. The measurement is in agreement with models that include the $2\hbar\omega$ intruder as the ground state such as the $sd - pf$ Quantum Monte Carlo Shell Model. There is a slightly better agreement with the QMCSM calculations as compared to the $2\hbar\omega$ shell model in Reference [30]. These results are summarized in Figure 5.2 in which our measurements are compared with adopted and calculated

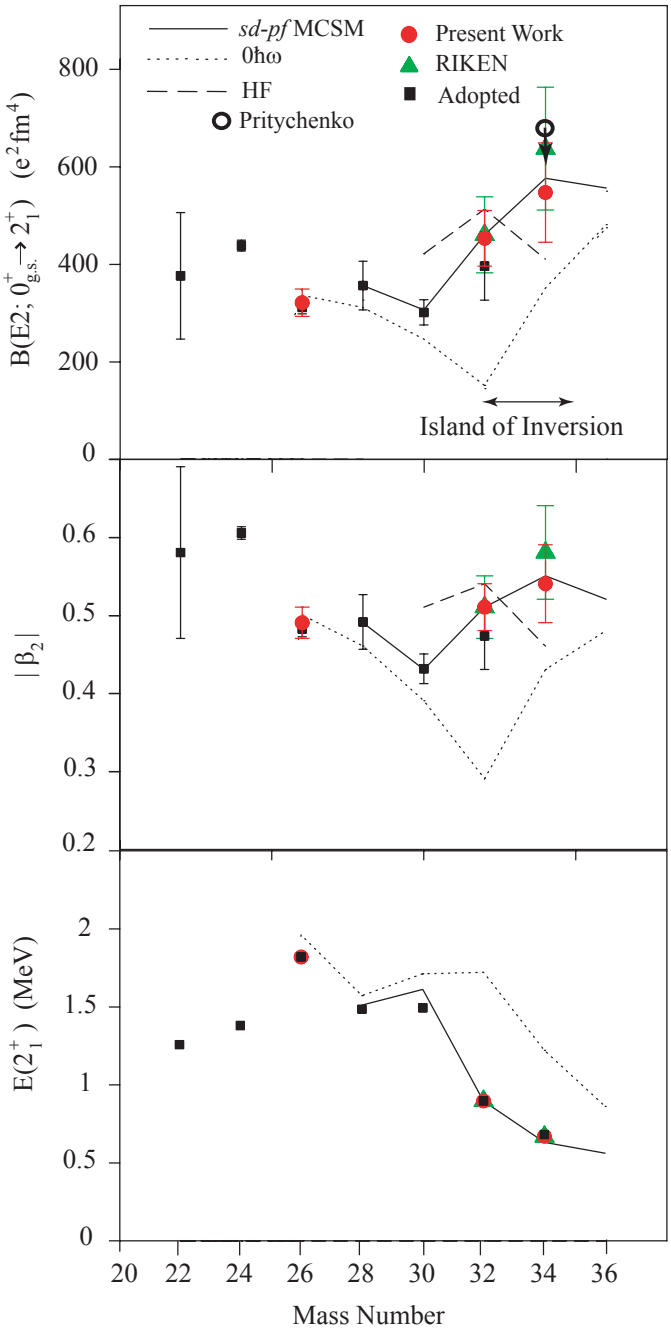

Figure 5.2: Reduced quadrupole transition probabilities, $B(E2; 0^+_{g.s.} \rightarrow 2^+_1)$, quadrupole deformation parameters, β_2, and first excited state energies, $E(2^+_1)$, for Mg isotopes with even numbers of neutrons. Values measured in the present work (circles), at RIKEN (triangles), and by Pritychenko *et al.* [25] (open circle) are compared to the adopted values (squares) as well as theoretical calculations (lines). The RIKEN measurement of ^{32}Mg is reported in Reference [12], while those for ^{34}Mg are the work of References [38, 39]. The $sd - pf$ Monte Carlo Shell Model (MCSM) [22, 56] values are connected by the solid line, the $0\hbar\omega$ shell model calculation ($0\hbar\omega$) [107] by the dotted line, and an example of a Hartree-Fock calculation [59] by the dashed line.

values for the reduced quadrupole transition probabilities, quadrupole deformation parameters and first 2^+ excited state energies for the magnesium isotopes. The figure demonstrates the evolution of collectivity in the magnesium isotopes with increasing numbers of neutrons, and thereby confirms the inclusion of ^{34}Mg in this anomalous group of collective nuclei near the magic number $N = 20$.

Although much work has already been done in the region of the Island of Inversion, many new opportunities for exploring the region have been created with the increased intensities of the rare-isotope beams currently being developed world-wide. With these increases, considerable advancements can be made through the measurement of the higher-lying states, such as the 4_1^+ state in ^{32}Mg, in order to confirm the suspected deformation of the region. Spectroscopic information on the $N = 24$ nucleus ^{36}Mg will provide information confirming the neutron boundary predicted by many models. While the high-Z boundary has been explored, the low-Z boundary also remains to be investigated. This further experimental exploration of the Island of Inversion may be feasible, should the construction of new rare-isotope beam facilities be completed, and is necessary in order to continue the investigation into the structure of these extremely rare, neutron-rich, anomalously-collective nuclei.

Appendix A

Weisskopf Single-Particle Estimates

A standard for estimating transition strengths between two states are transition probability estimates made from the extreme single-particle viewpoint. These are called Weisskopf single-particle estimates and involve moving a single nucleon from one state to the next without affecting the rest of the nucleus. The derivation for the single-particle estimates is found in Reference [109]. The results are outlined here.

For the reduced electric transition probability, the Weisskopf single-particle estimate, or one Weisskopf unit (W.u.), is

$$B_W(E\lambda) = \frac{1}{4\pi}\left(\frac{3}{\lambda+3}\right)^2 (1.2A^{1/3})^{2\lambda}\mathrm{e}^2\mathrm{fm}^{2\lambda}, \tag{A.1}$$

where λ is the multipolarity of the transition. The Weisskopf single-particle estimate for the reduced magnetic transition probability is written similarly,

$$B_W(M\lambda) = \frac{10}{\pi}\left(\frac{3}{\lambda+3}\right)^2 (1.2A^{1/3})^{2\lambda-2}\mu_{\mathrm{N}}^2\mathrm{fm}^{2\lambda-2}, \tag{A.2}$$

Table A.1: Electric and magnetic Weisskopf single-particle estimates for transition probabilities up to the first four multipoles.

Order in λ	$\mathcal{W}_W(E\lambda)$ (s^{-1})	$\mathcal{W}_W(M\lambda)$ (s^{-1})
1	1.02×10^{14} $A^{2/3}E_\gamma^3$	3.15×10^{13} E_γ^3
2	7.28×10^{7} $A^{4/3}E_\gamma^5$	2.24×10^{7} $A^{2/3}E_\gamma^5$
3	3.39×10 $A^{2}E_\gamma^7$	1.04×10 $A^{4/3}E_\gamma^7$
4	1.07×10^{-5} $A^{8/3}E_\gamma^9$	3.27×10^{-6} $A^{2}E_\gamma^9$

where μ_N is the nuclear magneton,

$$\mu_N = \frac{e\hbar}{2M_pc}, \tag{A.3}$$

for which $\hbar c = 197.329$ MeV $\cdot$ fm, and M_p is the mass of the proton, 938.3 MeV/c^2. Thus, μ_N^2 can be written in terms of e^2fm^2 through the conversion

$$\mu_N = 0.105 \text{ efm}. \tag{A.4}$$

Weisskopf estimates for the transition probabilities $\mathcal{W}_W$ are for electric transitions

$$\mathcal{W}_W(E\lambda) = \alpha\hbar c\frac{8\pi(\lambda+1)}{\lambda[(2\lambda+1)!!]^2}\frac{1}{\hbar}\left(\frac{1}{\hbar c}\right)^{2\lambda+1}\frac{1}{4\pi}\left(\frac{3}{\lambda+3}\right)^2(1.2A^{1/3})^{2\lambda}E^{2\lambda+1}, \tag{A.5}$$

and for magnetic transitions

$$\begin{aligned}\mathcal{W}_W(M\lambda) = \alpha\hbar c\left(\frac{\hbar}{2M_pc}\right)^2\frac{8\pi(\lambda+1)}{\lambda[(2\lambda+1)!!]^2}\frac{1}{\hbar}\left(\frac{1}{\hbar c}\right)^{2\lambda+1} \\ \times\frac{10}{\pi}\left(\frac{3}{\lambda+3}\right)^2(1.2A^{1/3})^{2\lambda-2}E^{2\lambda+1}.\end{aligned} \tag{A.6}$$

The values for the first three orders of λ are listed in Table A.1. Comparison of these single-particle estimates with observed values is a good indication of the collective nature of the transition. If the observed value is much greater than the single-particle estimate, the nucleons are acting together collectively to produce the transition. On

the other hand, in the case that the observed value is in agreement with the single-particle estimate, the excitation must be largely single-particle in nature.

Appendix B

Energy Resolutions of the APEX NaI(Tl) Detectors

Energy resolutions (FWHM/centroid) are presented here for each of the individual NaI(Tl) detectors of the APEX NaI(Tl) array. The first table contains measurements taken immediately following the reconditioning at the NSCL by B.C. Perry. The second and third tables are values measured after NSCL Experiment 01017 in January of 2003. The detectors are numbered from 1 to 24.

Figure B.1: Energy resolutions measured immediately following reconditioning under laboratory conditions. The figure is the work of B.C. Perry [74].

DETECTOR NUMBER	RESOLUTION AFTER RECOUPLING	
	1173 keV	1332 keV
1	15.1% ± 0.1%	13.3% 0.1%
2	N/A ± N/A	N/A N/A
3	15.9% ± 0.1%	14.0% 0.1%
4	14.4% ± 0.1%	12.7% 0.1%
5	12.6% ± 0.1%	11.2% 0.1%
6	16.8% ± 0.2%	14.9% 0.2%
7	13.7% ± 0.0%	12.1% 0.0%
8	13.5% ± 0.1%	12.0% 0.1%
9	14.8% ± 0.1%	13.2% 0.1%
10	14.8 % ± 0.1%	13.0 % 0.1%
11	15.6 % ± 0.1%	13.8 % 0.1%
12	15.2 % ± 0.1%	13.4 % 0.1%
13	15.7 % ± 0.1%	13.9 % 0.1%
14	14.0% ± 0.1%	12.4% 0.1%
15	19.1% ± 0.3%	17.0% 0.3%
16	12.7 % ± 0.1%	11.0 % 0.1%
17	13.8 % ± 0.1%	12.2% 0.1%
18	13.7 % ± 0.1%	12.1 % 0.1%
19	13.2 % ± 0.1%	11.7 % 0.1%
20	14.0 % ± 0.1%	12.4 % 0.1%
21	14.9 % ± 0.1%	13.2 % 0.1%
22	17.8 % ± 0.2%	15.7 % 0.2%
23	15.0 % ± 0.1%	13.3 % 0.1%
24	16.6 % ± 0.2%	14.7 % 0.2%
AVERAGE	14.6% ± 0.1%	12.9% 0.1%

Table B.1: Energy resolutions for the individual APEX NaI(Tl) detectors measured January 31, 2002 in the NSCL Experiment 01017 setup.

Detector	^{137}Cs 662 keV	^{88}Y 898 keV	^{88}Y 1836 keV
01	19.8(1)%	17.8(3)%	12.0(3)%
02	23.8(2)%	19.7(4)%	13.8(4)%
03	22.8(1)%	16.3(3)%	10.9(3)%
04	20.2(1)%	16.6(3)%	11.4(3)%
05	17.3(1)%	14.1(3)%	10.2(3)%
06	19.6(1)%	15.8(3)%	11.1(3)%
07	20.1(1)%	16.7 (3)%	11.0(3)%
08	19.9(1)%	16.0 (3)%	11.1(3)%
09	19.2(1)%	18.0 (4)%	12.4(3)%
10	20.0(1)%	16.8 (3)%	12.6(3)%
11	18.5(1)%	15.8 (3)%	12.1(3)%
12	21.0(1)%	16.8 (3)%	12.0(3)%
13	20.3(1)%	18.2 (4)%	13.3(3)%
14	21.3(1)%	16.4 (3)%	11.9(3)%
15	24.3(2)%	18.6 (4)%	14.9(4)%
16	14.3(1)%	12.7 (3)%	9.1(2)%
17	18.5(1)%	15.6 (3)%	11.7(3)%
18	17.7(1)%	14.6 (3)%	10.1(3)%
19	17.4(1)%	15.3 (3)%	10.3(3)%
20	19.7(1)%	15.8 (3)%	11.9(3)%
21	16.5(1)%	14.9 (3)%	10.5(3)%
22	22.7(2)%	18.6 (4)%	13.9(4)%
23	18.9(1)%	16.4 (3)%	11.8(3)%
24	20.6(1)%	16.8 (3)%	12.6(3)%

Table B.2: Energy resolutions with uncertainties due to Doppler reconstruction at 90° and v/c=0.36 taken into account.

Detector	662 keV
01	20.8%
02	24.6%
03	23.7%
04	21.2%
05	18.4%
06	20.6%
07	21.1%
08	20.9%
09	20.2%
10	21.0%
11	19.6%
12	21.9%
13	21.3%
14	22.2%
15	25.1%
16	15.7%
17	19.6%
18	18.9%
19	18.6%
20	20.7%
21	17.7%
22	23.6%
23	19.9%
24	21.6%

Bibliography

[1] Mme. Sklodowska-Curie. *Acad. Sci. Paris: Comptes Rendus*, **126**:1101, 1898.

[2] E. Marsden and T.S. Taylor. *Proc. Roy. Soc.*, **A88**:443, 1913.

[3] E. Rutherford. *Phil. Mag.*, **21**:669, 1911.

[4] H. Geiger and E. Marsden. *Phil. Mag.*, **25**:604, 1913.

[5] H. Geiger. *Proc. Roy. Soc.*, **A83**:492, 1910.

[6] B.A. Brown. *Prog. Part. Nucl. Phys.*, **47**:517, 2001.

[7] M.G. Mayer. *Phys. Rev.*, **74**:235, 1948.

[8] DOE/NSF Nuclear Science Advisory Committee. Opportunities in nuclear science: A long-range plan for the next decade. http://dnp.nscl.msu.edu, 2002.

[9] C. Thibault *et al. Phys. Rev.*, **C12**:644, 1975.

[10] D.J. Millener, J.W. Olness, E.K. Warburton, and S.S. Hanna. *PRC*, **28**:497, 1983.

[11] I. Tanihata *et al. PRL*, **55**:2676, 1985.

[12] T. Motobayashi *et al. Phys. Lett. B*, **346**:9, 1995.

[13] F. Marti, P. Miller, D. Poe, M. Steiner, J. Stetson, and X.Y. Wu. Commissioning of the coupled cyclotron system at the nscl. In *Proc. 16th International Conference on Cyclotrons and Their Applications*, East Lansing, Michigan, 2001.

[14] T. Glasmacher. *Annu. Rev. Nucl. Part. Sci.*, **48**:1, 1998.

[15] A. Bohr and B.R. Mottleson. *Nuclear Structure: Volume 1 Single-Particle Motion*. W.A. Benjamin, Inc., 1969.

[16] A. deShalit and H. Feshbach. *Theoretical Nuclear Physics Vol. 1: Nuclear Structure*. John Wiley and Sons, 1974.

[17] S. Raman. *At. Data and Nucl. Data Tables*, **78**:1, 2001.

[18] A. Bohr and B.R. Mottleson. *Nuclear Structure: Volume 2 Nuclear Deformations*. W.A. Benjamin, Inc., 1975.

[19] R.F. Casten. *Nuclear Structure from a Simple Perspective.* Oxford University Press, 2000.

[20] M.G. Mayer. *Phys. Rev.*, **75**:1969, 1949.

[21] O. Haxel, J.H.D. Jensen, and H.E. Suess. *Phys. Rev.*, **75**:1766, 1949.

[22] T. Otsuka, Y. Utsuno, M. Honma, and T. Mizusaki. *Prog. Part. Nucl. Phys.*, **46**:155, 2001.

[23] G.A. Lalazissis, A.R. Farhan, and M.M. Sharma. *Nucl. Phys. A*, **628**:221, 1998.

[24] S.G. Nilsson *et al. Shapes and Shells in Nuclear Structure.* Cambridge University Press, 1995.

[25] B.V. Pritychenko *et al. Phys. Lett. B*, **461**:322, 1999.

[26] D. Guillemaud-Mueller *et al. Nucl. Phys. A*, **426**:37, 1984.

[27] B.V. Pritychenko *et al. Phys. Rev. C*, **63**:011305, 2000.

[28] B.V. Pritychenko *et al. Phys. Rev. C*, **63**:047308, 2001.

[29] R.W. Ibbotson *et al. Phys. Rev. Lett.*, **80**:2081, 1998.

[30] E. Warburton, J. Becker, and B. Brown. *Phys. Rev. C*, **41**:1147, 1990.

[31] X. Campi, H. Flocard, A.K. Kerman, and S. Koonin. *Nucl. Phys. A*, **251**:193, 1975.

[32] B.H. Wildenthal and W. Chung. *Phys. Rev. C*, **22**:2260, 1980.

[33] A. Watt, R.P. Singhal, M.H. Storm, and R.R. Whitehead. *J. Phys. G*, **L145**:7, 1981.

[34] A. Poves and J. Retamosa. *Phys. Lett. B*, **184**:311, 1987.

[35] B.V. Pritychenko *et al. Phys. Rev. C*, **66**:024325, 2002.

[36] M. Keim *et al. Eur. Phys. J. A*, **8**:31, 2000.

[37] Y. Yanagisawa *et al. Phys. Lett. B*, **566**:84, 2003.

[38] K. Yoneda *et al. Phys. Lett. B*, **499**:233, 2001.

[39] H. Iwasaki *et al. Phys. Lett. B*, **522**:227, 2001.

[40] C. Détraz *et al. Phys. Rev. C*, **19**:164, 1979.

[41] V. Chiste *et al. Phys. Lett. B*, **514**:233, 2001.

[42] G. Klotz *et al. Phys. Rev. C*, **47**:2502, 1993.

[43] M. Belleguic *et al. Nucl. Phys. A*, **682**:136c, 2001.

[44] N. Fukunishi *et. al. Phys. Lett. B*, **296**:279, 1992.

[45] J. Raynal. Coupled channels code ecis79, unpublished.

[46] R. Liguori Neto *et al. Nucl. Phys. A*, **560**:733, 1993.

[47] J. Barrette *et al. Phys. Lett. B*, **209**:182, 1988.

[48] N. Alamanos *et al. Phys. Lett. B*, **137**:37, 1984.

[49] C.A. Bertulani *et al. Computer Phys. Comm.*, **116**:1459, 1999.

[50] P.M. Endt. *At. Data and Nucl. Data Tables*, **55**:171, 1993.

[51] J. Raynal. Coupled channels code ecis94, unpublished.

[52] R.A. Broglia. *Heavy Ion Reactions, Vol. 1.* Benjamin/Cummings, 1981.

[53] W. Mittig *et al. Eur. Phys. J. A*, **15**:157, 2002.

[54] F. Azaiez. *Nucl. Phys. A*, **704**:37c, 2002.

[55] D. Guillemaud-Mueller. *Eur. Phys. J. A*, **13**:63, 2002.

[56] Y. Utsuno, T. Otsuka, T. Mizusaki, and M. Honma. *Phys. Rev. C*, **60**:054315, 1999.

[57] E. Caurier, F. Nowacki, and A. Poves. *Nucl. Phys. A*, **693**:2001, 2001.

[58] P.-G Reinhard *et al. Phys. Rev. C*, **60**:014316, 1999.

[59] P.D. Stevenson, J. Rikovska Stone, and M.R. Strayer. *Phys. Lett. B*, **545**:291, 2002.

[60] M.V. Stoitsov *et al. Phys. Rev. C*, **61**:034311, 2000.

[61] F. Grümmer *et al. Phys. Lett. B*, **387**:673, 1996.

[62] S.K. Patra and C.R. Praharaj. *Phys. Lett. B*, **273**:13, 1991.

[63] Z. Ren *et al. Phys. Lett. B*, **380**:241, 1996.

[64] R. Rodríguez-Guzmán, J.L Egido, and L.M. Robledo. *Nucl. Phys. A*, **709**:201, 2002.

[65] H. Scheit, T. Glasmacher, R.W. Ibbotson, and P.G. Thirolf. *Nucl. Instr. and Meth. A*, :124, 1999.

[66] A. Winther and K. Alder. *Nucl. Phys. A*, **319**:518, 1979.

[67] F.D. Becchetti *et al. Phys. Rev. C*, **40**:R1104, 1989.

[68] R. Anne *et al. Z. Phys. A*, **352**:397, 1995.

[69] M. Fauerbach. *Study of Light Neutron-rich Nuclei.* PhD thesis, Michigan State University, 1997.

[70] H. Scheit. *Low-Lying Collective Excitations in Neutron-Rich Even-Even Sulfur and Argon Isotopes Studied via Intermediate-Energy Coulomb Excitation and Proton Scattering.* PhD thesis, Michigan State University, 1998.

[71] K. Miller. *Nuclear Structure near N=Z=28: Study of Neutron-Deficient Nickel Isotopes via One-Neutron Knockout and Intermediate-Energy Coulomb Excitation.* PhD thesis, Michigan State University, 2003.

[72] K. Alder, A. Bohr, T. Huss, B. Mottleson, and A. Winther. *Rev. Mod. Phys.*, **28**:432, 1954.

[73] N.I. Kaloskamis *et. al. Nucl. Instr. and Meth. A*, **330**:447, 1995.

[74] B.C. Perry, C.M Campbell, J.A. Church, D.-C. Dinca, J. Enders, T. Glasmacher, Z. Hu, K.L. Miller, W.F. Mueller, and H. Olliver. *Nucl. Instr. and Meth. A*, **505**:85, 2003.

[75] H. Koivisto, D. Cole, A. Fredell, C. Lyneis, P. Miller, J. Moskalik, B.Nurnberger, J. Ottarson, A. Zeller, J. DeCamp, R. Vondrasek, P.A. Zavodszky, , and D. Xie. Artemis - the new ecr ion source for the coupled cyclotron facility at nscl/msu. In S. Gammino and G. Ciavola, editors, *Proceedings of the Workshop on the Production of Intense Beams of Highly Charged Ions*, volume **72**, page 135, Catania, Italy, 2000. Italian Physical Society.

[76] D. J. Morrissey, B. M. Sherrill, M. Steiner, A. Stolz, and I. Wiedenhoever. *Nucl. Instr. and Meth. B*, **204**:90, 2003.

[77] C. Zhou. *Nucl. Data Sheets*, **76**:399, 1995.

[78] M.J. Martin. *Nucl. Data Sheets*, **63**:723, 1991.

[79] W.F. Mueller, J.A. Church, T. Glasmacher, D. Gutknecht, G. Hackman, P.G. Hansen, Z. Hu, K.L. Miller, and P. Quirin. *Nucl. Instr. and Meth. A*, **466**:492, 2001.

[80] A. Gade. private communication, 2003.

[81] G.F. Knoll. *Radiation Detection and Measurement.* John Wiley and Sons, Inc., New York, 2000.

[82] B.V. Pritychenko. *Intermediate-Energy Coulomb Excitation of the Neutron-Rich Radioactive Isotopes* $^{26,28}Ne$, $^{28-31}Na$, $^{30-34}Mg$, $^{34,35}Al$, ^{33}Si *and* ^{34}P. PhD thesis, Michigan State University, 2000.

[83] D. Bazin, O. Tarasov, M. Lewitowicz, and O. Sorlin. *Nucl. Instr. and Meth. A*, **482**:314, 2002.

[84] J. Ziegler. The stopping and range of ions in matter, http://www.srim.org.

[85] C.J. Benesh *et al. Phys. Rev. C*, **40**:1198, 1989.

[86] R. Fox, C. Bolen, K. Orji, and J. Venema. The spectcl analysis program. In *Proceedings of the 2003 IEEE Conference on Real Time Applications in Nuclear, Particle and Plasma Physics*, Montreal, 2003.

[87] Chalk River Nuclear Laboratories. *GF2: Notes on the use of the program GF2*, 1989.

[88] J.K. Ousterhout. *Tcl and the Tk Toolkit*. Addison-Wesley, 1994.

[89] B.B. Welch. *Practical Programming in Tcl and Tk*. Prentice Hall, 3rd edition edition, 2000.

[90] TRIUMF. *Physica: Reference Manual*, 1994.

[91] Application Software Group, Computing Networks Division, CERN, Geneva, Switzerland. *GEANT: Detector Description and Simulation Tool*, 1993.

[92] E. Storm and H.I. Israel. *At. Data and Nucl. Data Tables*, **A7**:565, 1970.

[93] S. Wolfram. *The Mathematica Book*. Cambridge University Press, 1996.

[94] P.R. Bevington and D. Keith Robinson. *Data Reduction and Error Analysis for the Physical Sciences*. McGraw-Hill, 3rd edition edition, 2003.

[95] H. Olliver. private communication, 2003.

[96] A.H. Wapstra, G.J. Nijgh, and R. Van Lieshout. *Nuclear Spectroscopy Tables*. North Holland Publishing Company, Amsterdam, 1959.

[97] W.R. Leo. *Techniques for Nuclear and Particle Physics Experiments*. Springer-Verlag, Berlin Heidelberg, 2nd edition edition, 1994.

[98] P.H. Stelson and F.K. McGowan. *Phys. Rev.*, **110**:489, 1957.

[99] K.I. Erokhina and I.K. Lemberg. *Izv. Akad. Nauk. SSSR, Ser. Fiz.*, **26**:205, 1962.

[100] J. Barrette *et al. Nucl. Phys. A*, **172**:41, 1971.

[101] S.J. Burger and G. Heynman. *Nucl. Phys. A*, **243**:461, 1975.

[102] H. Iwasaki *et al. Phys. Lett. B*, **491**:8, 2000.

[103] L. Riley. private communication, 2003.

[104] P.M. Endt. *Nucl. Phys. A*, **633**:1, 1988.

[105] B.A. Brown. private communication, 2003.

[106] P.M. Endt. *At. Data and Nucl. Data Tables*, **23**:3, 1979.

[107] E.Caurier, F. Nowacki, A. Poves, and J. Retamosa. *Phys. Rev. C*, **58**:2033, 1998.

[108] R.W. Ibbotson *et al. Phys. Rev. C*, **59**:642, 1999.

[109] S.S.M. Wong. *Introductory Nuclear Physics*. John Wiley and Sons, 2nd edition edition, 1998.